

SOURCE REGION CHARACTERISTICS OF
MAGNETOSPHERIC ELF/VLF BANDED CHORUS EMISSIONS

A DISSERTATION
SUBMITTED TO THE DEPARTMENT OF
ELECTRICAL ENGINEERING
AND THE COMMITTEE ON GRADUATE STUDIES
OF STANFORD UNIVERSITY
IN PARTIAL FULFILLMENT OF THE REQUIREMENTS
FOR THE DEGREE OF
DOCTOR OF PHILOSOPHY

Naoshin Haque
May 2012

© 2012 by Naoshin Haque. All Rights Reserved.

Re-distributed by Stanford University under license with the author.



This work is licensed under a Creative Commons Attribution-Noncommercial 3.0 United States License.

<http://creativecommons.org/licenses/by-nc/3.0/us/>

This dissertation is online at: <http://purl.stanford.edu/hq112qw1569>

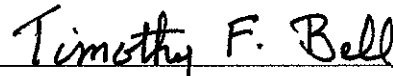
Naoshin Haque

I certify that I have read this dissertation and that, in my opinion, it is fully adequate in scope and quality as a dissertation for the degree of Doctor of Philosophy.



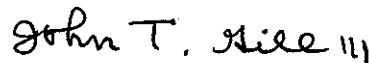
(Umran S. Inan) Principal Advisor

I certify that I have read this dissertation and that, in my opinion, it is fully adequate in scope and quality as a dissertation for the degree of Doctor of Philosophy.



(Timothy F. Bell)

I certify that I have read this dissertation and that, in my opinion, it is fully adequate in scope and quality as a dissertation for the degree of Doctor of Philosophy.



(John T. Gill III)

Approved for the University Committee on Graduate Studies

Abstract

Geomagnetically trapped electrons in the Earth's radiation belts have energies ranging from a few keV to several MeV. Electrons with relativistic energies may cause serious damage to spacecraft systems through their interactions with onboard electronics. Natural electromagnetic plasma waves, known as extremely low frequency/very low frequency (ELF/VLF) chorus, are able to accelerate electrons with energies in the keV range to energies in the MeV range, increasing the flux of relativistic electrons. Chorus, observed in the magnetosphere outside the plasmapause, often appears in two distinct frequency bands separated by an emission gap, which occurs where the wave power exhibits a minimum. This configuration, known as banded chorus, consists of an upper band (UB) of chorus located above the emission gap and a lower band (LB) of chorus located below this gap. This dissertation explores the source region characteristics of magnetospheric banded chorus emissions using data from the Cluster spacecraft and the Polar spacecraft to provide a better understanding of the properties of these waves.

A new theory has emerged suggesting banded chorus is generated within whistler-mode ducts. In particular, the theory states UB chorus can be guided in depletion ducts and LB chorus can be guided in either depletion or enhancement ducts depending on the wave normal angle. To test this theory, electron densities are determined with the highest spatial resolution to date. Irregularities in the electron density profiles are classified as ducts if they satisfy the two ducting requirements involving the half-width and the enhancement or depletion factor.

The relationship between banded chorus and ducts is analyzed using data from the Cluster spacecraft. For this data set, LB chorus emissions are found to be generated within ducts located at the same L -shell within $\sim 3^\circ$ of the magnetic equator. The wave normal

angle distribution for the LB chorus generated within whistler-mode enhancement and depletion ducts show that the majority of the LB chorus waves can be guided by these ducts as well. LB chorus emissions can also be uniformly excited over an extended region near the magnetic equator.

The wave normal angle analysis is extended to both LB and UB chorus emissions in the equatorial and off-equatorial regions using data from the Polar spacecraft. LB chorus tends to be quasi-field-aligned with increasing probability as the magnetic latitude increases, while UB chorus tends to have oblique wave normal angles. In addition, the LB chorus waves have a time averaged Poynting flux that is much greater than that of UB chorus waves. The wave normal angle distribution is important for the evaluation of resonant wave-particle interactions.

Analysis of the spatial dependence of chorus intensity resulted in observations of two main configurations of banded chorus. The first configuration has chorus absent within 1° of the magnetic equator, while the second has only weak chorus emissions in this region. For both configurations, the intensity of banded chorus generally has an exponential spatial dependence on distance away from the magnetic equator. The distribution of the spatial growth factor provides a new boundary condition for chorus generation models.

This dissertation provides many new contributions and advances our fundamental understanding of the source region characteristics of magnetospheric ELF/VLF banded chorus emissions.

Acknowledgments

As my time at Stanford comes to an end, I would like to thank everyone who has supported me and helped me reach the end of this long and winding road to a Ph.D.

I would like to thank my principal advisor, Professor Umran Inan, for bringing me into the VLF group and for all of his support, enthusiasm, and leadership over the past five years. His unlimited energy and passion for VLF research are truly inspiring. Thanks to Umran, I had the opportunity to work on many interesting projects, as well as travel to some of the most beautiful countries all over the world.

I would also like to express my gratitude to my second advisor, Dr. Timothy Bell, for his guidance, helpfulness, and patience. Tim is one of the most knowledgeable scientists I have had the pleasure of working with. I greatly enjoyed our discussions on chorus, ducts, and life in general.

During my first few years at Stanford, I had the opportunity to work closely with Dr. Maria Spasojević. Maria was an incredible mentor and taught me the fundamentals of being a meticulous researcher.

I would also like to thank Professor John Gill III for serving on my oral defense committee and for his reading of this dissertation, as well as Professor Sigrid Close for serving as the chair of my defense committee.

I am grateful to Professor Don Carpenter for his depth of knowledge and historical insight into ducts and for his consistent interest in my work.

I owe immense thanks to Ms. Jolene Pickett, the Principal Investigator of the Cluster WBD instrument, and to Dr. Ondrej Santolík. Jolene has always been quick to answer my questions and provide access to Cluster WBD data. Ondrej was instrumental in providing access to Cluster STAFF data.

I would like to thank the Cluster WHISPER team for giving me the opportunity to use their database and determine electron densities at the Centre National de la Recherche Scientifique in Orléans, France for three weeks. Dr. Jean-Gabriel Trotignon, the Principal Investigator, made this trip possible and was very welcoming. I would like to particularly thank Dr. Guillaume Lointier for teaching me how to identify the different resonances and for validating all of my results. I also enjoyed working with the rest of the WHISPER team, Drs. Xavier Vallières, Gabor Facskó, Sena Koungblenou, Jean-Louis Rauch, and Pierette Decreau.

Shaolan Min and Helen Niu ensure that the VLF group always runs smoothly. From scheduling to reimbursements, they take care of everything. Dan Musetescu has also been a great help in providing me access to the Cluster DVDs and replacing my hard drive when it crashed right before my thesis defense.

I would like to thank the IHY/ISWI AWESOME team Kevin Graf, Vijay Harid, Nick LaVassar, and especially Morris Cohen, Ben Cotts, and Debbie Scherrer for all the fantastic experiences we shared planning our workshops and traveling the world. I am very grateful to have had the chance to work on this international scientific outreach program, which gives scientists in developing countries some of the same opportunities we have available at Stanford.

I would like to extend my sincere thanks to all past and present members of the VLF group. I have benefited greatly from the discussions, knowledge, and friendship of many VLF members. I would especially like to acknowledge Amanda Daniel, Forrest Foust, Dan Golden, George Jin, Justin Li, Bob Marshall, Denys Pidnyachiy, and Fadi Zoghzoghy. I would also like to thank all of my friends and family for always being there for me throughout this process.

Above all, I wish to thank my parents, Mohammad and Monoara Haque, and my sister, Farhana Haque, for a lifetime of love, support, and encouragement and for all that they have done for me.

NAOSHIN HAQUE
Stanford, California
March 23, 2012

This research was supported by the National Aeronautics and Space Administration through grants NNX07AI24G and NNX09AF51G and the Office of Naval Research through grant N000140710789.

Contents

Abstract	iv
Acknowledgments	vi
1 Introduction	1
1.1 The Earth's Magnetosphere	1
1.2 ELF/VLF Banded Chorus Emissions	4
1.2.1 Banded Structure of Chorus	5
1.2.2 Cyclotron Resonance	7
1.3 Satellite Systems	7
1.3.1 The Cluster Mission	8
1.3.2 The Polar Mission	10
1.4 Overview and Contributions	11
2 Ducting Theory for Banded Chorus	13
2.1 Whistler-Mode Ducts	13
2.2 Commonalities of Three Types of Emissions	15
2.3 Refractive Index	17
2.4 Guidance by Whistler-Mode Ducts	21
2.5 Ducting of Chorus Waves	25
2.6 Summary	27
3 Determination of Electron Density	29
3.1 Cluster Instruments	29

3.1.1	EFW	30
3.1.2	WHISPER	30
3.2	Resonances in the Magnetosphere	31
3.3	Calculation of Electron Density	33
3.4	Ducting Requirements	36
3.5	Summary	37
4	Banded Chorus and Ducts	38
4.1	Case I: October 31, 2003	39
4.2	Case II: January 20, 2004	41
4.2.1	Lower Band Chorus Excitation	46
4.3	Lower Band Chorus Statistics	47
4.4	Summary	53
5	Wave Normal Angle Distribution	55
5.1	Chorus Wave Normal Angles	56
5.2	Classification of Wave Normal Angles	59
5.3	Upper Band Chorus Wave Normal Angles	61
5.4	Lower Band Chorus Wave Normal Angles	66
5.5	Comparison With Previous Work	71
5.6	Summary	73
6	Spatial Dependence of Chorus Intensity	75
6.1	Chorus Intensity	76
6.2	Case I: October 31, 2003	77
6.3	Case II: September 19, 2003	79
6.4	Spatial Dependence Statistics	81
6.5	Summary	83
7	Summary and Future Research	85
7.1	Summary of Major Results	85
7.2	Suggestions for Future Research	87

List of Figures

1.1	The Magnetosphere	2
1.2	Dipole Coordinate System	3
1.3	Electron Density Distribution in Inner Magnetosphere	4
1.4	Example of Banded Chorus	6
1.5	Cyclotron Resonance	8
1.6	Cluster Spacecraft	9
1.7	Polar Spacecraft	10
2.1	Magnetospheric Reflections and Ducts	14
2.2	Whistler-Mode Ducts	15
2.3	Triggered Emissions	16
2.4	Refractive Index Surfaces	20
2.5	Gendrin Angle	21
2.6	Guidance by Depletion Ducts	22
2.7	Guidance by Enhancement Ducts	24
2.8	Ducting of Banded Chorus	26
2.9	Emission Gap	26
3.1	EFW Instrument	31
3.2	WHISPER Instrument	32
3.3	Bernstein Modes	33
3.4	Magnetospheric Resonances	34
3.5	Plasma Frequency Measurements	35
3.6	Electron Density Profile	36

4.1	Observations on October 31, 2003	40
4.2	Observations on January 20, 2004	42
4.3	Backward Ray Tracing for Set 1	44
4.4	Wave Normal Angles for Set 2	45
4.5	Refractive Index Surface for Set 2	46
4.6	Lower Band Chorus Propagation	48
4.7	Cluster Passes	49
4.8	Wave Normal Distribution for Depletion Ducts	51
4.9	Wave Normal Distribution for Enhancement Ducts	52
4.10	Correlation Between Ducts and Intensity	53
5.1	Observations on December 14, 1996	58
5.2	UB Chorus Cases	62
5.3	Polar Passes for UB Chorus	63
5.4	Histogram of θ for UB Chorus	64
5.5	Histogram of θ for Different Ranges of λ for UB Chorus	64
5.6	$\theta_R - \theta$ vs. λ	65
5.7	Poynting Flux for UB Chorus	66
5.8	LB Chorus Cases	67
5.9	Polar Passes for LB Chorus	68
5.10	Histogram of θ for LB Chorus	69
5.11	Histogram of θ for Different Ranges of λ for LB Chorus	70
5.12	$ \theta_G - \theta $ vs. λ	70
5.13	Poynting Flux for LB Chorus	71
6.1	Observations on October 31, 2003	78
6.2	Observations on September 19, 2003	80
6.3	Histogram of α	82
6.4	Chorus Elements on October 31, 2003	82
7.1	Observations on January 6, 2004	88

Chapter 1

Introduction

The Earth’s radiation belts, comprised of highly energetic charged particles, are toroidal regions extending from radial distances of approximately 1.2 to 8 Earth radii (R_E). These geomagnetically trapped ions and electrons have energies ranging from a few keV to several MeV. Such relativistic electrons may cause serious damage to spacecraft systems through their interactions with onboard electronics [[Baker, 2000](#)]. Natural electromagnetic plasma waves, known as chorus, are able to accelerate electrons with energies in the keV range to energies in the MeV range, increasing the flux of relativistic electrons [[Horne, 2002](#)]. For this reason, it is important to learn more about the properties of these waves. The goal of this dissertation is to provide a better understanding of the source region characteristics of chorus emissions.

1.1 The Earth’s Magnetosphere

Chorus emissions have been observed in the magnetospheres of Earth, Jupiter, and Saturn [[Inan et al., 1983](#); [Inan, 1986](#)], making the source region characteristics of chorus of wide general interest. This dissertation will focus solely on chorus emissions observed in the Earth’s magnetosphere, the region in space where plasma dynamics are dominated by the Earth’s magnetic field. The solar wind, blown outward from the Sun, interacts with the Earth’s intrinsic magnetic field, causing the magnetosphere to take a bullet-like shape, as shown in the schematic diagram in Figure [1.1](#). The boundary of the magnetosphere, known

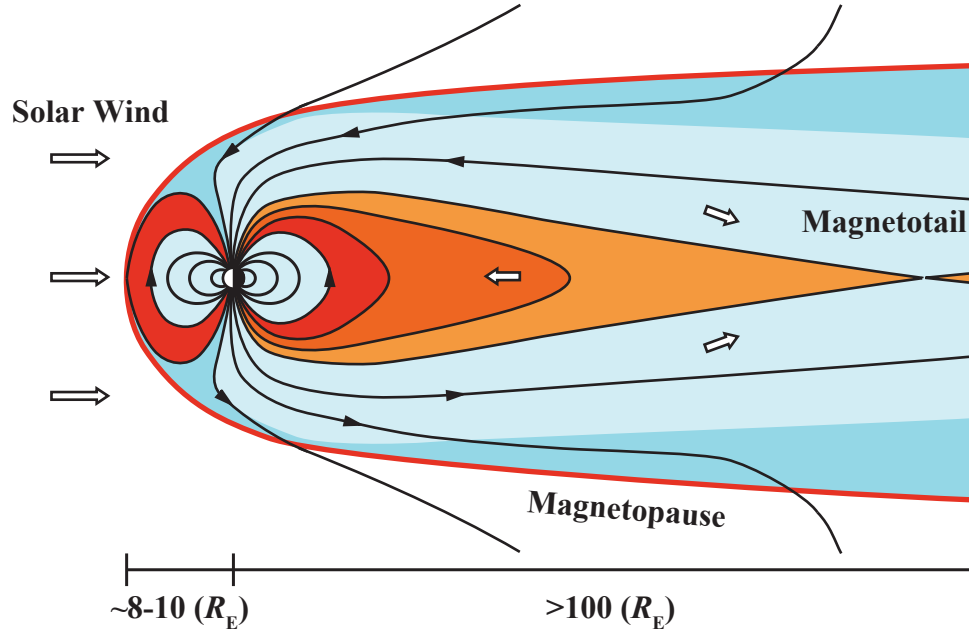


Figure 1.1: A schematic diagram of the magnetosphere showing the interaction of the solar wind with the Earth's magnetic field. Closer to the Earth, the magnetic field can be accurately modeled as a dipole, as the distortion from the solar wind is minimal.

as the magnetopause, is located at a radial distance of $\sim 8 - 10R_E$ on the dayside. On the nightside, a long magnetotail is formed, extending out to more than $100R_E$.

The inner magnetosphere, extending to $\sim 6R_E$, is where the magnetic field lines are closed and is the most important region of the magnetosphere in the context of this dissertation. To first order, the Earth's magnetic field in this region may be approximated by a centered, tilted dipole, where the dipole axis is inclined by approximately 11° with respect to the geographic rotation axis. Under this approximation, a location in space can be described using three parameters of the dipole coordinate system: L -shell value (L), magnetic latitude (λ), and magnetic local time (MLT), as shown in Figure 1.2. The L -shell value is defined as the distance, in units of Earth radii, at which a magnetic field line crosses the magnetic equatorial plane. For instance, if a field line intersects the magnetic equator at a radial distance (R) of $4R_E$, this field line has an L -shell value of 4. The parameter λ is the angle measured from the magnetic equator to the point of interest on the field line. The

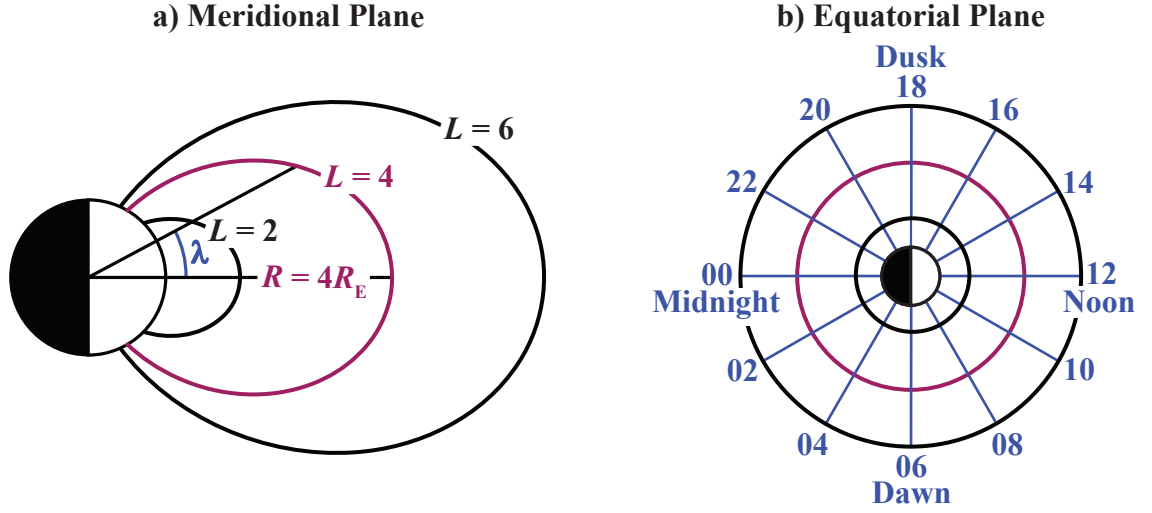


Figure 1.2: The dipole coordinate system of the magnetic field illustrated in the a) meridional and b) equatorial planes identifying the three parameters: L -shell value (L), magnetic latitude (λ), and magnetic local time (MLT).

formula that describes the locus of a field line is given by

$$R = L \cos^2 \lambda \quad (1.1)$$

for a dipole magnetic field [Walt, 1994, Ch. 3]. Finally, MLT describes the location of the field line with respect to the direction of the sun in decimal hours. The MLT values of 00, 06, 12, and 18 describe magnetic midnight, dawn, noon, and dusk, respectively.

The magnetosphere, a magnetized, inhomogeneous, collisionless plasma, exhibits a wide range of electron densities (N_e). A model of the electron density distribution of the cold electron population (energies ~ 1 eV) in the inner magnetosphere is shown in Figure 1.3. The ionosphere is the top layer of the Earth's atmosphere with $N_e > 10^4 \text{ cm}^{-3}$. The plasmasphere, a primarily field-aligned toroidal region of cold plasma, is essentially an extension of the ionosphere with a cold electron density ranging from about 10 to 10^4 cm^{-3} . The boundary of the plasmasphere, known as the plasmapause, occurs where there is a steep decrease in electron density, usually by an order of magnitude over a distance as small as $0.1 R_E$ [Carpenter and Anderson, 1992]. The source region of chorus emissions is outside the plasmapause near the magnetic equatorial plane [LeDocq et al., 1998; Parrot

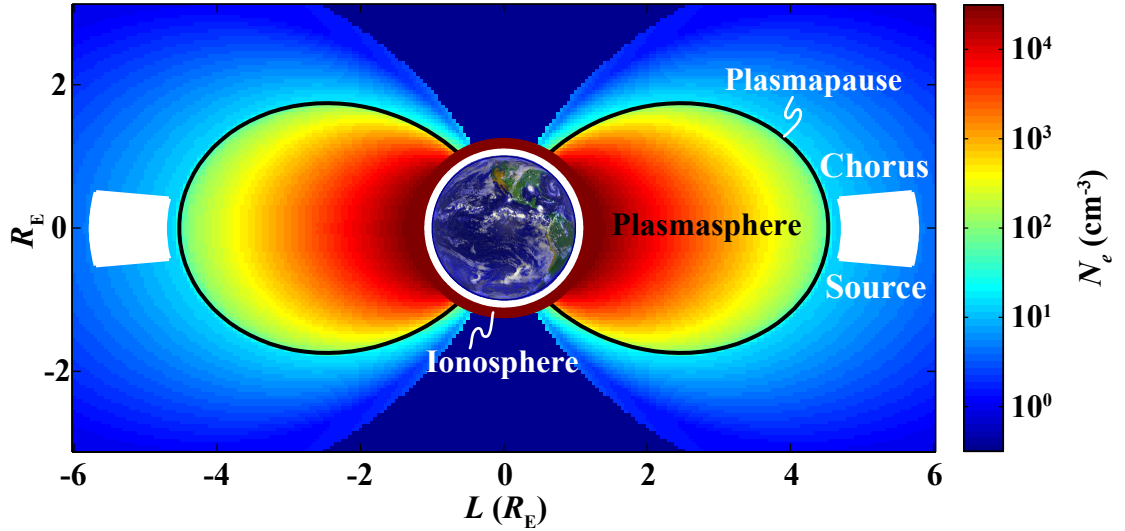


Figure 1.3: A model electron density distribution for different plasma regions in the inner magnetosphere. The value of the electron density is shown on the log color scale. Figure adapted from [Spasojević \[2003, Fig. 1.4\]](#).

[et al., 2003](#); [Santolík et al., 2005](#)].

1.2 ELF/VLF Banded Chorus Emissions

Chorus emissions are intense electromagnetic plasma waves that are naturally and spontaneously excited in the inner magnetosphere during periods of magnetic disturbance. These emissions are observed over a broad frequency range, from hundreds of Hz up to about 10 kHz [[Gurnett and O’Brien, 1964](#)], a subset of the Extremely Low Frequency/Very Low Frequency (ELF/VLF) band occurring between 0.3 and 30 kHz. The ELF/VLF band overlaps the audible frequency range of 0.02 to 20 kHz. Early observations of chorus emissions involved listening to the plasma waves by connecting the ELF/VLF analog signal to an audio amplifier and speaker [[Allcock, 1957](#)]. The plasma waves could then be identified using the human brain’s natural ability to compute Fourier transforms of the audio output. Chorus emissions are named for their resemblance in sound to birds’ dawn chorus, which is similar to a “rookery heard from a distance” [[Storey, 1953](#)].

An example of chorus is shown in the frequency-time spectrogram of Figure 1.4, which

displays 8 seconds of plasma wave data observed on the Cluster spacecraft (described in Section 1.3.1) on April 18, 2002. The spectrogram shows the power spectral density of the wave electric field as a function of frequency and time. Chorus waves are composed of closely spaced discrete elements, each of which may last up to several seconds and exhibit an approximately linear rate of frequency change of up to a few kHz/sec [Sazhin and Hayakawa, 1992; Santolík, 2008, and references therein]. While chorus is usually observed consisting of rising tones, falling tones, short impulsive bursts, and sometimes so-called ‘hooks’ may also be observed [Burtis and Helliwell, 1969]. Chorus waves propagate in the whistler-mode, with right-handed elliptical polarization, with respect to time, which reduces to circular polarization for propagation parallel to the ambient magnetic field. Whistler-mode waves have frequencies in the range $0 < f < f_{ce}$ for $f_{ce} < f_{pe}$ and in the range $0 < f < f_{pe}$ for $f_{pe} < f_{ce}$, where f_{ce} is the frequency with which an electron gyrates about the ambient magnetic field (B_0) and can be expressed as

$$f_{ce} = \frac{qB_0}{2\pi m}, \quad (1.2)$$

with q and m being the charge and mass of the electron, respectively, and f_{pe} is a natural frequency of oscillation, known as the plasma frequency, that is expressed as

$$f_{pe} = \frac{q}{2\pi} \sqrt{\frac{N_e}{m\epsilon_0}}, \quad (1.3)$$

where ϵ_0 is the permittivity of free space. For the typical case in the magnetosphere, $f_{pe} \gg f_{ce}$, and the whistler-mode waves propagate with frequencies exclusively below f_{ce} .

1.2.1 Banded Structure of Chorus

Chorus often appears in two distinct frequency bands separated by an emission gap, which occurs near $f_{ce}/2$, where the wave power exhibits a minimum [Burtis and Helliwell, 1969, 1975, 1976; Tsurutani and Smith, 1974]. This configuration, known as banded chorus, consists of an upper band (UB) of chorus located above the emission gap and a lower band (LB) of chorus located below this gap. Banded chorus has the same spatial distribution as all chorus, but with a reduced frequency of occurrence. Banded chorus is observed at all

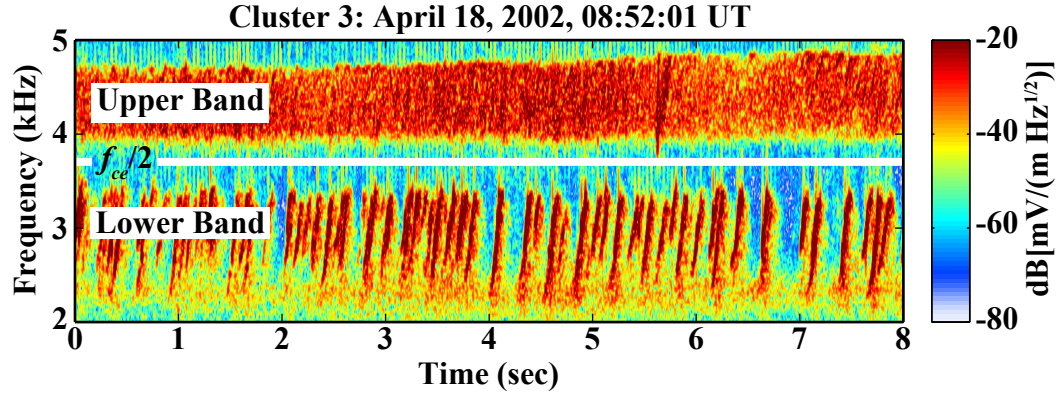


Figure 1.4: Frequency-time spectrogram of banded chorus observed by the Cluster spacecraft. The white line represents $f_{ce}/2$ and the color scale represents the intensity of the electric field in dB with respect to $1 \text{ mV}/\text{m}\sqrt{\text{Hz}}$.

local times for $L = 4 - 9$, although it is most common in the midnight-noon local time sector [Koons and Roeder, 1990].

The width of the emission gap, δf , between the two chorus bands is variable and generally lies in the range $0 \leq \delta f \leq f_{ce}/5$. There is currently no commonly accepted explanation as to why the banded structure of chorus is observed or why the emission gap occurs near $f_{ce}/2$. One theory for the two-banded structure of chorus is a two-source model, which suggests that UB chorus is locally generated, while LB chorus is generated further out in the magnetosphere in regions of lower magnetic field [Maeda, 1976]. The LB chorus waves then propagate away from their region of generation near the magnetic equator and get reflected, subsequently propagating back to the equatorial plane at a location closer to the Earth. This theory has not been developed in detail and its feasibility depends on the efficiency of the reflection process. Another theory is that the emission gap between the two chorus bands is due to Landau damping of the chorus waves by electrons that are traveling in phase with the waves and have a decreasing distribution function with increasing energy [Tsurutani and Smith, 1974]. However, Landau damping only produces this emission gap after the chorus waves have propagated a significant distance (10° - 20°) away from the magnetic equator [Bortnik et al., 2006], though banded chorus has often been observed very close to the equator. A new theory suggesting that the banded structure of chorus arises from the properties of the chorus source region is described in Chapter 2.

1.2.2 Cyclotron Resonance

Chorus emissions are generated spontaneously through a cyclotron resonance interaction in which a triggering plasma wave from the noise background, propagating in the whistler-mode, is amplified by counterstreaming energetic electrons gyrating in the same sense, as shown in Figure 1.5a. This interaction occurs when the Doppler-shifted frequency of the wave is equal to the electron gyrofrequency, expressed as

$$\omega - k_{\parallel} v_{\parallel} = \frac{\omega_{ce}}{\gamma}. \quad (1.4)$$

In this expression, ω is the frequency of the wave, k_{\parallel} and v_{\parallel} are the components of the wave vector and particle velocity parallel to the ambient magnetic field, respectively, ω_{ce} is the local gyrofrequency, and $\gamma = (1 - v^2/c^2)^{-\frac{1}{2}}$ is the relativistic mass factor, where v is the particle velocity and c is the speed of light [Kennel and Petschek, 1966].

The wave vector is typically specified with respect to \mathbf{B}_0 , with the polar and azimuthal wave normal angles, θ and ϕ , defined as the angles between \mathbf{B}_0 and the wave vector. This coordinate system is illustrated in Figure 1.5b, with the direction of \mathbf{B}_0 assumed to be in the z direction. Of the two wave normal angles, only the polar wave normal angle is needed to evaluate the resonance condition. Though it is widely believed that chorus is generated through cyclotron resonance, many characteristics of the chorus source region are still unknown. This dissertation examines such characteristics through the use of electron densities, polar wave normal angle distributions, and chorus intensity, as discussed in Chapters 3 through 6.

1.3 Satellite Systems

This dissertation is based primarily on observations from both the Cluster spacecraft [Escoubet et al., 1997] and the Polar spacecraft [Harten and Clark, 1995].

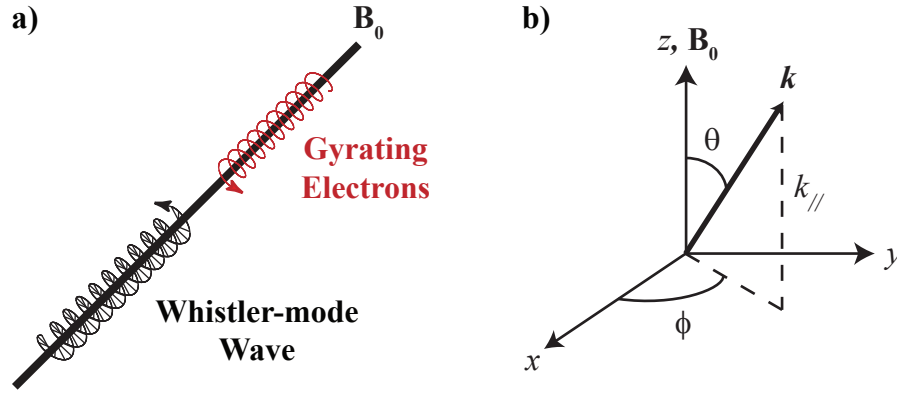


Figure 1.5: a) Schematic representation of cyclotron resonance, in which a triggering whistler-mode plasma wave is amplified by counterstreaming electrons gyrating in the same sense. b) Coordinate system depicting polar wave normal angle, θ , azimuthal wave normal angle, ϕ , and wave vector, \mathbf{k} . The direction of the local magnetic field, \mathbf{B}_0 , is assumed to be in the z direction in this system.

1.3.1 The Cluster Mission

The Cluster mission consists of four identical spacecraft flying in a tetrahedral formation around the Earth, shown in Figure 1.6a, with the spacecraft separation varying between 200 and 2000 km. The satellites were launched in two pairs on July 16 and August 9, 2000 and moved into the operational phase in February 2001. The Cluster mission, which is planned and managed by the European Space Agency (ESA), has been approved to operate until the end of 2014. The highly elliptical orbit, designed for exploration of different regions of the magnetosphere, has a perigee of $3.4R_E$, an apogee of $18.3R_E$, an inclination of 88.5° , and a period of 57 hours. The orbit has been systematically changed over time, with the orbits for the years 2001 and 2009 shown in Figure 1.6b. Chorus emissions are usually observed near perigee close to the magnetic equatorial plane.

Each Cluster spacecraft, with a mass of 1200 kg, has two electric and two magnetic antennas connected to 11 instruments: 5 wave instruments and 6 particle instruments. There are six instruments of interest for this dissertation. The fluxgate magnetometer (FGM) [Balogh *et al.*, 1997], consisting of two three-axis FGM sensors, measures the magnetic field, used to determine the electron gyrofrequency. The Wideband Data (WBD) instrument [Gurnett *et al.*, 1997, 2001] provides high time and frequency resolution electric and

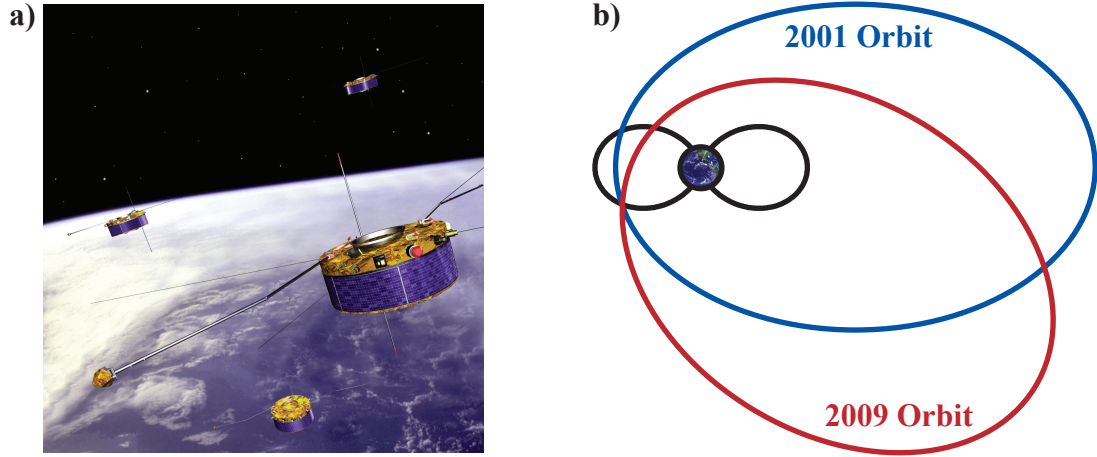


Figure 1.6: a) Cluster mission consisting of four identical spacecraft flying in a tetrahedral formation. Figure courtesy of ESA. b) The highly elliptical orbit of Cluster has been systematically changed over time, with the orbits for the years 2001 and 2009 shown.

magnetic field measurements of ELF/VLF waves, allowing analysis of fine wave structure. The WBD instrument can be connected to one of the four antennas at any given time, though for this study, spectrograms are only created with the electric field measurements. For observations of chorus, the WBD instrument was operated exclusively in the mode with a bandwidth of 9.5 kHz in baseband, a time resolution of $37 \mu\text{sec}$, and a dynamic resolution of 8 bits. The Plasma Electron and Current Experiment (PEACE) [Johnstone *et al.*, 1997] consists of two sensors that provide measurements of energetic electron flux and pitch angle, respectively.

The Spatio-Temporal Analysis of Field Fluctuations (STAFF) instrument [Cornilleau-Wehrlin *et al.*, 2003] consists of a triaxial search coil magnetometer. The Spectrum Analyzer calculates 5×5 Hermitian cross-spectral matrices in real time using the 3 magnetic components of the waves, along with the two electric components measured by the Electric Field and Wave (EFW) instrument [Gustafsson *et al.*, 1997]. These matrices are calculated at 27 frequencies distributed logarithmically in the frequency range 8 Hz to 4 kHz, with a time resolution that varies between 0.125 and 4 seconds. The measurements from STAFF are used to determine wave normal information for chorus elements. Finally, the Waves of High frequency and Sounder for Probing of Electron density by Relaxation (WHISPER)

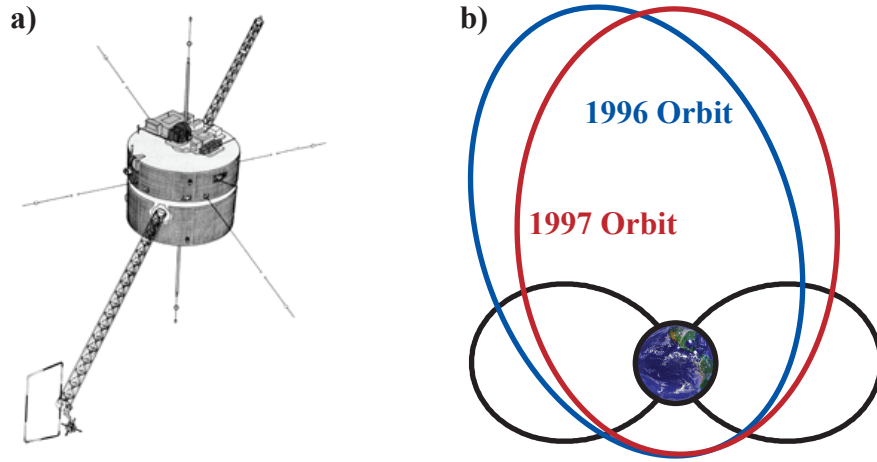


Figure 1.7: a) Polar mission consisting of a single spacecraft. Figure courtesy of NASA. b) The highly elliptical orbit of Polar is shown for the years 1996 and 1997.

instrument [[Décréau et al., 1997, 2001](#); [Trotignon et al., 2001, 2003, 2010](#)] and the EFW instrument are used to determine the electron density and will be discussed in greater detail in Chapter 3.

1.3.2 The Polar Mission

The Polar mission consists of a single spacecraft, shown in Figure 1.7a, launched on February 24, 1996. Operated by the National Aeronautics and Space Administration (NASA), the Polar mission concluded about 12 years later on April 16, 2008. The Polar spacecraft has a highly elliptical, 86° inclination orbit with a period of approximately 17.5 hours, perigee of $1.8R_E$, and apogee of $9R_E$, displayed in Figure 1.7b. The spacecraft, with a mass of 1240 kg, carries 12 instruments, four of which are of interest for this dissertation. The Plasma Wave Instrument (PWI) provides high-resolution plasma wave data within the chorus band. The PWI detects magnetic fields through the use of a triaxial magnetic search coil antenna ($70 \mu\text{V}/\text{nT-Hz}$ sensitivity) and detects electric fields using three orthogonal electric dipole antennas, two in the spacecraft spin plane (100 and 130 m, 6 second period), and one aligned along the spin axis (14 m).

The signals from these antennas are processed by several receiver systems, one of which

is the High Frequency Waveform Receiver (HFWR). Coincident sampling from 20 Hz to 25 kHz of 3 orthogonal components of the electric and magnetic wave fields is provided by the HFWR. In the high-telemetry rate mode, 0.45 second waveform snapshots are recorded from each antenna at intervals spaced 9.2 seconds apart [Gurnett *et al.*, 1995]. The local gyrofrequency was obtained from measurements of the magnetic field from the Magnetic Field Experiment onboard Polar [Russell *et al.*, 1995]. When data was available, the PWI Sweep Frequency Receiver (SFR) was used to extract the electron density from the upper hybrid resonance (described further in Chapter 3) line [Mosier *et al.*, 1973]. The SFR, which covers frequencies in the range of 26 Hz to 808 kHz at higher than one minute resolution, provides continuous data of a single component of the electric and magnetic fields [Gurnett *et al.*, 1995].

1.4 Overview and Contributions

This dissertation is primarily concerned with the use of measurements of ELF/VLF banded chorus from the Cluster and Polar satellites to better understand the source region characteristics of these emissions. In Chapter 2, we describe a new theory which puts forth that banded chorus emissions may be generated within and guided by whistler-mode ducts. In order to test this theory, high resolution electron density is determined to identify ducts in Chapter 3. The relationship between banded chorus and ducts is analyzed in Chapter 4, through the use of wave normal angle distributions near the magnetic equator. In Chapter 5, we further evaluate the wave normal angle distributions of banded chorus in both the equatorial and off-equatorial regions. To assess other characteristics of the source region, we examine the spatial dependence of banded chorus intensity near the magnetic equator in Chapter 6. Finally, we discuss conclusions and suggestions for future research in Chapter 7.

The contributions of this research may be summarized as follows:

1. Provided the first evaluation of a new theory suggesting that the emission gap between the upper and lower bands of chorus is due to ducting effects.
2. Determined the highest spatial resolution plasmaspheric electron densities to date for

accurate identification of whistler-mode ducts.

3. Showed that lower band chorus emissions can be uniformly excited over an extended region near the magnetic equator.
4. Demonstrated that banded chorus can be generated within, and likely guided by, enhancement and depletion ducts.
5. Showed lower band chorus tends to be quasi-field-aligned and upper band chorus tends to have oblique wave normal angles over a magnetic latitude range up to 50° .
6. Provided the first identification and analysis of exponential spatial dependence of banded chorus intensity on magnetic latitude.

Chapter 2

Ducting Theory for Banded Chorus

Chorus often appears in a banded configuration, with an upper band above an emission gap occurring near $f_{ce}/2$ and a lower band below this gap. In this chapter, we describe a new theory suggesting that the two distinct bands of chorus and the emission gap between them are characteristics that arise from the properties of the chorus source region. In particular, we argue that the banded structure of chorus can be explained if the chorus waves are excited within field-aligned whistler-mode ducts of either enhanced or depleted cold plasma density.

Part of the work presented in this chapter has been published in *Geophysical Research Letters* as [Bell et al. \[2009\]](#).

2.1 Whistler-Mode Ducts

In a smooth magnetosphere, without the presence of whistler-mode ducts, a whistler-mode wave transmitted from a ground-based transmitter, as shown in Figure 2.1a, would be preferentially guided approximately along the direction of the ambient magnetic field until it reached the conjugate region, where it would undergo a magnetospheric reflection, if its frequency was less than the local lower hybrid frequency, and remain in the magnetosphere until it eventually dissipated [[Kimura, 1966](#)]. Despite this tendency for whistler-mode waves to reflect internally in a smooth magnetosphere, these waves were often observed on the ground by receivers in the conjugate region in the opposite hemisphere. In order

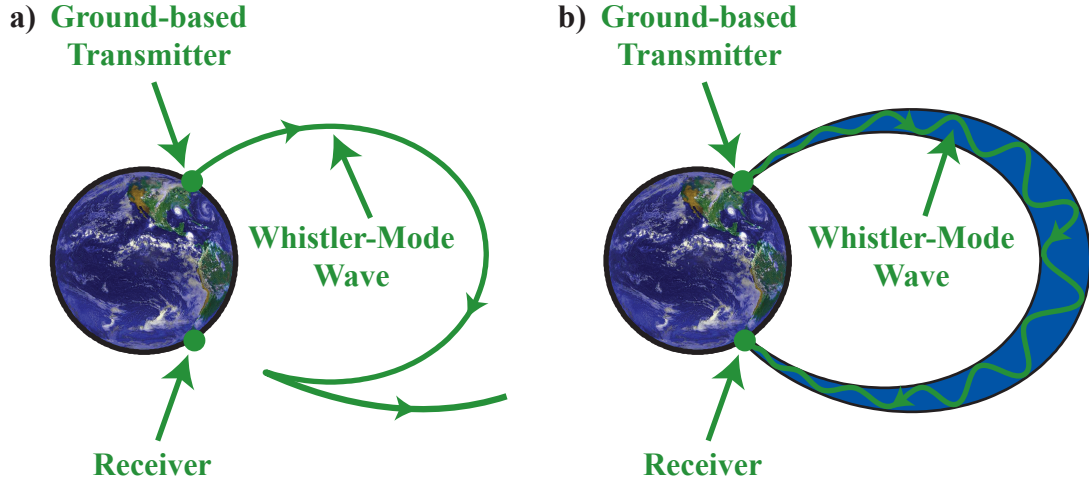


Figure 2.1: a) Whistler-mode wave, in a smooth magnetosphere, guided by magnetic field lines until it reaches the conjugate hemisphere, where it would undergo a magnetospheric reflection. b) To explain the return of these waves to the ground, it was proposed that whistler-mode ducts existed to act as guiding structures for the plasma waves.

to explain these ground-based observations, the existence of whistler-mode ducts in the magnetosphere was proposed [Helliwell, 1965, Sec. 3.6].

Whistler-mode ducts are field-aligned cold electron density irregularities that are able to guide plasma waves. For instance, if a whistler-mode wave is transmitted from a ground-based transmitter, it can be guided within a duct to the conjugate point in the opposite hemisphere, where it can be observed by a receiver, as illustrated in Figure 2.1b. Ducts are guiding structures analogous to optical fibers, which are known to guide light waves over large distances through the principle of total internal reflection. While ducts are plentiful, they only occupy a small percentage of the total magnetospheric volume, and are therefore difficult to detect. Smith and Angerami [1968] showed the first satellite evidence for the existence of ducts through observations of waves whose spectral characteristics changed discretely as a series of ducts was encountered.

In order to identify ducts directly from the electron density data, measurements with high resolution and accuracy are needed. However, such measurements have been unavailable until this study. An example of high resolution electron density data, described in more detail in Chapter 3, as a function of L -shell, is shown in Figure 2.2a. Many irregularities are

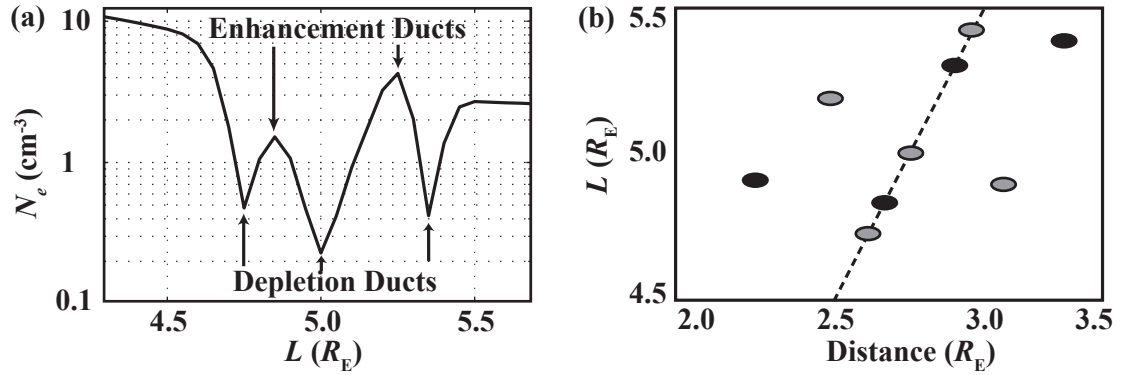


Figure 2.2: a) Electron density versus L -shell in the magnetic equatorial plane with whistler-mode enhancement and depletion ducts. b) Possible arrangement of enhancement (black) and depletion (gray) ducts for L -shell versus East-West distance. Dashed line indicates equatorial projection of Cluster 1 orbit.

observed within this electron density profile. The regions of enhanced electron density are known as enhancement ducts, while the regions of depleted electron density are known as depletion ducts. One possible arrangement of these ducts in the magnetic equatorial plane for L -shell versus East-West distance is seen in Figure 2.2b.

2.2 Commonalities of Three Types of Emissions

Banded chorus emissions are believed to be generated through the cyclotron resonance interaction given by Equation 1.4. This emission generation condition is common to two other processes in the magnetosphere by which emissions are also excited by triggering waves. The first process is the triggering of Auroral Kilometric Radiation (AKR) in the polar regions by background plasma waves [Gurnett, 1974]. AKR is believed to be excited at $f \simeq f_{ce}$ at relatively low altitudes, and thus is observed at much higher frequencies than chorus. However, it generally consists of many discrete narrowband emissions [Gurnett and Anderson, 1981] whose form resembles the form of many chorus emissions, as shown in Figure 2.3a. AKR is believed to be generated within auroral depletion ducts in which the cold plasma density is much less than the local ambient density average.

The second process is the triggering of ELF/VLF emissions in the plasmasphere by

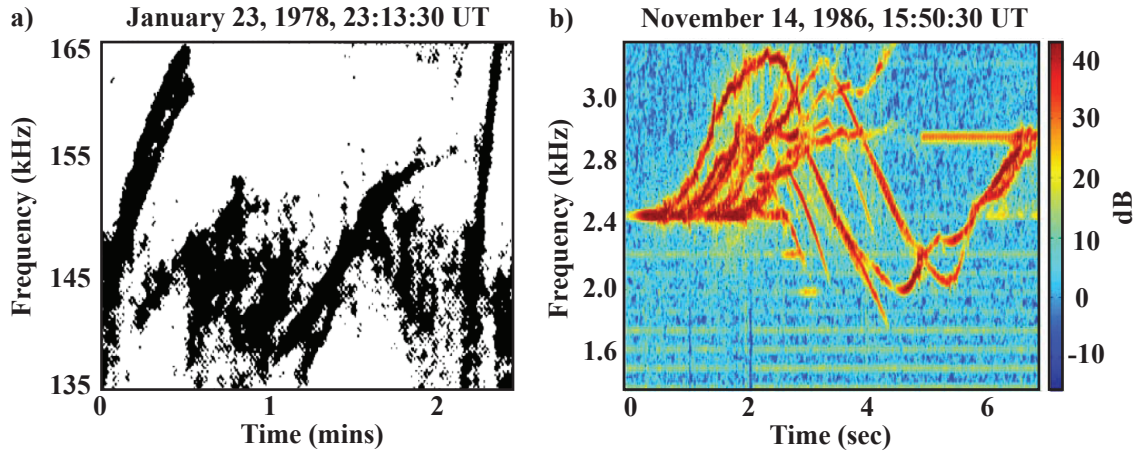


Figure 2.3: a) Spectrogram showing Auroral Kilometric Radiation (AKR) triggered by background plasma waves. AKR consists of discrete narrowband emissions often similar in form to chorus emissions. b) Spectrogram showing a two-second duration fixed-frequency pulse at 2.46 kHz transmitted from Siple Station, as received in the Northern hemisphere at Lake Mistissini. The pulse triggers a series of emissions that closely resemble chorus emissions.

fixed-frequency signals transmitted from ground-based transmitters, such as the one located at Siple Station, Antarctica [[Helliwell and Katsufurakis, 1974](#)], as shown in Figure 2.3b. The instability of the plasma that gives rise to these emissions is known as the Coherent Wave Instability (CWI) because the emissions are triggered only when a coherent ELF/VLF input wave is present as the triggering signal [[Mielke and Helliwell, 1992](#)]. In general, triggered emissions such as these within the plasmasphere closely resemble many chorus emissions triggered outside the plasmasphere [[Pickett et al., 2004](#)]. Two decades of experiments at Siple Station have demonstrated that the CWI takes place within whistler-mode enhancement ducts. In addition, ISEE-1 spacecraft observations showed that only very few ELF/VLF emissions triggered by ground-based ELF/VLF transmitter signals were triggered outside whistler-mode ducts [[Bell et al., 1981](#)]. These findings lead to the conclusion that the CWI takes place predominantly within whistler-mode ducts.

Noting that the three types of emissions are generated through the same cyclotron resonance interaction, that many of the frequency-time characteristics of the emissions are similar, and that two of the three types of emissions are excited within either depletion or enhancement ducts, it appears reasonable to suggest that the third type of emissions,

ELF/VLF banded chorus, is also excited predominantly within either depletion or enhancement ducts. This theory leads to an explanation for the banded structure of chorus.

2.3 Refractive Index

A parameter used in describing the ducting theory for banded chorus is the refractive index, which is the ratio of the speed of light in a vacuum relative to that in the considered medium. The refractive index vector is expressed as

$$\boldsymbol{\mu} = \frac{\mathbf{k}c}{\omega} \quad (2.1)$$

for a wave in an arbitrary medium, with the coordinate system as defined in Figure 1.5b. In free space, the refractive index is a scalar with $\mu = |\boldsymbol{\mu}| = 1$, while in a cold magnetized plasma, the refractive index is a vector and is a function of the plasma frequency, gyrofrequency, frequency of the wave, and the polar wave normal angle with respect to \mathbf{B}_0 .

The refractive index for a cold, collisionless, magnetized plasma is derived following the approach of several textbooks [e.g., *Stix, 1992*]. To obtain a linear set of equations, the dependent variables are assumed to consist of a constant uniform zero order term plus a small first order perturbation. The dependent variables include the particle velocity (\mathbf{v}_s), electric field (\mathbf{E}), magnetic field (\mathbf{B}), and particle density (N_s), where s denotes the particle species. Considering the variables \mathbf{v} and \mathbf{E} to be first order perturbations, \mathbf{B} and N_s are represented as

$$\mathbf{B}(\mathbf{r}, t) = \mathbf{B}_0 + \mathbf{B}_1(\mathbf{r}, t) \quad (2.2)$$

$$N_s(\mathbf{r}, t) = N_{s0} + N_{s1}(\mathbf{r}, t). \quad (2.3)$$

The Fourier transform of the linearized Maxwell's equations and Lorentz force equation are then expressed as

$$-j\omega m_s \mathbf{v} = q_s(\mathbf{E} + \mathbf{v} \times \mathbf{B}_0) \quad (2.4)$$

$$\mathbf{k} \times \mathbf{E} = \omega \mathbf{B}_1 \quad (2.5)$$

$$j\mathbf{k} \times \mathbf{B}_1 = \mu_0(q_s N_{s0} \mathbf{v} - j\omega \epsilon_0 \mathbf{E}), \quad (2.6)$$

where $j \equiv \sqrt{-1}$.

Without loss of generality, the coordinate system can be rotated such that \mathbf{B}_0 is in the z direction and the refractive index vector is in the $x-z$ plane at an angle θ relative to \mathbf{B}_0 . Equations 2.4, 2.5, and 2.6 remain a closed set of equations even with an increase in the number of species, which would increase the number of equations and unknowns. Solving this set of equations yields

$$\begin{bmatrix} S - \mu^2 \sin^2 \theta & -jD & \mu^2 \sin \theta \cos \theta \\ jD & S - \mu^2 & 0 \\ \mu^2 \sin \theta \cos \theta & 0 & P - \mu^2 \sin^2 \theta \end{bmatrix} \begin{bmatrix} E_x \\ E_y \\ E_z \end{bmatrix} = 0, \quad (2.7)$$

where

$$S = \frac{R + L}{2} \quad (2.8)$$

$$D = \frac{R - L}{2} \quad (2.9)$$

$$P = 1 - \sum_s \frac{f_{ps}^2}{f^2} \quad (2.10)$$

$$R = 1 - \sum_s \frac{f_{ps}^2}{f(f + f_{cs})} \quad (2.11)$$

$$L = 1 - \sum_s \frac{f_{ps}^2}{f(f - f_{cs})}. \quad (2.12)$$

The quantities f_{cs} and f_{ps} are the cyclotron and plasma frequencies for the s particle species, respectively, and are expressed as

$$f_{cs} = \frac{q_s B_0}{2\pi m_s} \quad (2.13)$$

$$f_{ps} = \frac{|q_s|}{2\pi} \sqrt{\frac{N_s}{m_s \epsilon_0}}, \quad (2.14)$$

where q_s carries a sign.

Equation 2.7 has a non-trivial solution if and only if the determinant of the matrix is

zero, producing the dispersion relation

$$A\mu^4 - B\mu^2 + C = 0, \quad (2.15)$$

where

$$A = S\sin^2\theta + P\cos^2\theta \quad (2.16)$$

$$B = RL\sin^2\theta + PS(1 + \cos^2\theta) \quad (2.17)$$

$$C = RLP. \quad (2.18)$$

Solving the quadratic equation for μ^2 gives

$$\mu^2 = \frac{B \pm F}{2A}, \quad (2.19)$$

where

$$F^2 = (RL - PS)^2\sin^4\theta + 4P^2D^2\cos^2\theta. \quad (2.20)$$

Neglecting the effects of ions and collisions, the refractive index can be approximated by the Appleton-Hartree equation

$$\mu^2 = 1 - \frac{\frac{f_{pe}^2}{f^2}}{1 - \frac{f_{ce}^2\sin^2\theta}{2(f^2 - f_{pe}^2)} \pm \sqrt{\left(\frac{f_{ce}^2\sin^2\theta}{2(f^2 - f_{pe}^2)}\right)^2 + \frac{f_{ce}^2}{f^2}\cos^2\theta}} \quad (2.21)$$

[[Appleton, 1932](#)]. If it is further assumed $f^2 \ll f_{pe}^2$ and $f_{ce}^2 \ll f_{pe}^2$, conditions that generally hold true in the inner magnetosphere, the refractive index is given by

$$\mu \simeq \frac{f_{pe}}{\sqrt{f_{ce}f\left(\cos\theta - \frac{f}{f_{ce}}\right)}} \simeq \frac{q}{2\pi} \sqrt{\frac{N_e}{m\epsilon_0 f_{ce}f\left(\cos\theta - \frac{f}{f_{ce}}\right)}} \quad (2.22)$$

[[Smith et al., 1960](#)].

A useful representation of the refractive index is a polar plot of the refractive index as a function of the wave normal angle, which is commonly referred to as the refractive

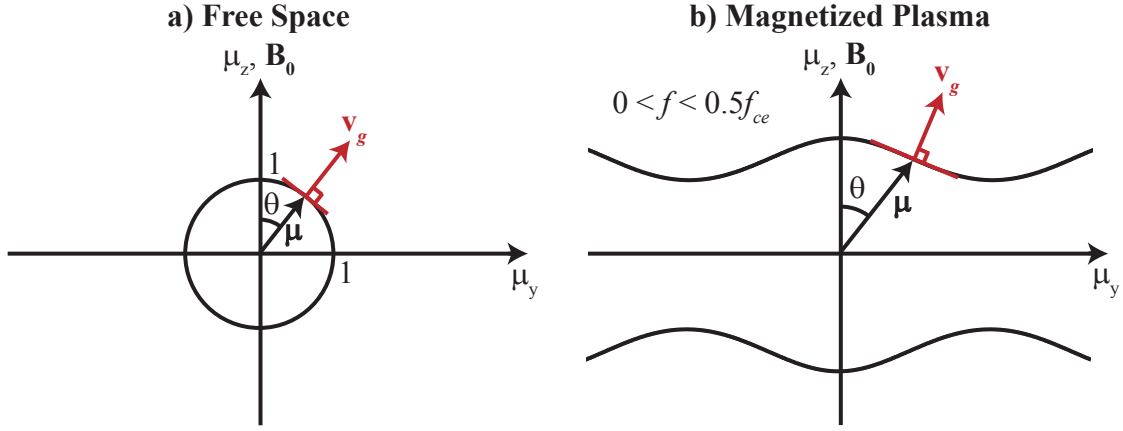


Figure 2.4: Refractive index surfaces showing the refractive index (μ) as a function of the wave normal angle (θ) for a) free space and b) a cold magnetized plasma. The axes represent the transverse and parallel components of the refractive index with respect to B_0 . The direction of the group velocity (v_g) is in the same direction as θ for isotropic media like free space, but generally in a different direction for anisotropic media like the magnetosphere.

index surface, and which is a contour with a surface of revolution about the magnetic field. The refractive index surfaces for free space and a cold magnetized plasma are shown in Figure 2.4. In free space, the refractive index surface is a sphere with unit magnitude, while in a magnetized plasma, the refractive index surface takes on a much different shape. The particular refractive index surface shown in Figure 2.4b is for frequencies below $f_{ce}/2$.

For an isotropic medium such as free space, the energy of the wave, indicated by the direction of the group velocity vector (v_g), travels in the same direction as the wave vector k as described by the wave normal angle θ . For an anisotropic medium such as the magnetosphere, the energy of the wave generally travels in a direction different than θ . Using the refractive index surface, the direction of the group velocity is given as the direction normal to the surface at the tip of the refractive index vector [Poevlerlein, 1948]. The minimum nonzero wave normal angle for which the group velocity is parallel to the magnetic field is defined as the Gendrin angle [Gendrin, 1960, 1961], shown in Figure 2.5.

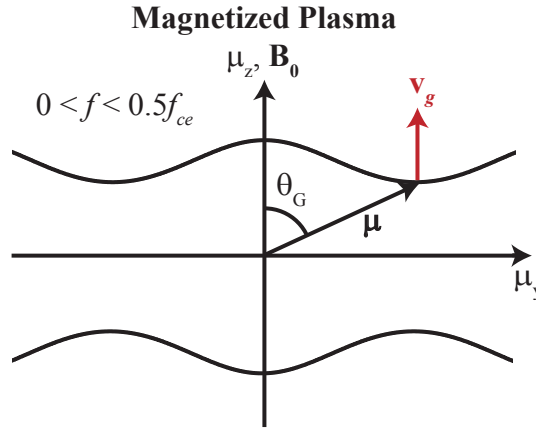


Figure 2.5: Refractive index surface for a cold magnetized plasma showing the Gendrin angle (θ_G), defined as the minimum nonzero wave normal angle for which \mathbf{v}_g is parallel to \mathbf{B}_0 .

2.4 Guidance by Whistler-Mode Ducts

Chorus waves can be guided by whistler-mode ducts of either depleted or enhanced electron density. Figure 2.6b shows an electron density profile, with electron density varying only in the direction perpendicular to \mathbf{B}_0 . The electron density profile exhibits a region of depleted electron density that acts as a depletion duct. The grayscale in the background is another representation of the electron density, with darker shades of gray indicating increasing values of electron density. The three particular electron density points on the electron density profile are used to determine the color coded refractive index surfaces seen in Figure 2.6a.

A Snell's law construction of the refractive index surfaces in Figure 2.6a, typical of frequencies in the range $f_{ce}/2 < f < f_{ce}$, can be used to determine the direction of reflected and transmitted waves at a boundary between different media. According to Snell's law, if a boundary is assumed parallel to \mathbf{B}_0 , then the projection of the refractive index along this boundary must be the same for different media. Assuming an initial wave normal angle θ and the lowest value of electron density in the electron density profile (denoted by blue), θ intersects the refractive index at point P. The normal to the boundary, denoted by the dashed line in Figure 2.6a, is drawn through point P. The intersections of this normal with the refractive index surfaces represent the possible transmitted and reflected waves. For each

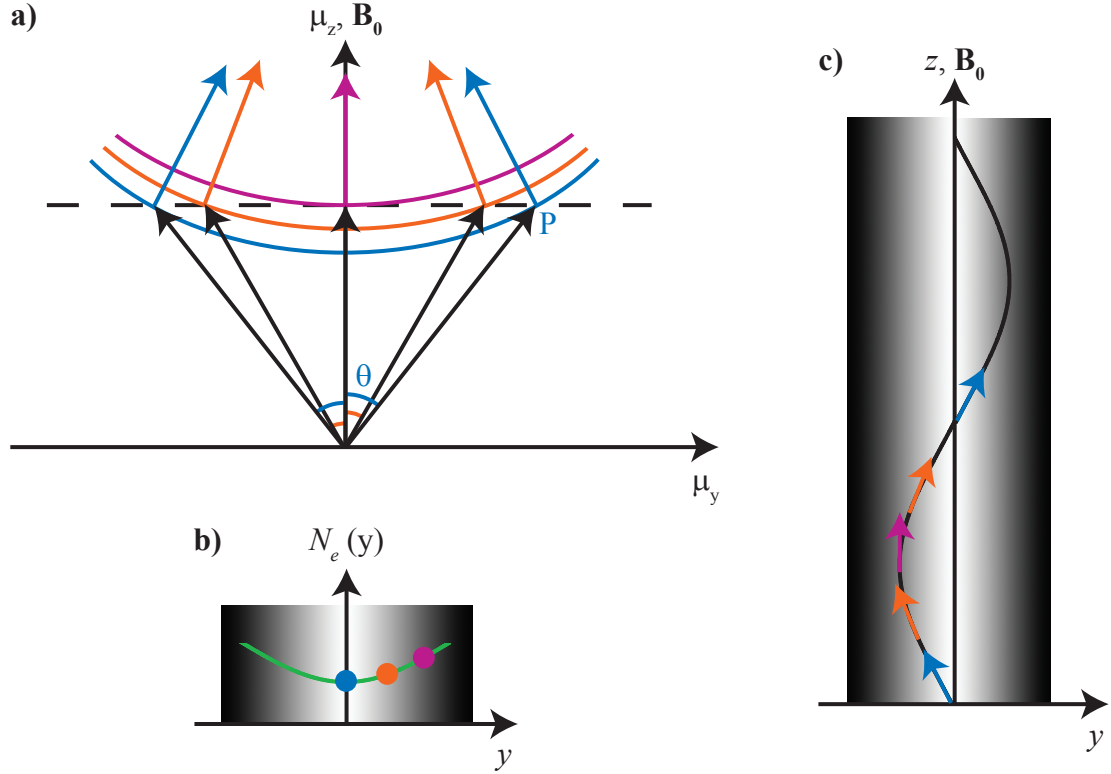


Figure 2.6: a) Snell's law construction of refractive index surfaces color coded to the points on b) the electron density profile and c) the ray path. The electron density profile shows a depletion duct and a grayscale representation of the electron density in the background, with darker shades of gray indicating increasing electron densities. Assuming an initial wave normal angle θ , the intersection of the normal (dashed line) to the boundary (assumed to be parallel to \mathbf{B}_0) through point P with the refractive index surfaces indicate the possible reflected and transmitted waves. The ray path associated with these intersections shows that the chorus waves will be trapped within the depletion duct.

intersection, the direction of the energy of the wave, or the ray direction, is perpendicular to the refractive index surface at the tip of the refractive index vector.

Starting with the initial wave normal angle θ , the direction of the ray, corresponding in color to the electron density and refractive index surface, at each intersection, moving from right to left, is traced in Figure 2.6c, with the electron density grayscale shown in the background. While the wave normal angle always rotates in the direction of increasing refractive index, the behavior of the ray is different depending on whether the wave is in an enhancement or depletion duct. For a depletion duct, the ray rotates in the opposite sense of the wave normal angle, meaning it rotates away from regions of higher refractive index. The ray path in Figure 2.6c shows the ray first moving away from the central magnetic field line, until the ray becomes parallel to \mathbf{B}_0 at $\theta = 0^\circ$, reaching its maximum lateral excursion. After this point, the ray moves back toward the magnetic field line following a ray path that is the mirror image of the lower half about a horizontal line, due to the symmetry of the refractive index surface. Returning to the initial point on the electron density profile, the ray is now on the other side of the magnetic field line. If a similar process were used for the left side of the electron density profile in Figure 2.6b, the rays would follow the path on the right side of the magnetic field shown in Figure 2.6c. The ray path shows that the chorus waves are trapped within the depletion duct, as the rays propagate closely along the magnetic field in a snake-like manner.

Following a process similar to that for the depletion duct, the refractive index surfaces, typical of frequencies $f \rightarrow 0$, electron density profile, and ray path for waves trapped in an enhancement duct are shown in Figure 2.7. For this case, however, the ray rotates in the same direction as the wave normal angle, which is in the direction of increasing refractive index. Similar to the case of the depletion duct, the rays for an enhancement duct also propagate closely along the magnetic field in a snake-like manner, showing that the chorus waves will be trapped within the enhancement duct.

The ray path can also be computed through numerical integration of a closed set of first order differential equations [Haselgrove, 1955]. The set of equations [Kimura, 1966] are expressed as

$$\frac{\partial r}{\partial t} = \frac{1}{\mu^2} \left(\rho_r - \mu \frac{\partial \mu}{\partial \rho_r} \right) \quad (2.23)$$

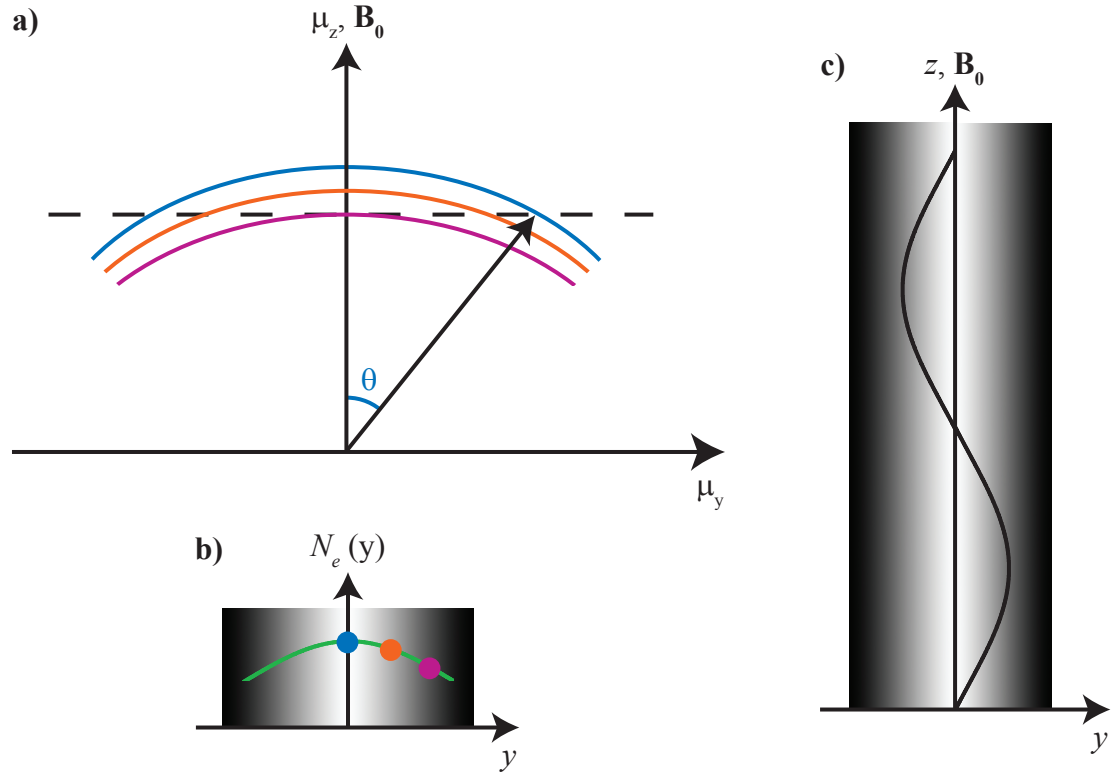


Figure 2.7: a) Snell's law construction of refractive index surfaces color coded to the points on b) the electron density profile and c) the ray path. The electron density profile shows an enhancement duct and a grayscale representation of the electron density in the background, with darker shades of gray indicating decreasing electron densities. The ray path associated with the intersections of the normal (dashed line) to the boundary (assumed to be parallel to B_0) with the refractive index surfaces shows that the chorus waves are trapped within the enhancement duct.

$$\frac{\partial \psi}{\partial t} = \frac{1}{r\mu^2} \left(\rho_\psi - \mu \frac{\partial \mu}{\partial \rho_\psi} \right) \quad (2.24)$$

$$\frac{\partial \gamma}{\partial t} = \frac{1}{r\mu^2 \sin \psi} \left(\rho_\gamma - \mu \frac{\partial \mu}{\partial \rho_\gamma} \right) \quad (2.25)$$

$$\frac{\partial \rho_r}{\partial t} = \frac{1}{\mu} \frac{\partial \mu}{\partial r} + \rho_\psi \frac{\partial \psi}{\partial t} + \rho_\gamma \frac{\partial \gamma}{\partial t} \sin \psi \quad (2.26)$$

$$\frac{\partial \rho_\psi}{\partial t} = \frac{1}{r} \left(\frac{1}{\mu} \frac{\partial \mu}{\partial \psi} - \rho_\psi \frac{\partial r}{\partial t} + r \rho_\gamma \frac{\partial \gamma}{\partial t} \cos \psi \right) \quad (2.27)$$

$$\frac{\partial \rho_\gamma}{\partial t} = \frac{1}{r \sin \psi} \left(\frac{1}{\mu} \frac{\partial \mu}{\partial \gamma} - \rho_\gamma \frac{\partial r}{\partial t} \sin \psi - r \rho_\psi \frac{\partial \psi}{\partial t} \cos \psi \right), \quad (2.28)$$

where r , ψ , and γ are the geocentric distance, colatitude ($90^\circ - \lambda$), and longitude, respectively, ρ_r , ρ_ψ , and ρ_γ are the components of the refractive index vector, which has a length μ , and t is the variable of integration in units of distance. The group delay time, T , gives the rate of energy travel along the ray and is expressed as

$$\frac{dT}{dt} = \frac{1}{c} \left(1 + \frac{f}{\mu} \frac{\partial \mu}{\partial f} \right). \quad (2.29)$$

The ray tracing equations, Equations 2.23 to 2.29, determine the variation of the ray path as a function of time in a slowly varying medium.

2.5 Ducting of Chorus Waves

The ducting theory for banded chorus emissions can now be introduced. Figure 2.8a shows a typical refractive index surface for $0 < f < f_{ce}/2$, which corresponds to the frequencies of LB chorus waves. LB chorus can be guided by enhancement ducts for $\theta < \theta_G$ and by depletion ducts for $\theta \gtrsim \theta_G$. The typical refractive index surface for UB chorus waves, corresponding to the frequency range $f_{ce}/2 < f < f_{ce}$, is different than that for LB chorus waves and is shown in Figure 2.8b. UB chorus can be guided by depletion ducts for all θ . The typical refractive index surface for $f \rightarrow f_{ce}/2$ is shown in Figure 2.9. Since the chorus waves cannot be guided by ducts when $f = f_{ce}/2$, an emission gap between the two chorus bands exists, providing a natural explanation for the banded structure of chorus.

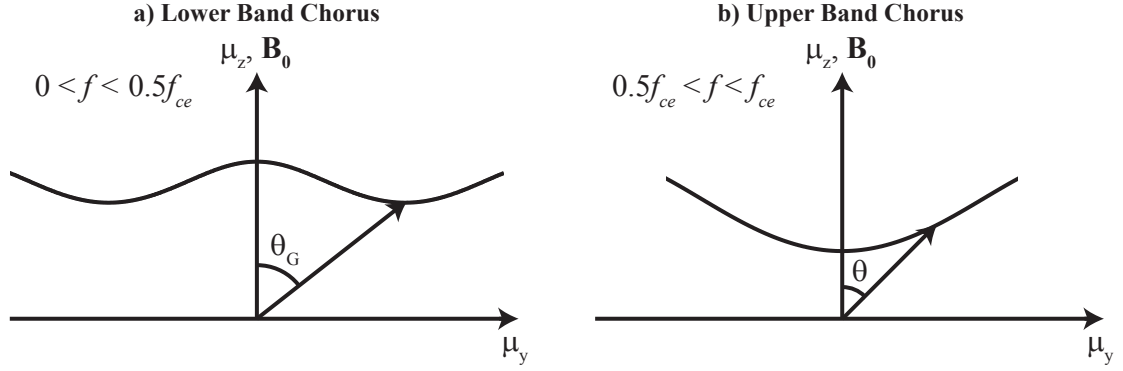


Figure 2.8: Refractive index surfaces for a) LB chorus and b) UB chorus. LB chorus can be guided by enhancement ducts for $\theta < \theta_G$ and by depletion ducts for $\theta \gtrsim \theta_G$, while UB chorus can be guided by depletion ducts for all θ .

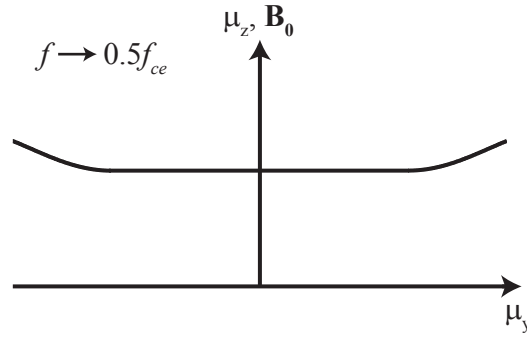


Figure 2.9: Refractive index surface as $f \rightarrow f_{ce}/2$. Since the chorus waves cannot be guided by ducts when $f = f_{ce}/2$, an emission gap between the two chorus bands exists, providing a natural explanation for the banded structure of chorus.

The conditions for guidance by whistler-mode ducts assume that the ducts are isolated, that N_e varies smoothly in the plane perpendicular to \mathbf{B}_0 , and that gradients in \mathbf{B}_0 and N_e along the direction of \mathbf{B}_0 are negligible. If the curvature of \mathbf{B}_0 and the gradient of N_e along \mathbf{B}_0 are included, the upper cutoff frequency of LB chorus is further reduced below $f_{ce}/2$, while the lower cutoff frequency of UB chorus is relatively less affected. The actual ducts in the chorus source region may not always conform to the assumption that the ducts are isolated, as illustrated in Figure 2.2a.

Although the ducts in which the triggered emissions as observed on the ground are excited must necessarily extend between conjugate hemispheres, this does not have to hold for the ducts in which banded chorus is excited. The dimensions of the chorus source region is believed to have a scale of ~ 100 km perpendicular to \mathbf{B}_0 and a scale of ~ 1000 km parallel to \mathbf{B}_0 [Helliwell, 1967; Trakhtengerts, 1999; Inan et al., 2003; Santolík and Gurnett, 2003; Santolík et al., 2004]. The length of the duct along \mathbf{B}_0 may be determined using the repetition rate of periodic chorus elements. The LB chorus of Figure 1.4 consists of similar elements with linearly increasing frequency with a repetition rate of 4 to 10 per second. This periodic behavior is consistent with chorus excitation within whistler-mode ducts. For example, as a chorus emission exits the duct, a small internally reflected component may propagate back to the other end of the duct where a second small internal reflection may take place. This twice reflected component may then act as a seed wave that triggers a second chorus emission. This process then repeats to produce periodic chorus elements. For a duct with length 1500 km along \mathbf{B}_0 and for a group velocity $v_g \simeq c/20$, the repetition rate of the chorus emissions would be ~ 5 per second, consistent with the rates for LB chorus in Figure 1.4.

2.6 Summary

Noting the commonality of banded chorus with two other types of emissions that are known to be excited within ducts, a new theory suggests that banded chorus is also excited within ducts. LB chorus can be guided by enhancement ducts for $\theta < \theta_G$ and by depletion ducts for $\theta \gtrsim \theta_G$, while UB chorus can be guided by depletion ducts for all θ . This theory provides a natural explanation for the banded structure of chorus, since chorus waves cannot be

guided by ducts when $f = f_{ce}/2$, causing an emission gap to exist at this frequency. If banded chorus is excited within whistler-mode ducts, then these ducts must be accurately identified and studied using high resolution electron density measurements. Such a study is the subject of the remaining chapters of this dissertation.

Chapter 3

Determination of Electron Density

We have shown in the previous chapter that the source region of banded chorus emissions consists of whistler-mode ducts of depleted electron density for UB chorus for all θ and ducts of either enhanced or depleted electron density for LB chorus for $\theta < \theta_G$ and $\theta \gtrsim \theta_G$, respectively. In order to test this theory, N_e must be characterized with high accuracy and with a spatial resolution of ~ 25 km or less to identify whistler-mode ducts. However, such measurements have previously been unavailable. In this chapter, we describe the process to determine high resolution electron densities using instruments onboard Cluster and the process to identify ducts.

Part of the work presented in this chapter has been published in *Geophysical Research Letters* as [Haque et al. \[2011\]](#).

3.1 Cluster Instruments

The electron density is determined using measurements from two instruments onboard the Cluster spacecraft: the Electric Field and Wave (EFW) instrument [[Gustafsson et al., 1997](#)] and the Waves of HIgh frequency and Sounder for Probing of Electron density by Relaxation (WHISPER) instrument [[Décr  au et al., 1997, 2001](#); [Trotignon et al., 2001, 2003, 2010](#)].

3.1.1 EFW

The EFW instrument uses two long double sphere electric field antennas, shown in Figure 3.1, which consist of four orthogonal cable booms (50 m long) with a spherical sensor (8 cm in diameter) at each end in the spacecraft spin plane. EFW can be operated in a mode to measure the spacecraft potential, U , with a time resolution of 0.2 seconds. Since the sensors are artificially biased near the potential of the ambient plasma, the measured potential difference between the sensor and the spacecraft is approximately the negative value of the spacecraft potential with respect to the ambient plasma. Using this fact, the plasma frequency can be estimated with the empirical formula

$$f_{pe} = 9\sqrt{a(-U)^b}, \quad (3.1)$$

where a and b are empirical parameters. It is initially assumed that $a = 200$ and $b = -1.85$, based on results from large statistical studies. Though EFW has a relatively high time resolution, as compared to WHISPER, its data cannot be used without being calibrated by the data obtained from WHISPER.

3.1.2 WHISPER

The WHISPER instrument measures the amplitude of frequencies in the range of 2 to 80 kHz and uses the two EFW antennas to transmit and receive electric field signals. The EFW boom cables are composed of several wires including a conductive outer braid, which is connected to the WHISPER transmitter. High-impedance preamplifiers, located close to the spherical sensors, provide signals to the WHISPER receiver electronic board. WHISPER operates in two different modes: passive and active. In the passive mode, the transmitter is turned off and WHISPER acts as a natural wave receiver, only monitoring natural electric emissions.

In the active mode, WHISPER acts like a topside sounder, as illustrated in Figure 3.2. The radio wave transmitter, connected to one of the electric field antennas of EFW, transmits a 1 ms pulse at a certain frequency. This pulse induces a signal within the surrounding plasma, which is observed by the receiver. This process is repeated for different frequencies

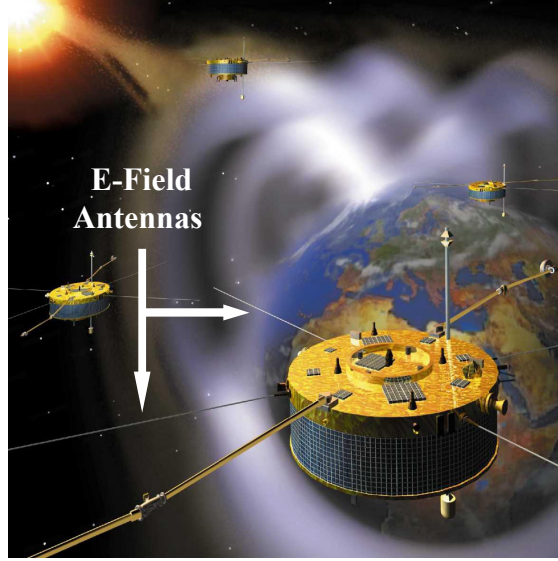


Figure 3.1: The two long double sphere electric field antennas of the EFW instrument located in the spacecraft spin plane. The antennas consist of four orthogonal cable booms with a spherical sensor at each end. Figure courtesy of ESA.

until the entire bandwidth of WHISPER is covered. Two active spectra, separated by 1.12 seconds, are available every 52 seconds. During these 52 seconds, only passive spectra are available, separated by 1.7 seconds.

3.2 Resonances in the Magnetosphere

When WHISPER operates in the active mode, it often transmits a pulse at a frequency close to the characteristic frequencies of the plasma, causing very intense echoes to be received. These stimulated signals are known as resonances, many different kinds of which are observed in the magnetosphere. The resonances observed include the plasma frequency, f_{pe} , the gyrofrequency, f_{ce} , and its harmonics, nf_{ce} , where n is the harmonic number, Bernstein mode frequencies, f_{qn} , and the upper hybrid resonance frequency, defined as

$$f_{uh} = \sqrt{f_{pe}^2 + f_{ce}^2}. \quad (3.2)$$

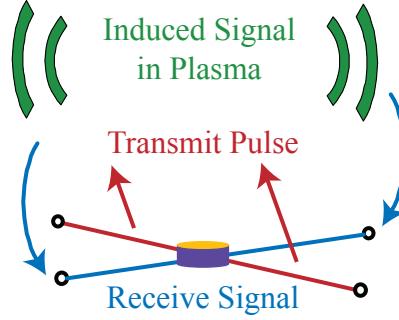


Figure 3.2: WHISPER operating in the active mode. One electric antenna transmits a pulse at a certain frequency, inducing a signal within the surrounding plasma, while the other antenna observes the induced signal. This process is repeated for the different frequencies of the WHISPER bandwidth.

The Bernstein modes [Bernstein, 1958] are quasi-electrostatic waves with dispersion relations that are a function of f_{pe} . The function $\alpha(q, \Lambda)$ is defined as

$$\alpha(q, \Lambda) = 2 \sum_{m=1}^{\infty} e^{-\Lambda} I_m(\Lambda) \frac{m^2}{q^2 - m^2}, \quad (3.3)$$

where $q = f/f_{ce}$, $\Lambda = k^2 \rho^2$, ρ is the gyroradius, and $I_m(\Lambda) = I_{-m}(\Lambda)$ is the Bessel function of the first kind of imaginary argument. The dispersion relation can be expressed as

$$\alpha = \frac{\Lambda f_{ce}^2}{f_{pe}^2}. \quad (3.4)$$

The roots of the dispersion relation are the intersections of the function $\alpha(q, \Lambda)$ with the horizontal line $\alpha = \Lambda f_{ce}^2 / f_{pe}^2$. The function $\alpha(q, \Lambda)$ is plotted as a function of q for $\Lambda = 0.1$ and $\Lambda = 5$ in Figure 3.3.

In order to identify N_e with the highest level of accuracy, the resonances were manually identified for each active spectrum. Occasionally, f_{pe} can be directly identified from the active spectra or indirectly through f_{uh} . More often, however, neither frequency is identifiable and f_{pe} must be determined using $n f_{ce}$ and f_{qn} . An individual active spectrum from WHISPER on the Cluster 2 spacecraft is shown in Figure 3.4a. Many spikes in amplitude are seen in the spectrum, which correspond to different resonances. A first estimate of f_{ce}

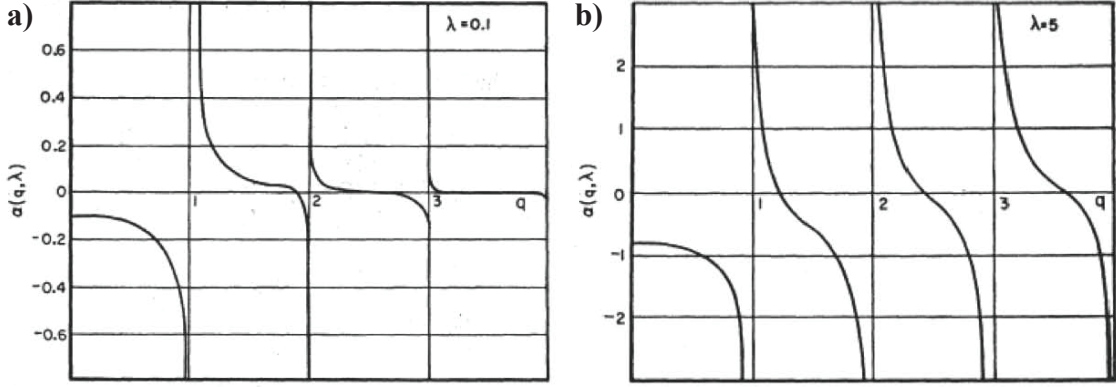


Figure 3.3: The function $\alpha(q, \Lambda)$ plotted as a function of q for a) $\Lambda = 0.1$ and b) $\Lambda = 5$. The intersections of $\alpha(q, \Lambda)$ with the horizontal line $\alpha = \Lambda f_{ce}^2 / f_{pe}^2$ give the roots of the dispersion relation. Figure from [Bernstein \[1958, Figs. 1 and 3\]](#).

is calculated using the value of the magnetic field as determined by the FGM instrument and is found to be ~ 20 kHz. The second and third gyroharmonics are observed at ~ 40 and ~ 60 kHz, respectively. Two Bernstein modes, of orders 2 and 3, are also observed occurring between the gyroharmonics.

The gyroharmonics and Bernstein modes can be used to determine f_{pe} from Hamelin's diagram [[Hamelin, 1978](#)], shown in Figure 3.4b. This diagram shows the difference between the Bernstein mode and gyroharmonic of the same order as a function of f_{pe} , where both axes are normalized to f_{ce} . The differences for the second and third order harmonics in Figure 3.4a, normalized by f_{ce} , correspond to the points on the curves for $n=2$ and $n=3$ in Figure 3.4b, respectively. The location at which the normalized differences vertically align indicates the value of f_{pe}/f_{ce} , which gives the value of f_{pe} since f_{ce} is known. It should be noted, however, that this vertical alignment only occurs for plasmas with Maxwellian distributions, such as the magnetospheric cold plasma.

3.3 Calculation of Electron Density

The electron density can be calculated from the plasma frequency with the highest resolution and accuracy using measurements from both the EFW and WHISPER instruments. If only WHISPER measurements are used, N_e would have a spatial resolution of ~ 250 km,

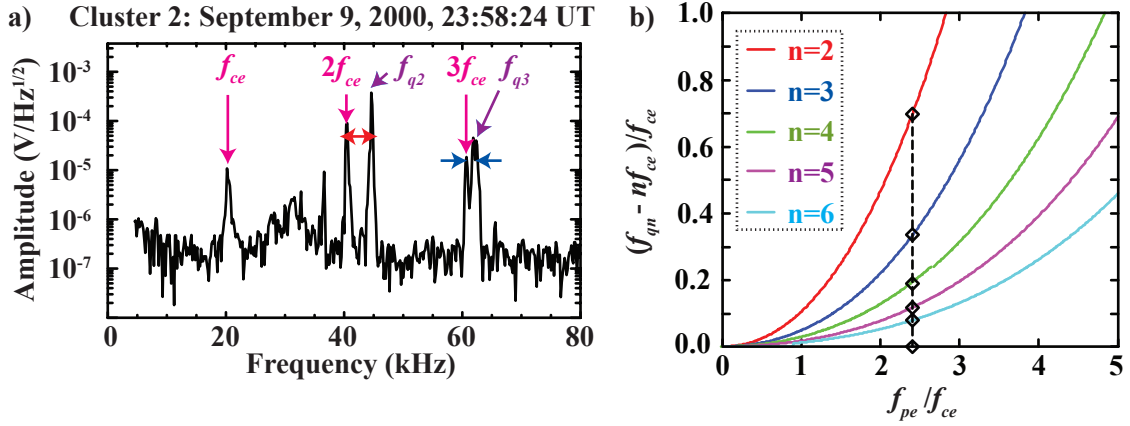


Figure 3.4: a) Individual active spectrum from WHISPER on the Cluster 2 spacecraft with amplitude as a function of frequency. Different resonances, including the gyroharmonics and Bernstein modes, are observed. b) Hamelin's diagram showing the separation between f_{qn} and nf_{ce} as a function of f_{pe} , with both axes normalized to f_{ce} . Each curve corresponds to one of the harmonics, with the harmonic number, n , indicated by the legend. The vertical alignment of the diamonds indicates the value of f_{pe} . Figure adapted from [Trotignon et al. \[2001, Figs. 3 and 4\]](#).

given a Cluster orbital velocity of ~ 5 km/s. For this reason, data from EFW is used to increase the resolution of N_e . The spectrogram from Cluster 1 in Figure 3.5a shows f_{pe} as determined from both the passive and active measurements of WHISPER and the uncalibrated f_{pe} as determined from EFW. The observed f_{pe} from the natural spectra is used to calibrate f_{pe} from EFW. This calibrated f_{pe} is then interpolated between the f_{pe} points manually determined by the active spectra of WHISPER. The total f_{pe} , which passes through the active measurements of f_{pe} from WHISPER, is shown in Figure 3.5b. The electron density can be calculated from the plasma frequency, using the formula

$$N_e = m\epsilon_0 \left(\frac{2\pi f_{pe}}{q} \right)^2, \quad (3.5)$$

where m and q are the mass and charge of the electron, respectively. Using this process, N_e has the highest L -shell resolution to date of ~ 17 km, a time resolution of 0.2 seconds, and an amplitude resolution accuracy of 1% [[Canu et al., 2001](#); [Trotignon et al., 2003](#)].

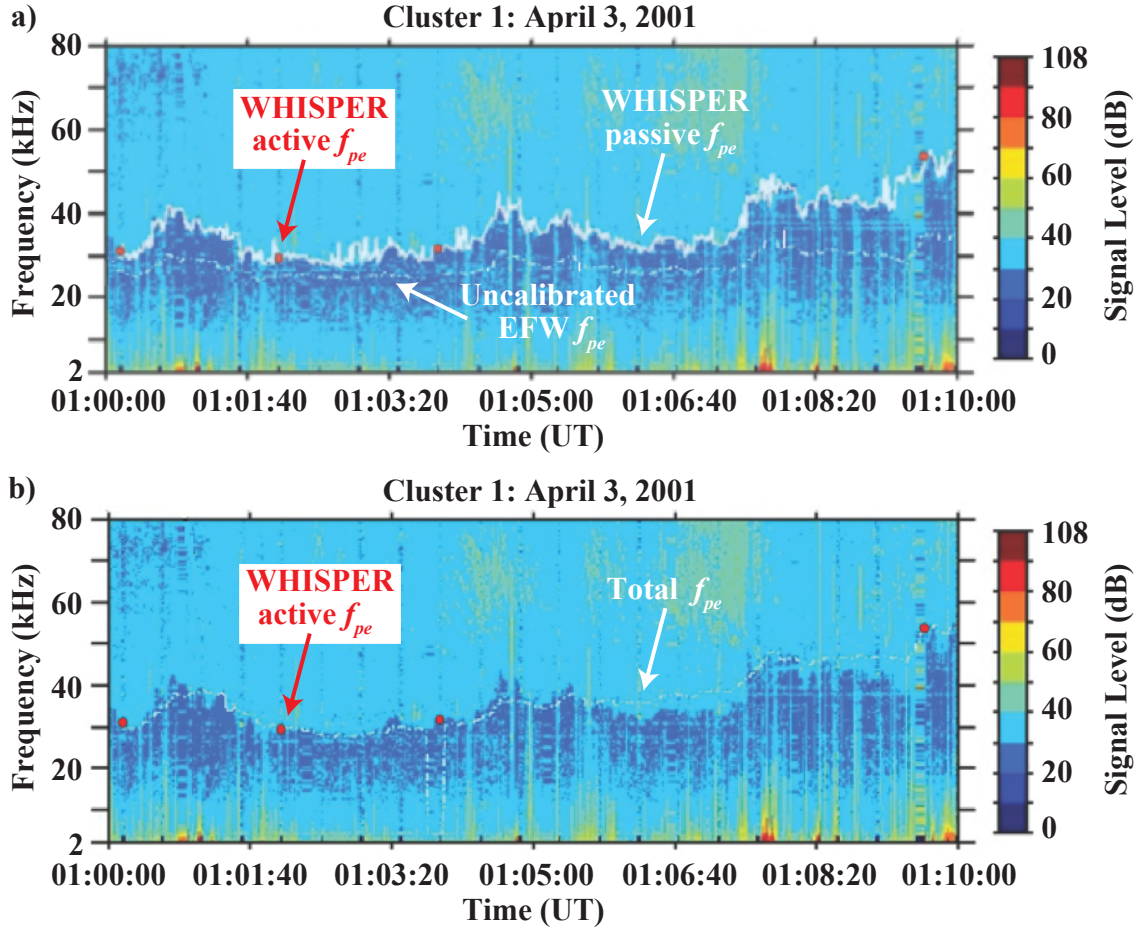


Figure 3.5: a) Spectrogram showing f_{pe} from active and passive measurements of WHISPER and uncalibrated f_{pe} from EFW. Measurements from WHISPER are interpolated with those from EFW to determine b) the total f_{pe} , which is used to calculate N_e . Color scale indicates signal level in dB.

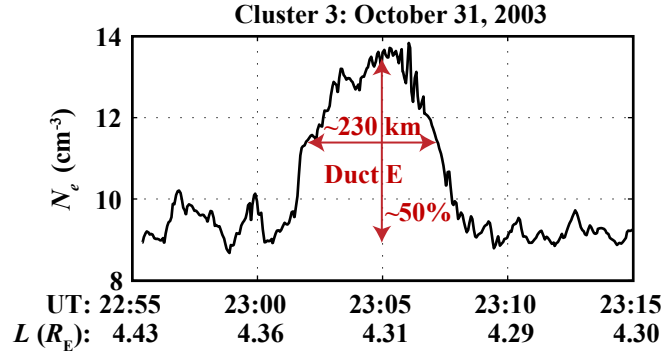


Figure 3.6: Electron density as a function of time and L -shell. An irregularity that satisfies both ducting requirements is the enhancement duct denoted by Duct E. The half-width of Duct E, shown by the horizontal red line, is ~ 230 km and the relative change in electron density, shown by the vertical red line, is $\Delta N_e/N_e \sim 50\%$.

3.4 Ducting Requirements

An example of an electron density profile determined through the above process is shown in Figure 3.6 for the Cluster 3 spacecraft. As there are many irregularities seen in this profile, there must be a method to determine which of these qualify as whistler-mode ducts. There are two requirements that must be satisfied in order for an irregularity to qualify as a duct. The first requirement involves $\Delta N_e/N_e$, which is the enhancement or depletion factor of the electron density with respect to the background level. It is assumed that an irregularity must have $\Delta N_e/N_e \geq 10\%$ to efficiently guide a wave, based on previous studies [Angerami, 1970]. The second requirement involves the half-width, the width of the duct at which the density enhancement is half its maximum value. The half-width is determined from the electron density profile as a function of L -shell, after the electron density is projected onto the magnetic equator.

Previous studies of interhemispheric plasmaspheric ducts show the half-width ranges from 68 km to hundreds of km [Scarf and Chappell, 1973; Koons, 1989]. If the irregularity is the size of the wavelength of the wave or less, there is considerable leakage of the wave so that it is not efficiently guided [Strangeways, 1986; Streltsov et al., 2006]. On the other hand, if the irregularity is very large compared to a wavelength, the perpendicular gradient of N_e is small and the guidance properties of the duct are reduced. In this dissertation,

for the chorus waves to be efficiently guided by a duct, the lower limit of the half-width has been assumed to be ~ 5 wavelengths, while the upper limit may be as large as ~ 45 wavelengths.

An irregularity that satisfies both of these requirements is the enhancement duct denoted by Duct E in Figure 3.6. The half-width of Duct E, shown by the horizontal red line, is ~ 230 km and the relative change in electron density, shown by the vertical red line, is $\Delta N_e/N_e \sim 50\%$. While there are many small plasma irregularities within Duct E, these are too small to efficiently guide chorus waves and cannot be classified as ducts, as their half-widths are less than a wavelength.

3.5 Summary

In order to test the theory that banded chorus emissions are excited within whistler-mode ducts, N_e needs to be characterized with a spatial resolution of ~ 25 km or less to accurately identify ducts. Such measurements have not been available until the present study. Measurements of f_{pe} from EFW and WHISPER, instruments onboard the Cluster spacecraft, are used to determine N_e with the highest resolution and accuracy to date. With these measurements, N_e is determined with a spatial resolution of 17 km, a time resolution of 0.2 seconds, and an accuracy within 1%. Irregularities observed in the electron density profile are classified as ducts if they satisfy two requirements: 1) the half-width must be between ~ 5 and ~ 45 wavelengths, and 2) $\Delta N_e/N_e \geq 10\%$. In the following chapter, the electron densities determined through this process are used to analyze the relationship between ducts and banded chorus.

Chapter 4

Banded Chorus and Ducts

Using instruments onboard the Cluster spacecraft, the electron density is determined with the highest spatial resolution to date in order to accurately identify whistler-mode ducts. The purpose of this chapter is to investigate whether banded chorus emissions can be guided by, and generated within, whistler-mode ducts, through analysis of the relationship between chorus waves with measured wave normal angles and ducts near the magnetic equator. For all of the Cluster passes in this study, the wave normal information is only available for LB chorus emissions due to the upper frequency limit of the STAFF instrument of 4 kHz. Data from the Cluster spacecraft is used to test the theory that LB chorus waves can be guided by enhancement ducts for $\theta < \theta_G$ and depletion ducts for $\theta \gtrsim \theta_G$.

Two cases of banded chorus and ducts are examined: 1) October 31, 2003 and 2) January 20, 2004. The first case focuses on the relationship between wave normal angles and an enhancement duct, while the second case focuses on depletion ducts. Both cases show that the banded chorus emissions are generated within ducts and likely to be guided within these ducts. Following the two cases, statistics for over 24 hours of data for 19 orbits containing observations of chorus and ducts are analyzed to show that the majority of LB chorus waves can be guided by whistler-mode ducts.

Part of the work presented in this chapter has been published in *Geophysical Research Letters* as [Haque et al. \[2011\]](#).

4.1 Case I: October 31, 2003

Figure 4.1 shows the relationship between banded chorus, electron density, and wave normal angles for Cluster 3 on October 31, 2003 during 23:01-23:08 UT. The electric field frequency-time spectrogram showing banded chorus emissions in Figure 4.1a uses WBD data. The WBD instrument cycles every 52 seconds, recording data from the electric antenna for 42 seconds and data from the magnetic antenna for 10 seconds. The data from the electric antenna have been dilated to fill the 10 second data gap during which the magnetic antenna is recorded. The white line in the spectrogram represents $f_{ce}/2$, above which UB chorus is observed and below which LB chorus is observed. Figure 4.1b displays the electron density for the same time period, where an irregularity that satisfies both ducting requirements is seen. This enhancement duct is the same as Duct E in Figure 3.6. The half-width of this duct is ~ 230 km and the relative change in electron density is $\Delta N_e/N_e \sim 50\%$. While there are many small plasma irregularities within this duct, they are too small to efficiently guide chorus and cannot be classified as ducts, as their half-widths are less than a wavelength. For example, a wave with $f \sim 3.6$ kHz has a wavelength calculated to be ~ 17 km for $\theta \simeq 0^\circ$ or ~ 14 km for $\theta \simeq \theta_G$.

The Gendrin angle is given by

$$\theta_G = \cos^{-1} \left(\frac{\sqrt{\frac{(\mu_G^2 - P)(\mu_G^2 S - RL)}{(S - P)\mu_G^2 + (PS - RL)}}}{\mu_G} \right) \quad (4.1)$$

[Gendrin, 1960, 1961], where μ_G is the value of the refractive index at θ_G . The quantity μ_G^2 is expressed as

$$\mu_G^2 = \sqrt{\frac{PRL}{S} \left(1 + \frac{P^2 S^2 - R^2 L^2}{PRL(S - P)} \right) + \left[\frac{PS - RL}{S - P} \right]^2} - \frac{PS - RL}{S - P}, \quad (4.2)$$

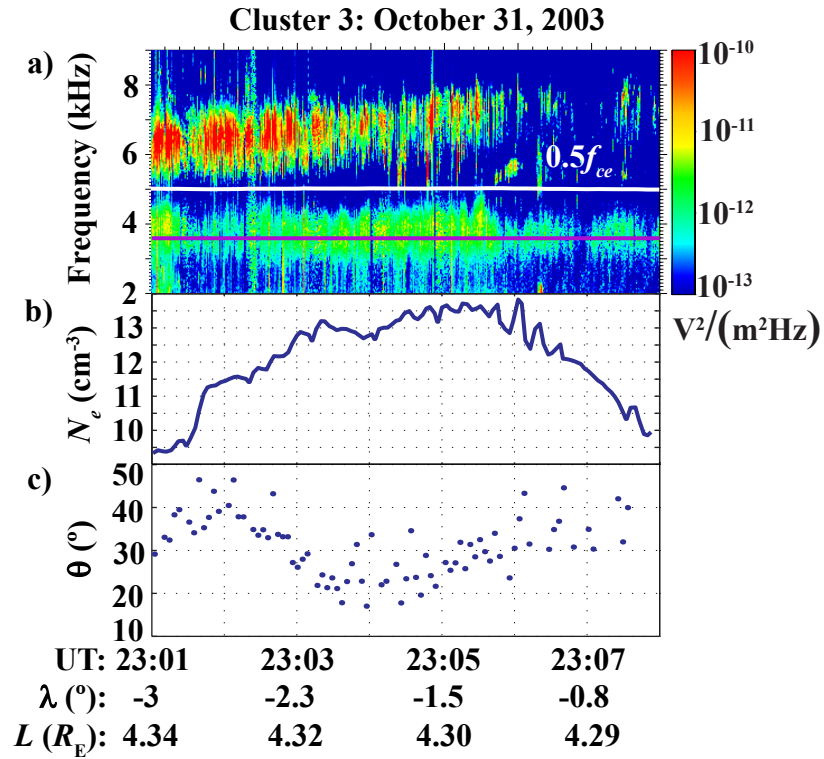


Figure 4.1: Measurements for Cluster 3 on October 31, 2003 during 23:01-23:08 UT. (a) E field spectrogram showing a pass with banded chorus. The white line indicates $f_{ce}/2$ and the purple line indicates the center frequency of the LB chorus. (b) Electron density and (c) wave normal angles for same time period. Ephemeris data for Cluster 3 is given on the bottom.

where S , P , R , and L are the parameters from Equations 2.8, 2.10, 2.11, and 2.12, respectively. A useful approximation of the Gendrin angle for whistler-mode waves is

$$\theta_G = \cos^{-1} \left(\frac{2f}{f_{ce}} \right) \quad (4.3)$$

[[Inan and Bell, 1977](#)].

The wave normal angles for chorus elements are calculated using the singular value decomposition (SVD) method [[Santolík et al., 2003](#)] on measurements from the STAFF instrument. The wave normal angles for the center frequency of the LB chorus, indicated by the purple line in Figure 4.1a, are shown in Figure 4.1c. The wave normal angles near the center of the duct have relatively small wave normal angles in the approximate range of 20° - 30° , while the wave normal angles near the edges of the ducts have values above 30° . The Gendrin angle, calculated using Equation 4.3, has a value of 48.6° . As $\theta < \theta_G$, the LB chorus waves can be guided by the enhancement duct. The chorus emissions are generated within this enhancement duct as well, as they are in the source region of chorus right near the magnetic equator and are generated at the same L -shell as the duct.

4.2 Case II: January 20, 2004

Figure 4.2a shows an E field spectrogram for Cluster 2 on January 20, 2004 during 19:27-19:36 UT. Of primary interest are two sets of banded chorus: Set 1 occurring during 19:27:15-19:30:30 UT and Set 2 occurring during 19:31:15-19:34:30 UT. Set 2 is observed close to the magnetic equator and displays the classic form of banded chorus in the source region, with UB chorus located above $f_{ce}/2$, indicated by the white line, and LB chorus located below. It can be seen that the chorus intensity is much weaker near 19:31 UT and 19:34 UT. A discussion of this effect can be found in Chapter 6.

Set 1, located further from the magnetic equator, has somewhat different characteristics, with the center of the gap between the chorus bands located well below $f_{ce}/2$ and the center frequencies of UB and LB chorus decreasing as $|\lambda|$ increases. These characteristics suggest that the chorus elements in Set 1 were generated near the magnetic equator at higher L -shells and subsequently propagated down to Cluster 2. Thus Set 1 is not related to Set 2,

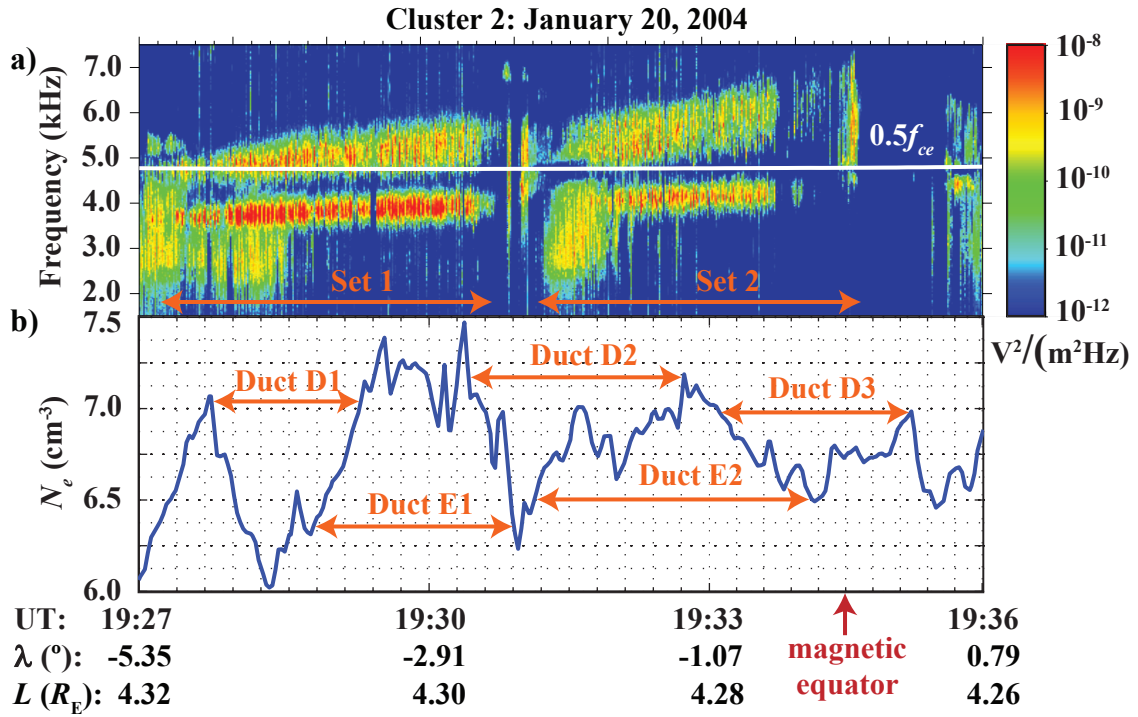


Figure 4.2: Measurements for Cluster 2 on January 20, 2004 during 19:27-19:36 UT. (a) E field spectrogram showing a pass with banded chorus. Two sets of banded chorus are denoted as Set 1, further from the magnetic equator, and Set 2, near the magnetic equator. The white line indicates $f_{ce}/2$. (b) Electron density with three depletion ducts and two enhancement ducts, denoted as Duct D1, D2, D3, E1, and E2, respectively. Ephemeris data for Cluster 2 is given on the bottom.

but demonstrates that numerous sources of banded chorus were present near the magnetic equatorial plane during this time, a common circumstance when banded chorus is observed.

The electron density is shown in Figure 4.2b for the same time interval as Figure 4.2a. During this interval, Cluster 2 moves ~ 3000 km parallel to, and ~ 400 km perpendicular to, the $L = 4.28$ magnetic field line. Though the L -shell range is not large, N_e still has a number of interesting features. Three depletion ducts and two enhancement ducts, with half-widths of 70 km or more, are denoted by Duct D1, D2, D3, E1, and E2, respectively. From Figure 4.2, it appears that Set 1 is generated within Ducts D1 and E1, while Set 2 is generated within Ducts D2, D3, and E2. However, not all chorus emissions located at the same L -shell as enhancement and depletion ducts are generated within those ducts. Chorus waves can only be generated within a particular duct if they are generated at the same L -shell as that duct.

Since the chorus elements of Set 1 are located further from the magnetic equator, which is the source region of chorus, they may have been generated at a different L -shell than Ducts D1 and E1. Ray tracing, following a method similar to [Lauben et al. \[2002\]](#), is performed on a falling LB chorus element at the beginning of Set 1 to determine the source region location of Set 1, shown in Figure 4.3. In this method, a ray is first traced backwards from the Cluster 2 spacecraft towards the magnetic equator. It is not necessary for the reverse ray paths to be terminated exactly at the magnetic equator, since chorus emissions are usually generated near the point of minimum inhomogeneity in the magnetic field, which may be slightly displaced from the magnetic equator, depending on geomagnetic disturbances [[Tsurutani and Smith, 1977](#)]. The ray is then traced from the proposed source location back towards the observation location. This process is repeated iteratively until the source location, from which the launched ray reaches the exact observation location, is determined.

The LB chorus element of Set 1 was observed by the Cluster 2 spacecraft at $L = 4.31$ and $\lambda = -4.60^\circ$ with $\theta \sim 70^\circ$. The source location of the element was found to be $L = 4.51$ and $\lambda = -0.46^\circ$, with $\theta = 56.2^\circ$. Although Set 1 is observed simultaneously with Ducts D1 and E1, the chorus is not generated at the same L -shell as these ducts and therefore has not been guided by them. Since the electron density is unknown for the region near $L = 4.51$, no association between Set 1 and ducts can be made.

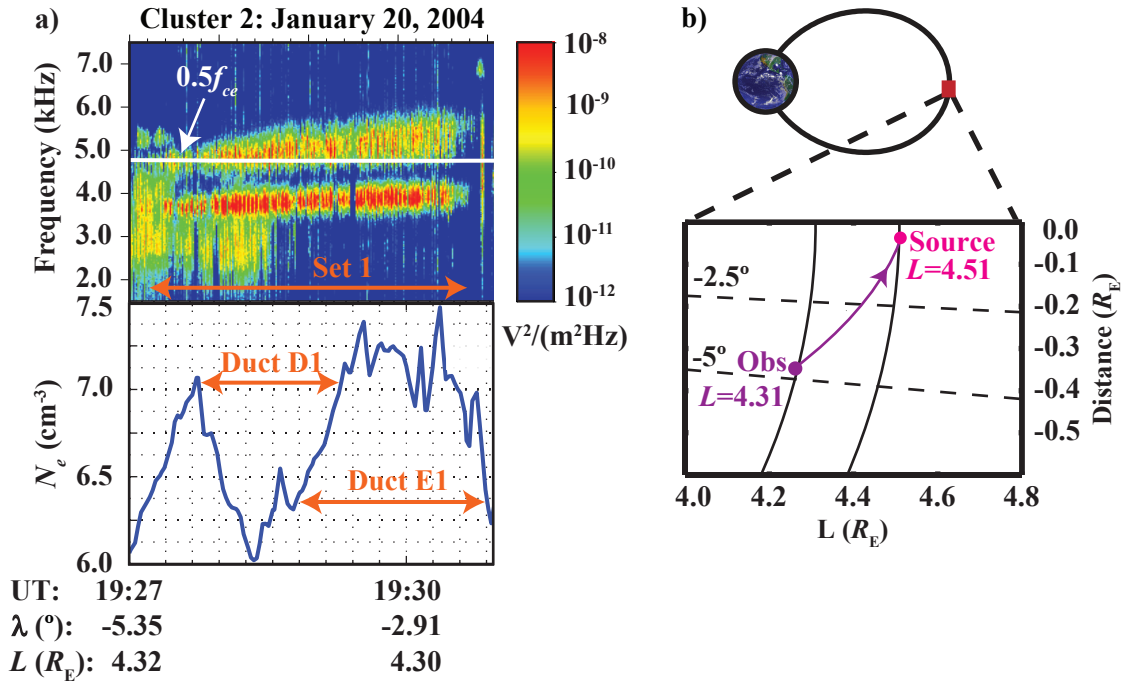


Figure 4.3: a) E field spectrogram and electron density profile for chorus elements from Set 1 for Cluster 2 on January 20, 2004. b) Inset of field lines located around $L = 4.4$ for North-South distance versus L -shell. The source location for a chorus element of Set 1 observed at $L = 4.31$ and $\lambda = -4.60^\circ$ with $\theta \sim 70^\circ$ is determined to be $L = 4.51$ and $\lambda = -0.46^\circ$ with $\theta = 56.2^\circ$ through ray tracing. The dashed lines represent magnetic latitude increments of 2.5° .

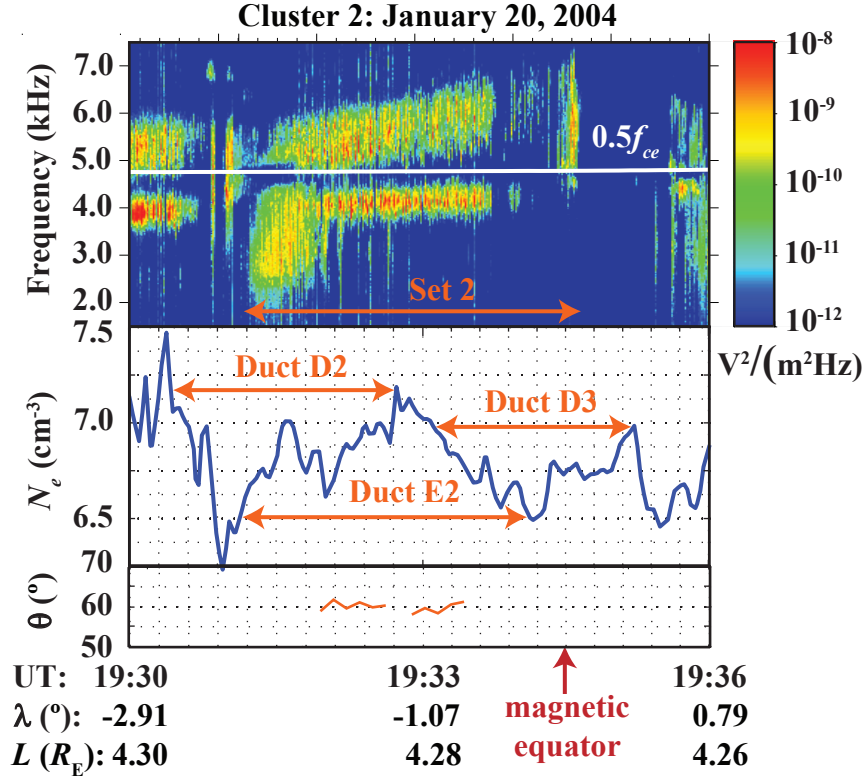


Figure 4.4: E field spectrogram, electron density profile, and wave normal angles for chorus elements from Set 2 for Cluster 2 on January 20, 2004. The wave normal angle for LB chorus, using the center frequency of 3.6 kHz, is between 55° and 60° .

As the chorus elements of Set 2 extend throughout the source region, $\lambda \simeq -2^\circ$ up to the magnetic equator for this case, they are generated at the same L -shell as Ducts D2, D3, and E2, as shown in Figure 4.4. The average wave normal angle for the LB chorus of Set 2, using the center frequency of 3.6 kHz, is calculated to be between 55° and 60° , while $\theta_G = 36^\circ$. Since $\theta > \theta_G$, the LB chorus waves can be guided only by the depletion ducts D2 and D3, meaning the chorus is likely to be generated within these ducts as well. To understand this concept, chorus generated within a duct can be compared to a marble within a bowl. If the marble is rolled from outside the bowl, it will likely not stay within the bowl, and leave the bowl on the other side. However, if the marble is rolled inside the bowl, it will likely remain trapped in the bowl. Similarly, chorus elements are likely to be trapped by the whistler-mode ducts in which they are generated.

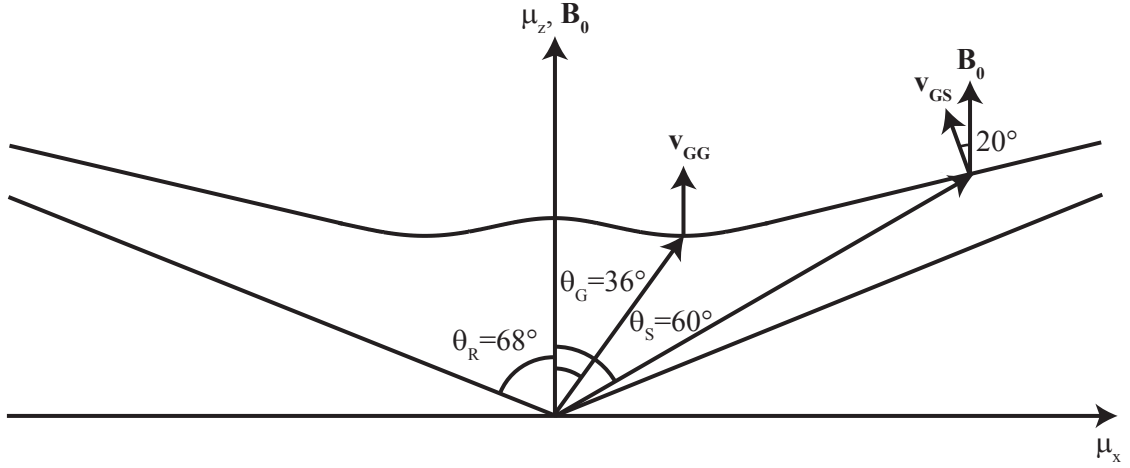


Figure 4.5: Refractive index surface for $f \sim 3.6$ kHz, $f_{ce} \sim 9.6$ kHz, and $f_{pe} \sim 22$ kHz. The vertical axis shows the direction of \mathbf{B}_0 . The Gendrin angle, its associated group velocity, and the resonance cone angle are shown as θ_G , \mathbf{v}_{GG} , θ_R , respectively. $\theta_S \sim 60^\circ$ is the average wave normal angle of the LB chorus of Set 2 in the source region. The angle between the associated group velocity, \mathbf{v}_{GS} , and \mathbf{B}_0 is $\sim 20^\circ$.

4.2.1 Lower Band Chorus Excitation

Using new high resolution N_e observations, we have examined the banded chorus pass from January 20, 2004 and found that the LB chorus is excited within whistler-mode depletion ducts. Since the LB chorus waves have $\theta \gtrsim \theta_G$, they can be guided only by depletion ducts. This guidance may be a necessary factor in the generation of banded chorus. The average wave normal angle for the LB chorus of Set 2 in the source region is $\theta_S \sim 60^\circ$.

For $f \sim 3.6$ kHz and $f_{ce} \sim 9.6$ kHz, θ_S has a value between θ_G and θ_R , the resonance cone angle, which have values of 36° and 68° , respectively. These values can be seen on the refractive index surface in Figure 4.5, calculated for these parameters as well as for $f_{pe} \sim 22$ kHz. The resonance cone angle, θ_R , is the angle at which the refractive index becomes infinite, meaning no propagation is possible for $\theta > \theta_R$, and is expressed as

$$\theta_R = \cos^{-1} \left(\sqrt{\left(\frac{f}{f_{pe}}\right)^2 + \left(\frac{f}{f_{ce}}\right)^2 \left[1 - \left(\frac{f}{f_{pe}}\right)^2\right]} \right) \quad (4.4)$$

[Gurnett and Bhattacharjee, 2005].

Using the values for f , f_{ce} , and f_{pe} , the direction of the group velocity vector, \mathbf{v}_{GS} , of the chorus waves can be calculated. The angle between \mathbf{B}_0 and \mathbf{v}_{GS} is $\sim 20^\circ$, with \mathbf{v}_{GS} pointing towards the Earth, shown in Figure 4.5. Since the tangent of 20° is $\sim 1/3$, for every 150 km the chorus waves propagate along \mathbf{B}_0 , they will also propagate 50 km across L towards the Earth. If the transverse scale of the source region for Set 2 is ~ 100 km [Santolík and Gurnett, 2003], which may be the characteristic duct scale, then Cluster 2 can only detect chorus waves generated within 150 km of the spacecraft position, shown in Figure 4.6.

However, chorus was detected within the entire green outlined region, implying that chorus is generated everywhere along the $L = 4.28$ field line from $\lambda = -1.7^\circ$ to $\lambda = -0.4^\circ$, a distance of ~ 500 km. This result is important because LB chorus generally has small wave normal angles [Santolík et al., 2009; Chum et al., 2009], making it difficult to determine if the chorus is generated within a small region near the magnetic equator and then propagates along \mathbf{B}_0 to the spacecraft, or if it is generated uniformly over an extended region. Our result suggests that uniform excitation of LB chorus over an extended region may be common. Since chorus wave normal angle information is only available for $f \leq 4$ kHz, the wave normal angles of the UB chorus in Figure 4.4 are not known. However, the UB chorus of Set 2 is clearly generated within the depletion ducts D2 and D3 shown in the source region of Figure 4.4, and can in principle be guided in these ducts. It is possible both UB and LB chorus may be guided in the same depletion duct.

4.3 Lower Band Chorus Statistics

The cases from October 31, 2003 and January 20, 2004 are representative of a larger data set used to assess whether LB chorus can be guided by ducts by analyzing the relationship between whistler-mode ducts and chorus waves with measured wave normal angles. The data set consists of observations of chorus emissions from 19 Cluster orbits, with 51 different passes spread across the four Cluster spacecraft. These orbits are from the years 2003, 2004, and 2006. The trajectory of Cluster for these passes is shown in a meridional plane projection in Figure 4.7a. The banded chorus passes were chosen to include the source

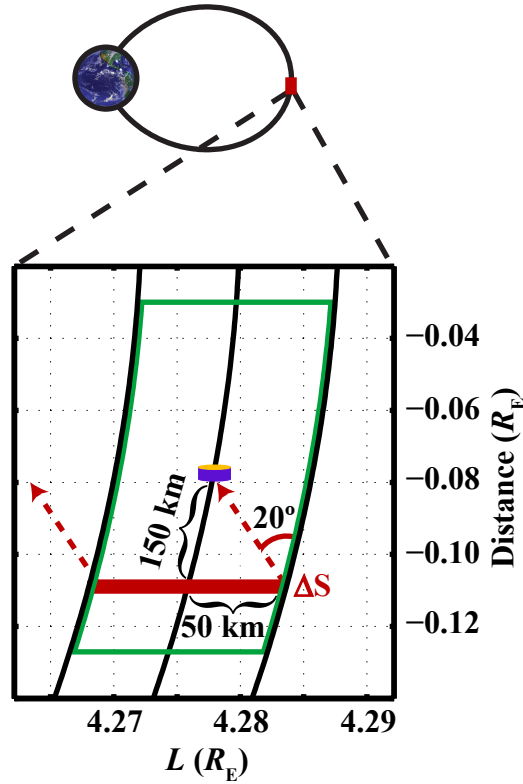


Figure 4.6: Inset of field lines located around $L = 4.28$ for North-South distance versus L -shell showing LB chorus propagation within a magnetic meridian. Assume a LB chorus element is generated in a region with a scale of 100 km across \mathbf{B}_0 and extending a small distance ΔS along \mathbf{B}_0 . Because the element's group velocity is directed 20° below the direction of \mathbf{B}_0 , the element propagates toward smaller L -shell values as shown by the dashed lines. After propagating 150 km parallel to \mathbf{B}_0 , the element can no longer be observed on the magnetic field line which originally bisected the source region.

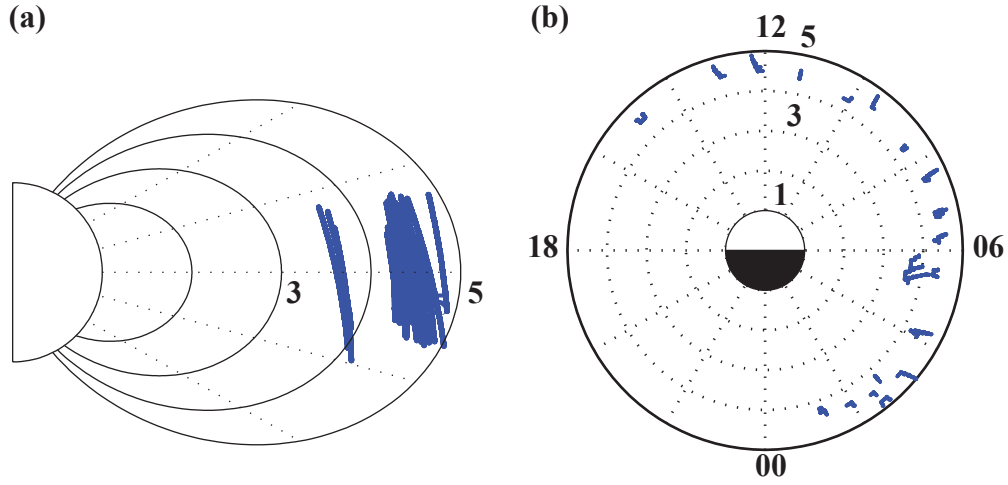


Figure 4.7: a) Trajectory of the Cluster spacecraft in a meridional plane projection for 19 orbits containing banded chorus emissions. The dashed lines represent magnetic latitude increments of 15° , while the solid lines represent dipole L -shell increments of $1R_E$. b) Distribution of MLT and L -shells. Each concentric circle represents an increase in L -shell by $1R_E$, while each sector represents an increment in MLT by 2 hours.

region, roughly defined for this study as magnetic latitudes within 3° of the magnetic equator. As there are data from multiple spacecraft for each orbit, the trajectories appear to be clustered together. The spacecraft sample L -shells in the range 3.6 to 5.0 and MLT in the range 1.3 to 15.0 hours, seen in Figure 4.7b.

The passes are also chosen such that the K_p index at the time of the 51 spacecraft passes was less than 5, indicating low to moderate storm-level geomagnetic activity so that the location of the magnetic equator could be reasonably determined [Santolík *et al.*, 2009]. The K_p index [Bartels *et al.*, 1939] indicates the level of geomagnetic disturbances, caused by the solar wind, by giving the mean value of the disturbance levels for the two horizontal magnetic field components as observed at 13 worldwide subauroral magnetic observatories. K_p is given for a three hour range on a quasi-logarithmic scale divided into discrete intervals of $1/3$. There are 28 such intervals taking the form 0, 0+, 1−, ..., 8+, 9−, 9.

Using the ducting requirements for efficient guidance, 57% of the irregularities that qualified as ducts are classified as enhancement ducts, while the other 43% are classified

as depletion ducts. However, not all chorus emissions located at the same L -shell as enhancement and depletion ducts are generated within those ducts. For instance, in the case of January 20, 2004, only the LB chorus of Set 2, located close to the magnetic equator, is generated within the ducts located at the same L -shell, while the LB chorus of Set 1 is not. For the chorus emissions generated within ducts at the same L -shell, the wave normal angle information is important to determine whether these emissions can be guided by these ducts.

The LB chorus emissions for this data set were found to be generated within ducts located at the same L -shell for magnetic latitudes within approximately 3° of the magnetic equator. As the wave normal angle requirement for guiding for LB chorus is different depending on whether the chorus is generated within an enhancement or depletion duct, these two cases are examined separately. Using over 24 hours of data from the Cluster spacecraft, 6,583 wave normal angles are analyzed for LB chorus generated within enhancement ducts and 5,395 wave normal angles are analyzed for LB chorus generated within depletion ducts, with an average of 31.8 wave normal angles per duct. For each set of chorus, the wave normal angles are analyzed for the center frequency of the band. However, if the center frequency is above 4 kHz, the upper frequency limit of the STAFF instrument, the frequency used is the one within the highest frequency band of the STAFF instrument, between 3.17 and 4 kHz. Though the polar wave normal angle can be determined for a range of 0° to 180° , it is normalized between 0° and 90° as the acute angle with respect to \mathbf{B}_0 , in order to be consistent with previous studies. With regards to the wave vector, 47.4% are directed away from the Earth, while the remaining 52.6% are directed towards the Earth.

The probability of occurrence for wave normal angles, divided into 10° intervals, for LB chorus generated within depletion ducts is shown in Figure 4.8a. The majority of wave normal angles have values between 30° – 60° . The probability of occurrence of wave normal angles in the ranges 30° – 40° , 40° – 50° , and 50° – 60° is 23.2%, 28.8%, and 20.4%, respectively. There is also an 11.1% probability of wave normal angles having values in the range 60° – 70° . There is less than 8% probability of occurrence of wave normal angles occurring in the other intervals. For our data set, the range of values for the Gendrin angle for depletion ducts is $26.8^\circ \leq \theta_G \leq 64.8^\circ$.

The probability of occurrence for the difference between the wave normal angle and the

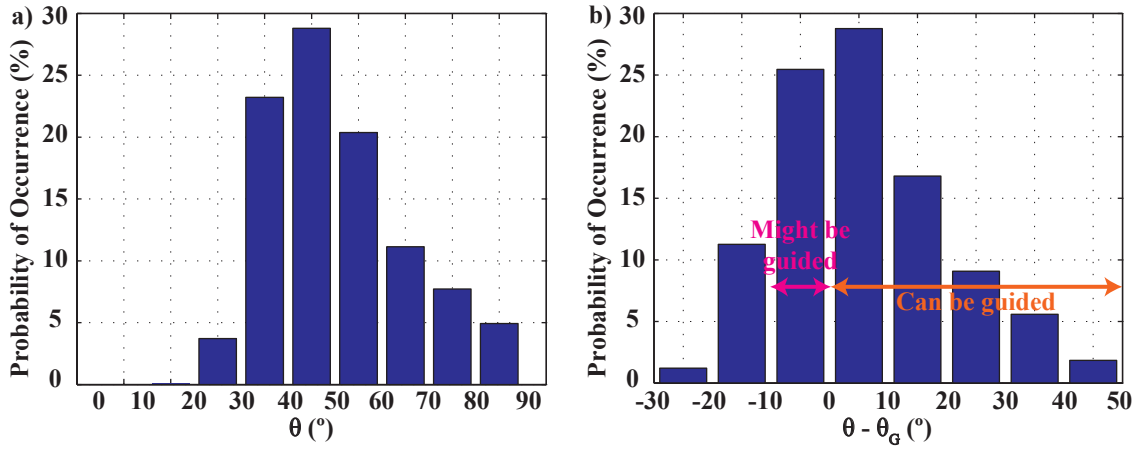


Figure 4.8: a) Probability of occurrence of wave normal angles, divided into 10° intervals, for LB chorus generated within depletion ducts over all orbits. b) Probability of occurrence of the difference between the wave normal angle and the Gendrin angle. Chorus can be guided for $\theta \geq \theta_G$ with a probability of $\sim 61\%$ and may be guided for $\theta - \theta_G$ in the range of -10° to 0° with a probability of $\sim 25\%$.

Gendrin angle, divided into 10° intervals, for LB chorus generated within depletion ducts is shown in Figure 4.8b. The quantity $\theta - \theta_G$ has values in the range -30° to -10° , for which the chorus waves cannot be guided, with a probability of occurrence of $\sim 12\%$. There is a $\sim 25\%$ probability of occurrence that $\theta - \theta_G$ has values in the range -10° to 0° , for which chorus waves might be able to be guided. For $\theta > \theta_G$, the probability of occurrence is $\sim 29\%$, $\sim 17\%$, and $\sim 9\%$ in the intervals $0^\circ - 10^\circ$, $10^\circ - 20^\circ$, and $20^\circ - 30^\circ$, respectively. There is less than 6% probability of occurrence in the range $30^\circ - 50^\circ$. In total, $\sim 61\%$ of the wave normal angles have values above the Gendrin angle, while $\sim 25\%$ have values near the Gendrin angle, indicating that the majority of UB chorus can be guided by depletion ducts.

The probability of occurrence for wave normal angles, divided into 10° intervals, for LB chorus generated within enhancement ducts is shown in Figure 4.9a. The majority of wave normal angles have values between $20^\circ - 40^\circ$. 49.6% of the wave normal angles occur in the range $30^\circ - 40^\circ$, while 28.0% of the wave normal angles occur in the range $20^\circ - 30^\circ$. In addition, 10.2% of the wave normal angles have values in the range $40^\circ - 50^\circ$. The wave normal angles have less than 3% probability of occurrence in the other intervals. For our

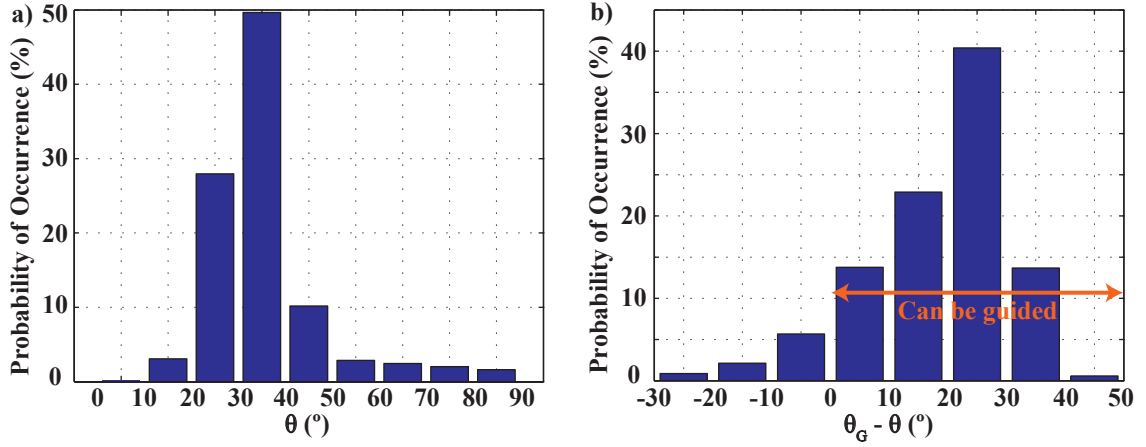


Figure 4.9: a) Probability of occurrence of wave normal angles, divided into 10° intervals, for LB chorus generated within enhancement ducts over all orbits. b) Probability of occurrence of the difference between the Gendrin angle and the wave normal angle. Chorus can be guided for $\theta < \theta_G$ with a probability of $\sim 91\%$.

data set, the range of values for the Gendrin angle for enhancement ducts is $41.5^\circ \leq \theta_G \leq 65.3^\circ$.

The probability of occurrence for the difference between the Gendrin angle and the wave normal angle, divided into 10° intervals, for LB chorus generated within enhancement ducts is shown in Figure 4.9. $\theta_G - \theta$ has values in the range $20^\circ - 30^\circ$ and $10^\circ - 20^\circ$ with a probability of occurrence of $\sim 40\%$ and $\sim 23\%$, respectively. The probability of occurrence is $\sim 14\%$ in both the ranges $0^\circ - 10^\circ$ and $30^\circ - 40^\circ$. In all other intervals, the probability of occurrence is less than 6%. In total, $\sim 91\%$ of the wave normal angles have values below the Gendrin angle, indicating that LB chorus can be guided by enhancement ducts.

The correlation between ducts and wave amplitude of chorus emissions has been recently studied by *Li et al.* [2011a,b] using data from the Time History of Events and Macroscale Interactions during Substorms (THEMIS) spacecraft [*Sibeck and Angelopoulos, 2008; Burch and Angelopoulos, 2009*], shown in Figure 4.10. THEMIS consists of five probes launched on February 17, 2007 in near-equatorial orbits with apogees above $10R_E$ and perigees below $2R_E$. In this study, it was found that the chorus wave amplitude peaked significantly within both enhancements and depletions of electron density. Though the chorus emissions in the *Li et al.* [2011a,b] study were observed at higher L -shell values

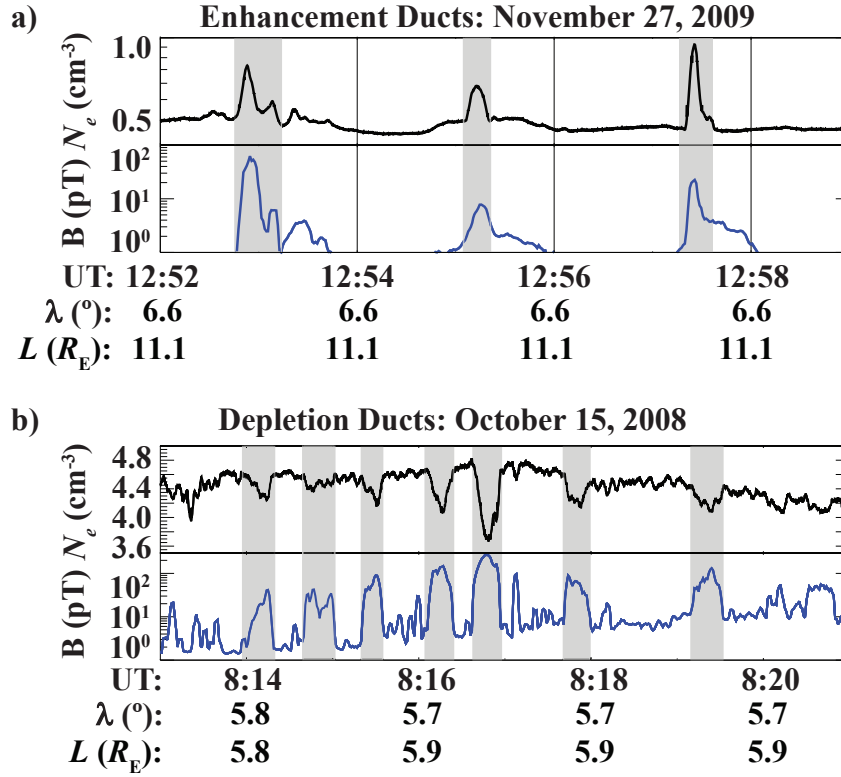


Figure 4.10: Measurements for THEMIS E on a) November 27, 2009 from 12:52-12:59 UT and b) October 15, 2008 from 08:13-08:21 UT. Total electron density is inferred from the spacecraft potential. The chorus wave amplitude is integrated over a) 0.25-0.35 f_{ce} and b) 0.05-0.5 f_{ce} . The chorus wave amplitude peaks significantly within both enhancements and depletions of electron density. Figure adapted from [Li et al. \[2011b, Figs. 1 and 4\]](#).

of 5–12, the findings are still significant as they seem to support the idea that chorus may be generated within whistler mode ducts.

4.4 Summary

The relationship between banded chorus emissions and whistler-mode ducts is analyzed for two cases, as well as a larger data set consisting of 51 different passes from the Cluster spacecraft. The half-width of these ducts is comparable to the transverse scale, ~ 100 km, of the chorus source region [[Santolík and Gurnett, 2003](#)]. For the case on January 20, 2004, making use of the fact that the group velocity of the LB chorus waves has a significant

cross- L component, we found that the source region extends over 500 km near the magnetic equator.

The cases from the entire data set have shown that LB chorus can be generated within enhancement and depletion ducts. From the wave normal angle distributions, it can be concluded that LB chorus can also be guided by ducts, as $\theta \gtrsim \theta_G$ with a probability of $\sim 87\%$ for depletion ducts and $\theta < \theta_G$ with a probability of $\sim 91\%$ for enhancement ducts. The correlations of chorus wave amplitude with enhancement and depletion ducts further support these conclusions. The conclusions from this study suggest that the source region of banded chorus is limited to a large, but finite number of locations within the magnetosphere. Therefore, banded chorus would not be excited continuously near the magnetic equatorial plane over some large range of L outside the plasmapause, but rather would only be predominantly excited within whistler-mode ducts.

Chapter 5

Wave Normal Angle Distribution

Using data from the Polar spacecraft, wave normal angles have been analyzed for 13 orbits containing UB chorus emissions and 15 orbits containing LB chorus emissions. The purpose of this chapter is to characterize the distribution of the polar wave normal angle, θ , for chorus emissions as a function of magnetic latitude, λ . Understanding wave normal angles is an important step in evaluating resonant wave-particle interactions. For UB chorus, wave normal angles tend to remain at or rise towards the resonance cone angle for low and mid-latitudes, but move away from the resonance cone angle at higher latitudes. For LB chorus, wave normal angles with values $\theta < 20^\circ$ have the highest probability of occurrence in the latitude range of $10^\circ - 50^\circ$. Just off the equator, $10^\circ \leq \lambda < 25^\circ$, there exists a secondary occurrence peak in the range of $50^\circ \leq \theta < 70^\circ$. The probability of observing these higher wave normal angles decreases with increasing latitude. The time averaged Poynting flux, S , is much larger for LB chorus waves, which have a mean value of $8.5 \times 10^{-8} \text{ W/m}^2$, than for UB chorus waves, which have a mean value of $1.4 \times 10^{-9} \text{ W/m}^2$. S is fairly evenly distributed about its median value, $3.1 \times 10^{-10} \text{ W/m}^2$, for all wave normal angles for UB chorus, but decreases as θ increases for LB chorus.

The work presented in this chapter has been published in *Journal of Geophysical Research* as [Haque et al. \[2010\]](#).

5.1 Chorus Wave Normal Angles

Chorus is believed to play a major role in the evolution of energetic particle distributions in the magnetosphere. Cyclotron resonant wave-particle interactions involving chorus can result in the precipitative loss of electrons over a wide range of energies. Chorus is believed to be a driver of low energy (< 1 keV) diffuse auroral precipitation [Inan *et al.*, 1992; Villalon and Burke, 1995; Ni *et al.*, 2008], medium energy (10s to 100 keV) microburst precipitation [Rosenberg *et al.*, 1971, 1981, 1990], and relativistic (> 1 MeV) microburst precipitation [Lorentzen *et al.*, 2001; Thorne *et al.*, 2005]. Interactions with chorus can also result in energy diffusion and thus contribute to the acceleration of electrons to MeV energies [Horne and Thorne, 1998; Horne *et al.*, 2005a,b; Shprits *et al.*, 2006; Summers *et al.*, 2007a,b]. Pitch angle scattering and energy diffusion can occur when the resonance condition, expressed in Equation 1.4, is satisfied. While both θ and ϕ are needed to predict how the wave will propagate in the magnetosphere from its current location, only θ is needed to evaluate the resonance condition, and is therefore the focus of this study.

While there have been several previous studies of chorus wave normal angles, many of them focused on the generation mechanism of chorus, and consequently were mostly limited to the equatorial plane. Past studies of wave normal angles for UB chorus emissions near the magnetic equator, $\lambda < 5^\circ$, show different results. From studying one pass of the GEOS 2 satellite, Hayakawa *et al.* [1984] concluded that the wave normal angles are near the resonance cone. However, Hospodarsky *et al.* [2001] found that the emissions propagate primarily parallel to the magnetic field from the analysis of one pass of the Cassini spacecraft. Lauben *et al.* [2002] also showed that UB chorus was emitted at $\theta \sim 0^\circ$ near the equator using properties of the wave measured by the Polar satellite and then doing multi-frequency ray tracing back to the source region. Outside the equatorial plane, Muto *et al.* [1987] analyzed two passes of the GEOS 1 satellite and concluded that θ is close to θ_R for $\lambda \sim 17^\circ$, but that θ is $15^\circ - 20^\circ$ less than θ_R for $\lambda \sim 26^\circ$.

Studies of LB chorus emissions in the equatorial plane, $\lambda < 6^\circ$, had some similarities. From three passes of the OGO 5 satellite, Goldstein and Tsurutani [1984] found that the majority of wave normal angles for LB chorus had values $\theta < 20^\circ$, as did Hayakawa *et al.* [1984] for the LB chorus rising emissions with small values of df/dt . However, Hayakawa

et al. [1984] found $\theta = 30^\circ - 45^\circ$ for LB chorus risers with increased values of df/dt . *Hospodarsky et al.* [2001] concluded that LB chorus emissions have $\theta \simeq 0^\circ$ in this latitude region. However, *Lauben et al.* [2002] deduced that LB chorus waves are emitted with wave normal angles close to the Gendrin angle. *Burton and Holzer* [1974] studied 18 passes of the OGO 5 satellite containing LB chorus over a much broader range of magnetic latitudes. They concluded that $\theta < 30^\circ$ for 80% of the wave normal angles occurring in $\lambda < 40^\circ$. However, in the higher latitude region ($\lambda = 40^\circ - 50^\circ$), the wave normal angles were more broadly distributed, extending to 85° .

Because of the difficulty in determining chorus wave normal angles, as measurements are required of all three magnetic field components and at least two electric field components, the previous studies were confined to a small region of the magnetosphere and limited in the number of wave normal angles analyzed. The data set in this study consists of a subset of 59 orbits of the Polar spacecraft containing banded chorus, as determined by *LeDocq et al.* [1998] through the examination of all available high-telemetry HFWR data (394 orbits from March 28, 1996 to September 16, 1997), after which the PWI instrument ceased to operate. For these orbits, the wave normal angles are determined from measurements of the three-component electric and magnetic fields, not only in the source region but for wherever chorus waves propagate. 1,765 wave normal angles for UB chorus emissions and 993 wave normal angles for LB chorus emissions over a broad range of magnetic latitudes, in both the equatorial and off-equatorial regions, L -shells, and magnetic local times are analyzed. The results of this study are important for studies of resonant interactions between chorus waves and electrons over a wide range of energies.

A sample plot of the data set for an orbit containing LB chorus from 19:52 to 20:03 UT and UB chorus from 19:57 to 20:10 UT on December 14, 1996 is shown in Figure 5.1. All of the measured and calculated parameters of Figure 5.1 have a log spaced frequency resolution ranging from 9.2 Hz to 1.2 kHz for 123 frequencies ranging from 0.2 to 25 kHz and a time resolution of 0.45 seconds. Each antenna only records 0.45 second snapshots of the waveform every 9.2 seconds. Therefore, the data in Figure 5.1 is not actually continuous but is the concatenation of each of the 0.45 second snapshots expanded over a 9.2 second interval.

Figures 5.1a and 5.1b represent measured quantities of the sum of the three magnetic

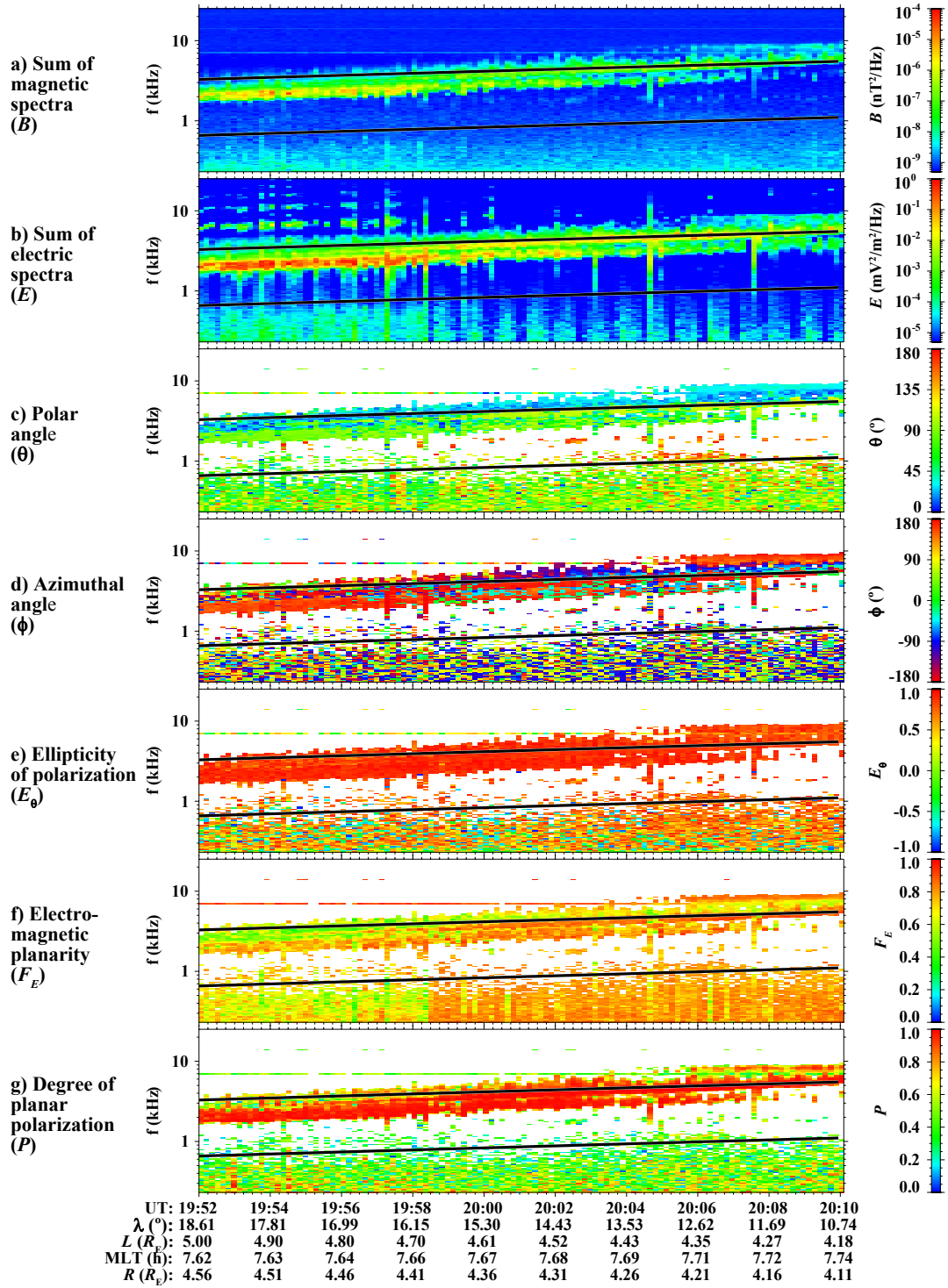


Figure 5.1: Sample plot of data for orbit containing LB chorus from 19:52 to 20:03 UT and UB chorus from 19:57 to 20:10 UT on December 14, 1996. The solid black lines in each panel represent 0.1 and 0.5 times the equatorial gyrofrequency.

auto-power spectra and the sum of the three electric auto-power spectra. The SVD technique is used on the electromagnetic spectral matrix to determine the polar wave normal angle, the azimuthal wave normal angle, and the electromagnetic planarity, F_E , which determines the planarity of the electromagnetic wave. SVD is also used on the magnetic spectral matrix to obtain the degree of planar polarization, P , and the ellipticity of polarization, E_θ . Values of P close to 1.0 mean that the magnetic field of the wave is coherent and that the ellipticity parameter is well defined. To ensure that E_θ is well defined, it was required that $P > 0.9$. In order for the waves to meet the right hand circular polarization condition for whistler-mode waves, it was required that $E_\theta > 0.8$. $F_E > 0.8$ was also required to ensure that the electromagnetic wave was close to a single plane wave and that the wave normal angles calculated are valid for whistler-mode waves.

5.2 Classification of Wave Normal Angles

For chorus emissions located off the magnetic equator, the wave frequency is more closely associated with the equatorial gyrofrequency, f_{ceq} , than with the local gyrofrequency [e.g., [Burtis and Helliwell, 1969](#)]. To distinguish between the upper and lower bands of chorus, we first estimate the equatorial gyrofrequency. The equatorial gyrofrequency was estimated by scaling the local gyrofrequency, calculated using the local magnetic field measured by the onboard magnetometer, using the current magnetic latitude and L -shell of the spacecraft and assuming a dipolar variation of the field strength along the field line. In all of the panels of Figure 5.1, the solid black lines represent 0.1 and 0.5 times the estimated equatorial gyrofrequency. However, since f_{ceq} was estimated based on a dipolar scaling, there are likely to be errors when operating at high latitudes and L -shells. The maximum error in f_{ceq} is estimated to be on the order of $\sim 15\text{--}20\%$, and therefore, the estimated f_{ceq} was used only as a starting guide to distinguish between the two bands. Visual inspection of the electric field for each individual orbit was used to separate the two bands along the line that best fit the typical gap seen between the two bands to ensure minimal overlap between the bands. The electric field was used to make the distinction because the strength of the electric field is typically on the order of at least two magnitudes larger than the strength of the magnetic field, making it easier to see the gap between the two bands visually. For

instance, in Figure 5.1a, though the upper solid black line representing $0.5f_{ceq}$ is used as a starting guide to distinguish between the upper and lower band chorus emissions, visual inspection of the electric field shows that the typical gap between the two bands actually occurs below this line. The line that best fit this typical gap was manually found for this and every other orbit used in this study. Using this method, it was determined that 24 orbits contained UB chorus emissions, while 35 orbits contained LB chorus emissions.

Due to its highly elliptical orbit, the Polar spacecraft crosses the magnetic equator in a region just inside the plasmopause at L -shells ranging from 2.5 to 4.5. For magnetic latitudes $\lambda < 30^\circ$, the spacecraft typically samples L -shells up to $L = 8$ [Gurnett et al., 1995]. Thus, in analyzing the wave normal angles calculated from Polar data, it is impossible to distinguish between latitudinal and L -shell effects. However, the equatorial plane has been shown to be the source region of the waves, and no current theories for wave generation are L -shell dependent. Thus, the propagation of the waves from the equatorial to the off-equatorial region is expected to have a much stronger effect on the wave normal angle distribution than variations with L -shell. Therefore, the variation of wave normal angle in this study will be characterized only in terms of magnetic latitude.

When the strength of the total electric field, E , is weak for the chorus emissions, there exists an immense amount of scatter and variation in the wave normal angles as a function of magnetic latitude. In order to reduce some of the scatter attributed to noisy measurements, a frequency dependent threshold level was determined. Thus, the orbits included in this study are those for which strong electric fields, corresponding to chorus emissions, were detected. For frequencies below 2 kHz, the threshold level is $E > 10^{-3} \text{ mV}^2/\text{m}^2/\text{Hz}$. For frequencies above 2 kHz, the threshold level is $E > 10^{-4.5} \text{ mV}^2/\text{m}^2/\text{Hz}$. After applying the frequency dependent threshold to all of the orbits, only 10 orbits containing UB chorus, 12 orbits containing LB chorus, and 3 orbits containing both upper and lower band chorus remained with sufficient data for wave normal analysis. For each of these orbits, the wave normal angles used for this study will be those that correspond to any frequency that satisfies the frequency dependent threshold and for which chorus was detected.

The following wave normal angle analysis will focus exclusively on the polar angle component of the wave normal angle, as the azimuthal angle plays no role in resonant wave-particle interactions, though it is important for determining the propagation of the

wave. Though the polar wave normal angle can be determined for a range of 0° to 180° , it will be normalized between 0° and 90° as the acute angle with respect to \mathbf{B}_0 in the direction of the Poynting vector, to be consistent with previous studies.

5.3 Upper Band Chorus Wave Normal Angles

For the 13 orbits containing UB chorus waves, two case studies will be shown, followed by statistics for all 13 orbits. The two case studies can be seen in Figure 5.2, with the orbit for the top panel occurring on December 14, 1996 and the orbit for the bottom panel occurring on July 31, 1997. The case study from December 14, 1996 took place from 19:06 to 20:24 UT near 7.5 MLT. A portion of the data for this orbit was shown in the sample plot in Figure 5.1, where it is clear that there are UB chorus emissions above $0.5f_{ceq}$. Figure 5.2a shows the wave normal angles as a function of magnetic latitude. For this case, the wave normal angles are small ($\theta < 20^\circ$) near the equator, but quickly rise to values close to the corresponding resonance cone angle, represented by the solid red line, as the satellite moves to higher latitudes. The solid red line is the best fit line for the resonance cone angles calculated using Equation 4.4 for each frequency of the chorus emission that satisfied the frequency dependent threshold. Figure 5.2b shows the trajectory of the Polar satellite in the meridional plane for this particular case study. The dashed lines in the meridional plane represent magnetic latitude increments of 15° . The solid lines represent dipole L -shell increments of $1R_E$. The spacecraft samples magnetic latitudes ranging from 3° to 29° and L -shells ranging from 3.7 to 6.8.

The second UB chorus case study from July 31, 1997 occurred from 16:01 to 16:21 UT near 4.6 MLT. The latitudinal dependence of the wave normal angles, shown in Figure 5.2c, illustrate that the wave normal angles remain relatively close to the resonance cone angle for the entire duration of the pass. The satellite samples $6.8^\circ \leq \lambda \leq 9.8^\circ$ and $3.6 \leq L \leq 3.8$.

These two case studies are representative of all of the UB chorus case studies in this study. The trajectory of the Polar spacecraft for the 13 orbits containing UB chorus emissions is shown in the meridional plane in Figure 5.3a. The spacecraft samples a broad range of magnetic latitudes, $3^\circ \leq \lambda \leq 35^\circ$, and L -shells, $3.2 \leq L \leq 7.7$. The distribution of magnetic local times and L -shell for the 13 orbits can be seen in Figure 5.3b. Each concentric

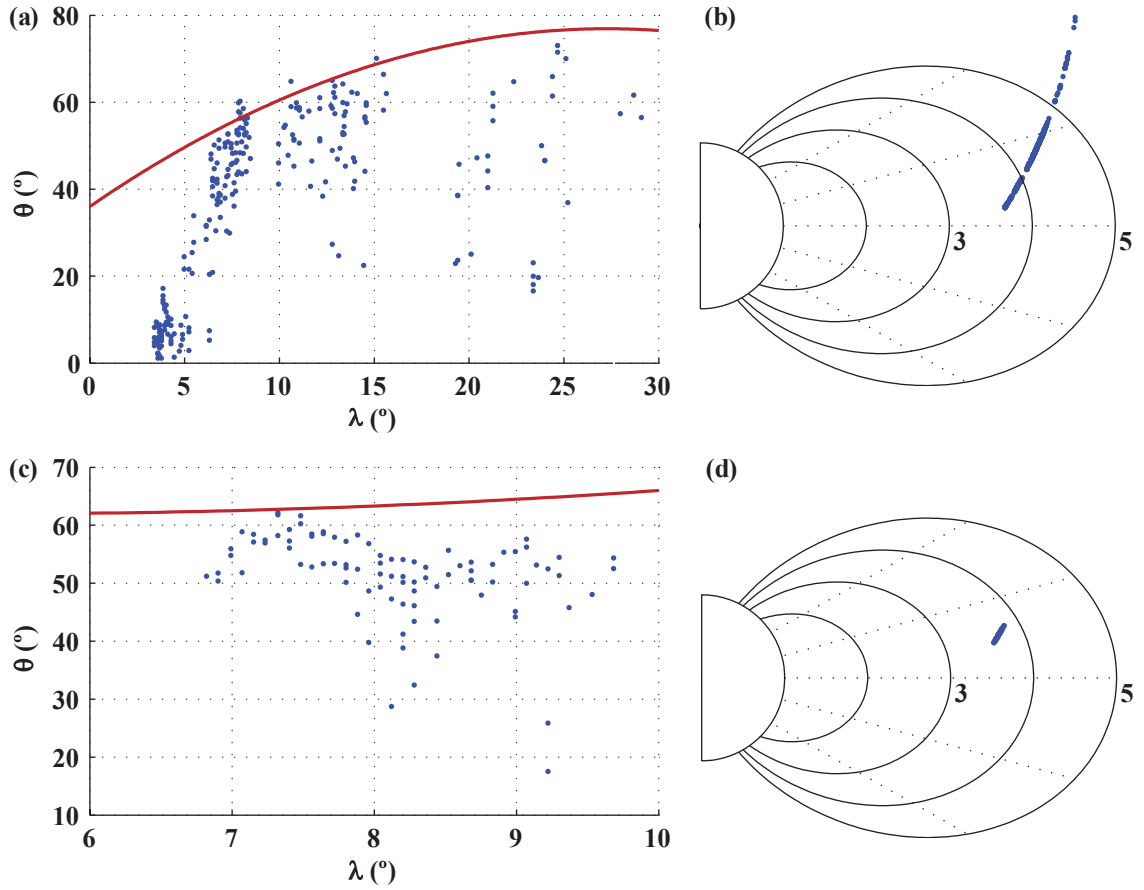


Figure 5.2: Wave normal angle, θ , versus magnetic latitude, λ , and the trajectory of the satellite in the meridional plane for two UB chorus case studies occurring on December 14, 1996 from 19:06 to 20:24 UT near 7.5 MLT, shown in (a) and (b), respectively, and on July 31, 1997 from 16:01 to 16:21 UT near 4.6 MLT, shown in (c) and (d), respectively. The solid red lines in parts (a) and (c) represent the resonance cone angle. The dashed lines in parts (b) and (d) represent magnetic latitude increments of 15° , while the solid lines represent L -shell increments of $1 R_E$.

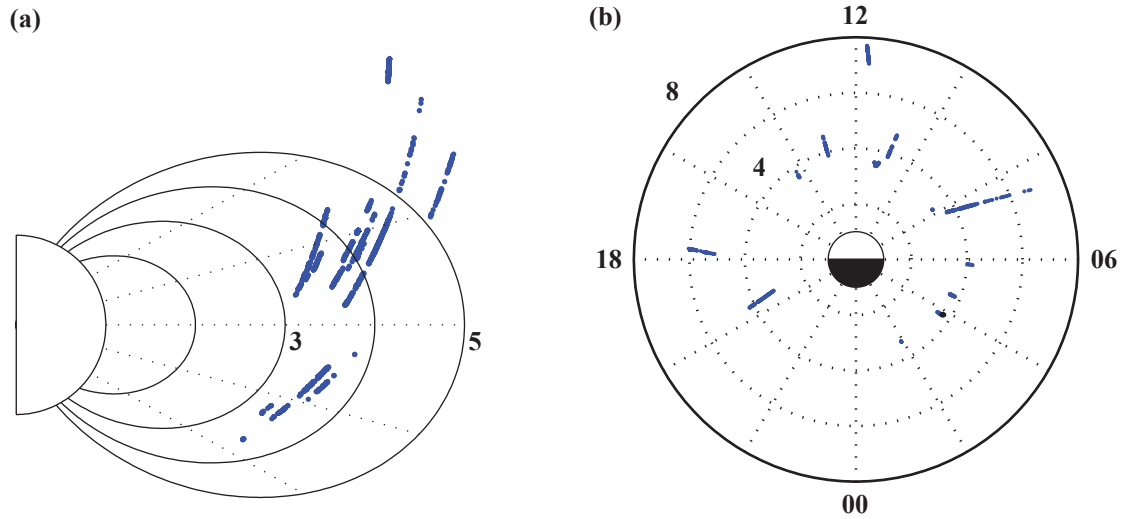


Figure 5.3: (a) Trajectory of the Polar spacecraft in the meridional plane for the 13 orbits containing UB chorus emissions. (b) Distribution of MLT and L -shells. Each concentric circle represents an increment in L -shell by $2R_E$, while each sector represents an increment in MLT by 2 hours.

circle represents an increment of 2 in L -shell, while each sector represents an increment in MLT by 2 hours. Because of the relatively sparse sampling in local time, we have not attempted to characterize differences in wave normal angle as a function of that parameter.

The overall distribution of wave normal angles over all magnetic latitudes for all UB chorus case studies is shown in Figure 5.4. The histogram is shown for wave normal angles divided into 10° intervals. The distribution is Gaussian-like, with the peak probability of occurrence taking place between $50^\circ \leq \theta < 60^\circ$. The rise in the probability of occurrence from lower wave normal angles to the peak is much less steep than the fall in the probability of occurrence from the peak to higher wave normal angles.

The probability of occurrence for different ranges of wave normal angles in the three magnetic latitude regions, $\lambda < 10^\circ$, $10^\circ \leq \lambda < 25^\circ$, and $25^\circ \leq \lambda < 40^\circ$, is illustrated in Figure 5.5. For each magnetic latitude region, the wave normal angles are divided into 10° intervals with their values indicated by the color scale. The probability of occurrence for the wave normal angles is normalized with respect to each magnetic latitude region in order to remove the bias of reduced sampling at higher magnetic latitudes by the Polar spacecraft.

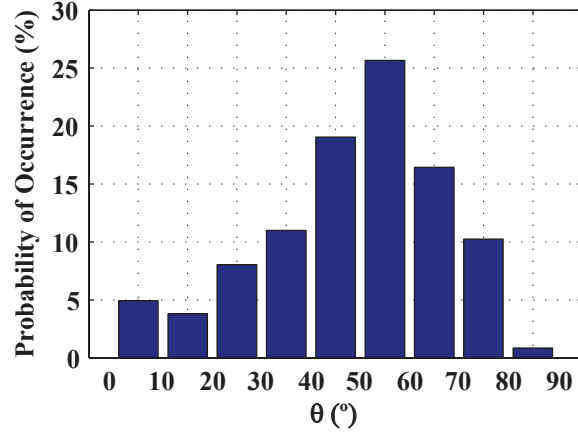


Figure 5.4: Probability of occurrence of wave normal angles over all magnetic latitudes for UB chorus case studies.

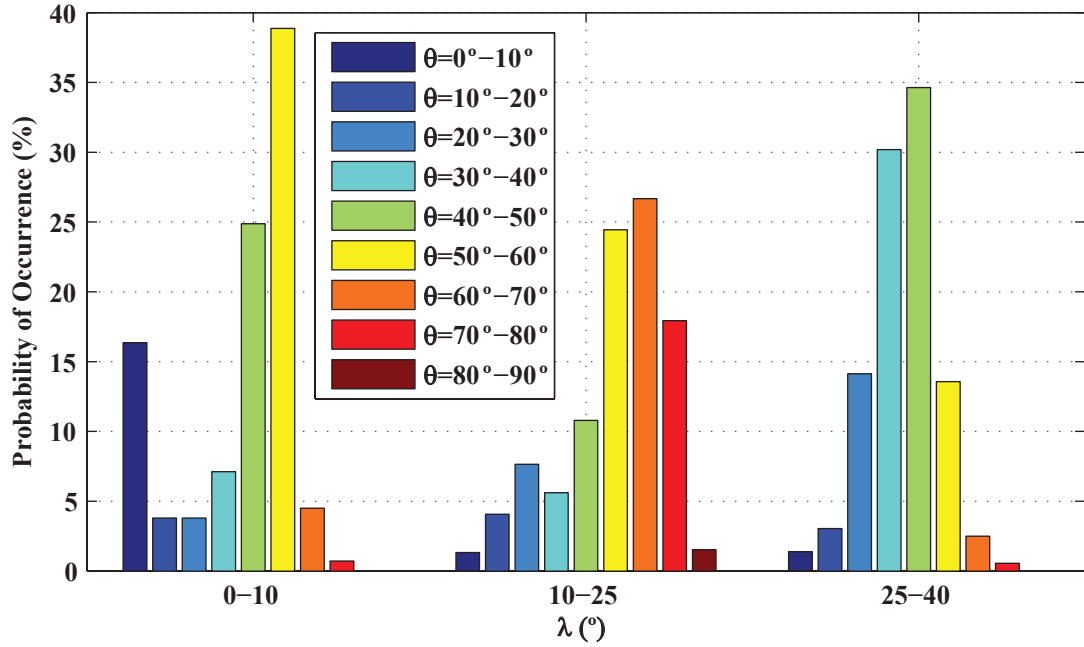


Figure 5.5: Probability of occurrence of wave normal angles, divided in 10° intervals, normalized with respect to each magnetic latitude region for UB chorus emissions. The value of the wave normal angle is indicated by the color scale.

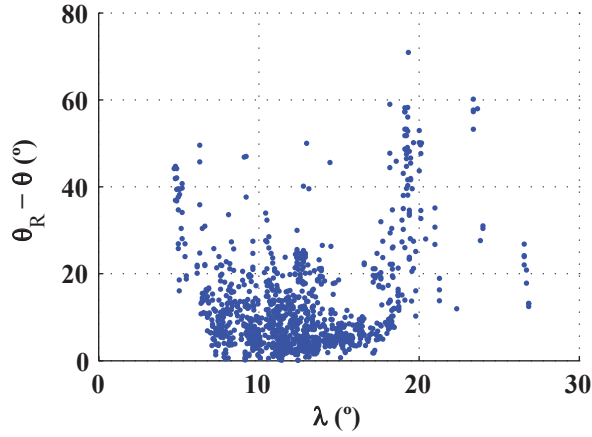


Figure 5.6: Difference between wave normal angle, θ , and the corresponding resonance cone angle, θ_R , with respect to magnetic latitude for UB chorus case studies.

As seen in Figure 5.4, the majority of wave normal angles for UB chorus occurs between 40° to 70° for all latitude ranges. However, Figure 5.5 demonstrates that there is a slight shift in peak probability of occurrence of the wave normal angles from higher wave normal angles ($50^\circ \leq \theta < 60^\circ$) at low latitudes ($\lambda < 10^\circ$) to lower wave normal angles ($40^\circ \leq \theta < 50^\circ$) at higher latitudes ($25^\circ \leq \lambda < 40^\circ$). This shift in peak can be seen with the help of Figure 5.6, which shows the difference between the wave normal angle and its corresponding resonance cone angle as a function of magnetic latitude. The resonance cone angle can only be calculated for those orbits for which the electron density can be extracted from the SFR on the Polar spacecraft. Therefore, the magnetic latitude range for Figure 5.6 is only $4^\circ \leq \lambda \leq 27^\circ$. In the mid-latitude region between $7^\circ \leq \lambda \leq 18^\circ$, the wave normal angle is very close to the resonance cone angle. However, at higher latitudes, it seems that the wave normal angle starts to move away from the resonance cone angle, though there is reduced sampling by the spacecraft at these latitudes.

In Figure 5.5, the other significantly high probability of occurrence takes place for wave normal angles in the range $\theta < 10^\circ$ for magnetic latitudes $\lambda < 10^\circ$. The case study from December 14, 1996, shown in the top panel of Figure 5.2, illustrates this result, as all of the wave normal angles in this region of high probability are from that orbit and one other orbit on October 31, 1996. The latter pass had very similar characteristics to that of the former, with small wave normal angles near the equator and larger wave normal angles at

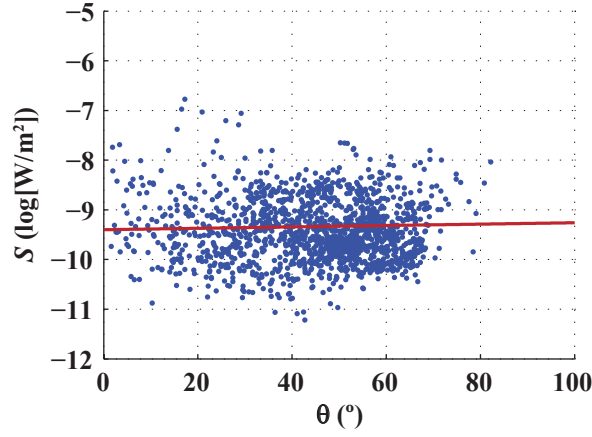


Figure 5.7: Time averaged Poynting flux, S , as a function of wave normal angle for UB chorus emissions. The solid red line represents the linear least squares fit to the data.

higher latitudes. This result is consistent with expectations from ray tracing in a smooth magnetosphere. For example, rays launched near the equator outside the plasmopause at a frequency of $0.6f_{ceq}$ and initial wave normal angle parallel to the magnetic field will quickly move toward the resonance cone angle as they propagate to higher magnetic latitudes. As seen in Figure 5.6, the observations closest to the equator show low wave normal angles (large difference between θ and θ_R) while observations at latitudes greater than $\sim 7^\circ$ show wave normal angles that are already approaching the resonance cone.

The time averaged Poynting flux, S , was calculated for each UB chorus case study and is plotted as a function of wave normal angle in Figure 5.7, with the solid red line representing the linear least squares fit to the data. It can be seen that the power ranges from 6.0×10^{-12} to $1.7 \times 10^{-7} \text{ W/m}^2$ for UB chorus emissions. Figure 5.7 also illustrates that the power is almost evenly distributed about its median value ($3.1 \times 10^{-10} \text{ W/m}^2$) with no clear dependence on the wave normal angle.

5.4 Lower Band Chorus Wave Normal Angles

For the 15 orbits containing LB chorus waves, two case studies will be shown, followed by overall statistics. The two case studies can be seen in Figure 5.8, with the orbit for the top panel occurring on February 28, 1997 and the orbit for the bottom panel occurring on

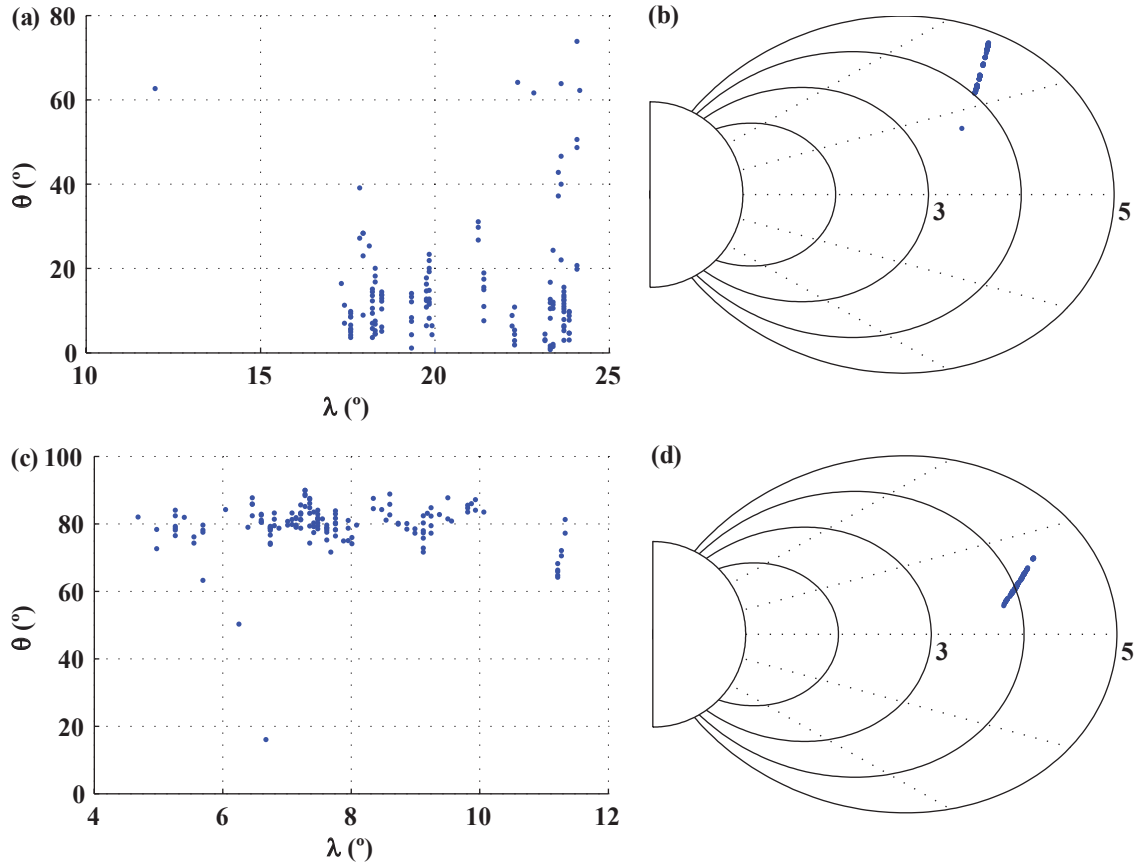


Figure 5.8: Wave normal angle versus magnetic latitude and the trajectory of the satellite in the meridional plane for two LB chorus case studies occurring on February 28, 1997 from 10:15 to 10:41 UT near 2.8 MLT, shown in (a) and (b), respectively, and on September 14, 1997 from 15:10 to 15:30 UT near 1.8 MLT, shown in (c) and (d), respectively.

September 14, 1997. The case study from February 28, 1997 took place from 10:15 to 10:41 UT near 2.8 MLT. The latitudinal dependence of the wave normal angle in Figure 5.8a shows the vast amount of scatter in the wave normal angles with respect to magnetic latitude typical of nearly all the orbits containing LB chorus. The Polar spacecraft samples magnetic latitudes ranging from 10° to 25° and L -shells ranging from 3.5 to 5.0, as seen in its trajectory in the meridional plane in Figure 5.8b.

The second LB chorus case study from September 14, 1997 occurred from 15:10 to 15:30 UT near 1.8 MLT. This case study is an exception from all of the other Polar orbits containing LB chorus. First, there is an absence of scatter in the latitudinal dependence of

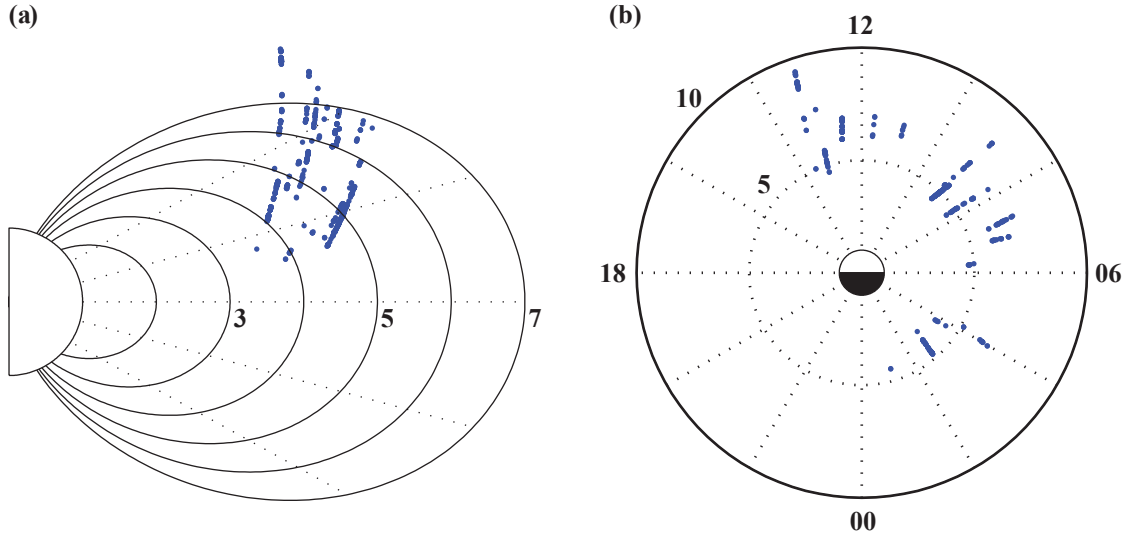


Figure 5.9: (a) Trajectory of the Polar spacecraft in the meridional plane for the 14 orbits containing LB chorus emissions. (b) Distribution of MLT and L -shells.

the wave normal angles, shown in Figure 5.8c, as compared with the other 14 LB chorus case studies. Second, nearly all of the wave normal angles have values of $70^\circ < \theta \leq 90^\circ$ for the magnetic latitudes sampled. The trajectory of the Polar spacecraft, which samples $4^\circ \leq \lambda \leq 12^\circ$ and $3.8 \leq L \leq 4.4$, in the meridional plane is shown in Figure 5.8d. Unfortunately, this is also the only LB case study within 10° of the equatorial plane. This unusual case study is shown for completeness, but will be excluded from the overall statistics. Consequently, the statistics shown in Figures 5.8 through 5.13 will consist of data only from the remaining 14 orbits.

The trajectory of the Polar spacecraft for the remaining 14 orbits containing LB chorus emissions is shown in the meridional plane in Figure 5.9a. The spacecraft samples a broad range of magnetic latitudes, $8^\circ \leq \lambda \leq 43^\circ$, and L -shells, $3.6 \leq L \leq 9.4$. The distribution of magnetic local times, ranging from 1.1 to 13.6, and L -shells for the 14 orbits can be seen in Figure 5.9b.

The overall distribution of wave normal angles over all magnetic latitudes for the 14 LB case studies is illustrated in Figure 5.10. The distribution is uneven, with the majority of wave normal angles having values less than 20° and a secondary peak with lower overall probability in the range of $50^\circ - 60^\circ$.

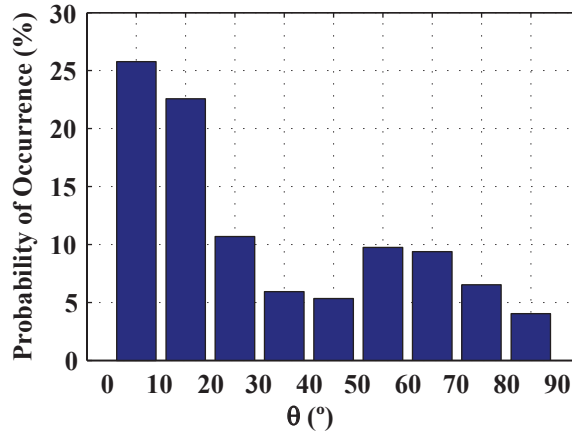


Figure 5.10: Probability of occurrence of wave normal angles over all magnetic latitudes for LB chorus case studies.

Figure 5.11 illustrates the probability of occurrence for different ranges of wave normal angles with respect to three magnetic latitude regions, $10^\circ \leq \lambda < 25^\circ$, $25^\circ \leq \lambda < 40^\circ$, and $40^\circ \leq \lambda < 50^\circ$. As mentioned earlier, the case study from September 14, 1997 is not included in the overall statistical analysis, and thus there is not sufficient data left in the magnetic latitude region $\lambda < 10^\circ$. For each of the other magnetic latitude regions, the probability of occurrence for the wave normal angles is normalized with respect to each latitude region. It can be seen in Figure 5.11 that the probability of occurrence of wave normal angles in the range $\theta < 20^\circ$ increases with increasing magnetic latitude. Contrarily, the higher wave normal angles observed near the magnetic equator have a decreasing relative probability with increasing latitude.

Figure 5.12 shows the absolute value of the difference between the wave normal angle and its corresponding Gendrin angle, defined in Equation 4.3, as a function of magnetic latitude. For magnetic latitudes less than 25° , 20% of the wave normal angles are within 10° of θ_G . These wave normal angles move further away from the Gendrin angle with increasing latitude.

Figure 5.13 illustrates the dependence of the time averaged Poynting flux, S , on wave normal angle. It can be seen from the figure that LB chorus emissions have power levels ranging from 6.9×10^{-10} to 1.5×10^{-6} W/m². As the value of the wave normal angle increases, the wave power decreases, which can be seen by the solid red line representing

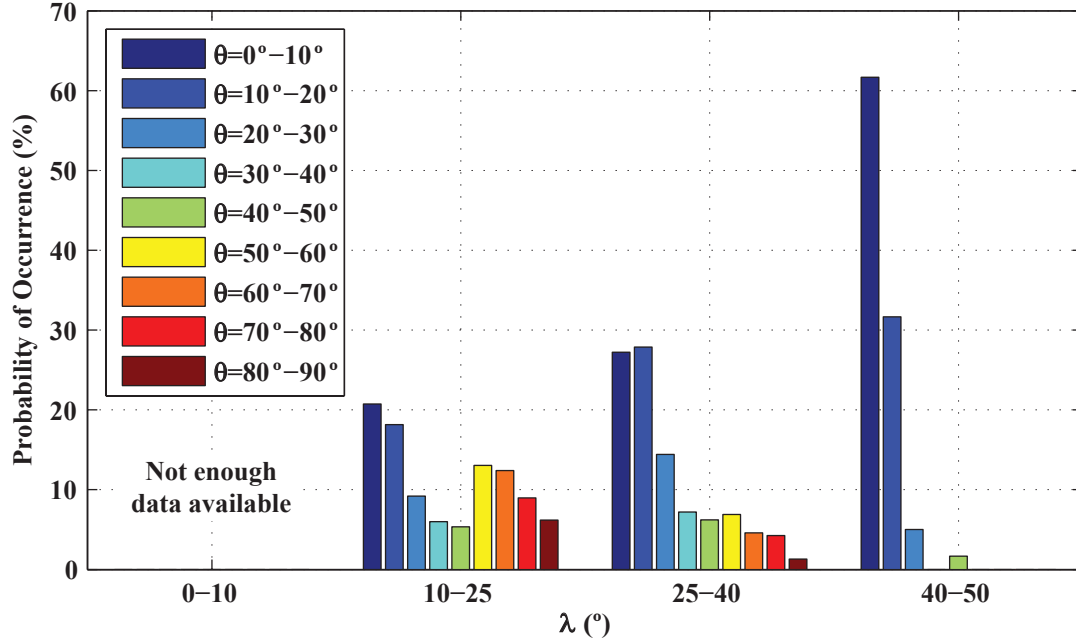


Figure 5.11: Probability of occurrence of wave normal angles, divided in 10° intervals, normalized with respect to each magnetic latitude region for LB chorus emissions.

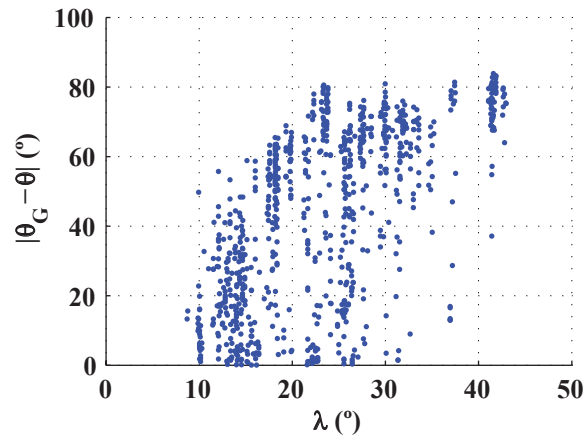


Figure 5.12: Absolute value of the difference between wave normal angle, θ , and the corresponding Gendrin angle, θ_G , with respect to magnetic latitude for LB chorus case studies.

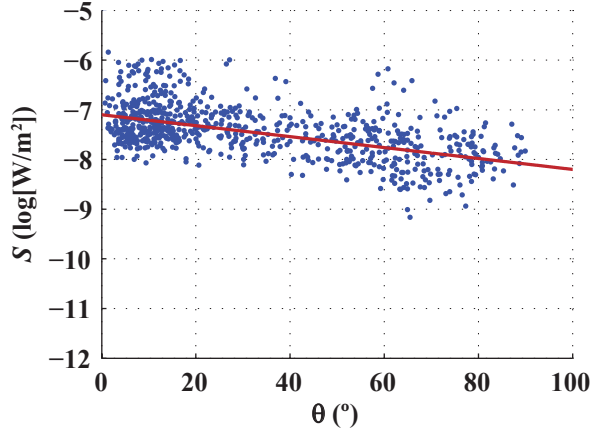


Figure 5.13: Time averaged Poynting flux, S , as a function of wave normal angle for LB chorus emissions. The solid red line represents the linear least squares fit to the data.

the linear least squares fit to the data.

5.5 Comparison With Previous Work

The results from the upper and lower band chorus case studies can be compared to the previous work done on these types of emissions. For the UB chorus case studies, 50% of the wave normal angles at latitudes near the magnetic equator ($\lambda \leq 7^\circ$) have values less than 10° . These results for low latitudes are consistent with those of [Hospodarsky et al. \[2001\]](#), which stated that the wave propagates primarily parallel to the magnetic field for $\lambda < 5^\circ$. They also agree with the conclusion in [Lauben et al. \[2002\]](#) that the wave normal angles in the equatorial source region have values $\theta \simeq 0^\circ$. For some of the other case studies, the wave normal angles are close in value to their corresponding resonance cone angles for all of the magnetic latitudes sampled. This finding agrees with that of [Hayakawa et al. \[1984\]](#), which shows $\theta \sim \theta_R$ near the magnetic equator.

The wave normal angle is very close to the resonance cone angle for all of the UB chorus emissions in the mid-latitude region between $7^\circ \leq \lambda \leq 18^\circ$. This finding is in agreement with the finding of [Muto et al. \[1987\]](#) that $\theta \simeq \theta_R$ at $\lambda \sim 17^\circ$ and the earlier stated results of [Hayakawa et al. \[1984\]](#). Overall, our results are consistent with the assertion of [Lauben et al. \[2002\]](#) that UB chorus is emitted near the equator at $\theta \simeq 0^\circ$, but that propagation away

from the equator quickly moves the wave normal angles close to the resonance cone.

At higher latitudes, $\lambda > 18^\circ$, the wave normal angles of UB chorus are observed to move away from the resonance cone by an average value of 30° . This effect was also reported by [Muto et al. \[1987\]](#). It is likely that the lack of high wave normal angles at higher latitudes is the result of Landau damping [[Lauben et al., 2002](#)]. Waves near the resonance cone are expected to be strongly Landau damped as they propagate [[Burton and Holzer, 1974](#)]. Thus, the only waves with observable amplitudes at the higher latitudes are those with wave normal angles away from the resonance cone.

For the unusual LB chorus case study, occurring on September 14, 1997, it can be seen that the wave normal angles are grouped around $\theta = 80^\circ$ for magnetic latitudes less than approximately 12° . This case is in stark contrast to previous reports on LB chorus [e.g., [Burton and Holzer, 1974](#); [Goldstein and Tsurutani, 1984](#); [Hayakawa et al., 1984](#); [Hospodarsky et al., 2001](#)], and as far we are aware, it is the only reported case of LB chorus of this type.

At all latitudes sampled by Polar, LB chorus has the highest probability of occurrence for $\theta < 20^\circ$. In addition, as the waves propagate to higher magnetic latitudes, the relative probability of observing chorus for $\theta < 20^\circ$ increases. For example, for $10^\circ \leq \lambda < 25^\circ$, wave normal angles have values less than 20° for $\sim 40\%$ of the time, while for $\lambda \geq 40^\circ$ the occurrence is greater than 90% . This result might be explained by the suggestion by [Burton and Holzer \[1974\]](#) that ducts are necessary to allow LB chorus waves to reach latitudes in the range of 40° - 50° . The small values of wave normal angles at higher magnetic latitudes may also be explained by the nonducted propagation of waves with high wave normal angles, near the Gendrin angle, directed towards the Earth in the source region [[Chum and Santolík, 2005](#); [Santolík et al., 2006](#)].

In contrast, wave normal angles with values $\theta \geq 20^\circ$ have a decreasing probability of occurrence as the LB chorus wave propagates to higher magnetic latitudes. According to [Lauben et al. \[2002\]](#), waves observed on the Polar spacecraft with high wave normal angles will soon be Landau damped at higher magnetic latitudes. In support of this, [Burton and Holzer \[1974\]](#) state that wave normal angles with values greater than 60° will rarely be detected at high latitudes due to strong attenuation. Thus, before the Polar spacecraft is able to sample the high magnetic latitudes, the waves will have been strongly damped,

explaining the absence of high wave normal angles in this region.

For the LB chorus emissions, it was seen that the portion of wave normal angles that start near the Gendrin angle tend to move away from the Gendrin angle with increasing values of magnetic latitude. It is possible that some fraction of LB chorus waves are generated at the Gendrin angle, as was concluded by [Lauben et al. \[2002\]](#), within depletion ducts in the source region.

For each of the orbits of both types of emissions, the wave normal angles used for this study were those that corresponded to any frequency that satisfied the frequency dependent threshold and for which chorus was detected. There does exist a small variation in wave normal angle with respect to frequency, though there is no systematic trend to this variation. Specifically, at any given time step, the average spread of the wave normal angle over frequency is $\sim 2^\circ$ for UB chorus and $\sim 8^\circ$ for LB chorus.

The time averaged Poynting flux was calculated for both upper and lower band chorus emissions, illustrating that the UB chorus waves have power levels that are 60 times smaller than those of the LB chorus waves on average. This difference is supported by past work, which states that the lower band of chorus is more intense than the upper band [[Bortnik et al., 2008](#); [Bortnik et al., 2009](#)]. The trend for each band is also different, with the power distributed about its median value for UB chorus waves and an inversely proportional relationship between the power and wave normal angle for LB chorus waves.

5.6 Summary

Data from the HFWR onboard the Polar spacecraft was used to analyze wave normal angles from 13 orbits containing UB chorus emissions and 15 orbits containing LB chorus emissions. Due to the highly elliptical orbit of the Polar spacecraft, it is impossible to distinguish between latitudinal and L -shell variations in the distribution of wave normal angles. However, since the effect of the propagation of waves from the equatorial source region to the off-equatorial region is expected to be much stronger on the wave normal distribution than variations with L -shell, the distribution of wave normal angles were characterized as a function of magnetic latitude only.

There were two types of wave normal angles observed for UB chorus emissions. The

first are wave normal angles with values $\theta < 20^\circ$ for magnetic latitudes $\lambda < 10^\circ$, which quickly rise to values close to the resonance cone with increasing latitude. The second are wave normal angles that remain near the resonance cone angle for $7 \leq \lambda \leq 18^\circ$. For either type, the wave normal angle moves away from the resonance cone angle at high latitudes, $\lambda > 18^\circ$, by an average of 30° .

For LB chorus emissions, wave normal angles tend to be scattered with respect to magnetic latitude and the majority of the wave normal angles occur in the range $\theta < 20^\circ$. Wave normal angles have values $\theta < 20^\circ$ with increasing probabilities of occurrence as magnetic latitude increases. For magnetic latitudes less than 25° , 20% of the wave normal angles are within 10° of the Gendrin angle.

Regarding the time averaged Poynting flux, LB chorus waves have power levels that are 60 times larger on average than UB chorus waves. The time averaged Poynting flux is fairly evenly distributed about its median value for all wave normal angles for UB chorus emissions. The time averaged Poynting flux decreases with respect to wave normal angle for LB chorus emissions.

The conclusions from this study establish a broader understanding of the distribution of chorus wave normal angles. These results are important for further studies of resonant interactions between chorus waves and electrons over a wide range of energies.

Chapter 6

Spatial Dependence of Chorus Intensity

In this chapter, data from 19 different Cluster orbits containing banded chorus emissions, with observations from 51 different passes spread across the four Cluster spacecraft, are used to show the spatial dependence of banded chorus intensity near the magnetic equator under conditions of moderate magnetic disturbance ($K_p \leq 5$). The intensities for UB and LB chorus were manually determined from E field spectrograms. Approximately half the spacecraft observations showed a complete absence of chorus emissions within 1° of the magnetic equator. Two cases of banded chorus intensity are examined: 1) October 31, 2003 with chorus present near the magnetic equator and 2) September 19, 2003 without chorus present near the magnetic equator. These cases are followed by statistics for the spatial dependence of banded chorus intensity over all orbits.

The intensity, I , of the chorus emissions is found to generally increase exponentially with distance, z , away from the magnetic equator according to the relation $I = I_o e^{\alpha z}$, where α is the spatial growth factor. For our data set, the probability of occurrence of exponential dependence of chorus intensity on magnetic latitude is $\sim 86\%$ for LB chorus and $\sim 63\%$ for UB chorus. The $f(\alpha) \simeq \alpha^2 e^{-\alpha}$ distribution of α provides a new boundary condition for consideration in current and future chorus generation models.

6.1 Chorus Intensity

Chorus emissions are believed to accelerate radiation belt electrons with energies of 10 to 100 keV to relativistic energies during and after geomagnetic storms [Meredith *et al.*, 2003]. Previous studies have generally concerned the dependence of chorus intensity on substorm activity. Thorne *et al.* [1974] studied ELF dawn chorus emissions, with frequency range 100 to 1000 Hz, concluding that chorus increases in intensity during a substorm and is most intense for $L > 4$. Meredith *et al.* [2001] did a detailed study of chorus intensities, using CRRES measurements, for both upper and lower band chorus as a function of L -shell and MLT. They found that chorus within 15° of the equator had the largest intensities for MLTs between 23.0 and 13.0 hours and L -shells between 3 and 7.

These early studies mainly focus on the L -shell and magnetic activity dependence of chorus intensity. In contrast, there has been little work concerning the intensity of chorus in the source region close to the magnetic equator. Since chorus is believed to be generated near the magnetic equatorial plane [LeDocq *et al.*, 1998], it is important to study the spatial dependence of chorus intensity as a function of magnetic latitude, λ , in order to better understand the chorus generation process.

The present study aims to determine the spatial dependence of chorus intensity near the magnetic equator by analyzing 19 different Cluster orbits containing banded chorus emissions, with observations from a total of 51 different passes spread across the four Cluster spacecraft. These passes are the same as the ones from Chapter 4, with the trajectory and distribution of MLT and L -shell of Cluster shown in Figure 4.7. The banded chorus passes were chosen to include the source region, roughly defined as magnetic latitudes within 5° of the magnetic equator for this study. The magnetic equator is determined using the current IGRF internal field model, along with the Tsyanenko T89c external field model, with $K_p = 3$. The 51 passes were chosen such that the K_p index at the time was less than 5, with an average K_p of 3.15, indicating low to moderate storm-level geomagnetic activity and that the location of the magnetic equator could be reasonably determined [Santolík *et al.*, 2009].

6.2 Case I: October 31, 2003

Figure 6.1 shows Cluster 3 observations of banded chorus on October 31, 2003 during 23:01:02-23:07:54 UT for magnetic latitudes -3° to 0° . The E field spectrogram in Figure 6.1a shows the two distinct bands of chorus separated by an emission gap at $f_{ce}/2$, indicated by the white line. Though the upper and lower bands of chorus are not absent at the magnetic equator, the intensity of the emissions appears to be much weaker in this region and also appears to increase with distance away from the magnetic equator.

The values of the average intensities of the upper and lower chorus bands were manually determined from frequency-time spectrograms, which were divided into 1-minute intervals. For each 10 ms time bin, the average intensity was calculated by integrating the wave spectral density ($\text{V}^2\text{m}^{-2}\text{Hz}^{-1}$) over the frequency range $0.1f_{ce} \leq f < f_{ce}/2$ for LB chorus and $f_{ce}/2 \leq f \leq f_{ce}$ for UB chorus. This wave intensity (V/m) was then averaged over a one second period.

The logarithm of the chorus intensities for upper and lower band chorus is plotted as a function of magnetic latitude as shown in Figures 6.1b and 6.1c by the red points, respectively. The chorus is seen to be weak near the magnetic equator and increases exponentially with distance from the equator. An intensity of 10^{-5} V/m indicates the background noise level for each band. A narrowband moving average filter, with bandwidth 15 Hz and 10 ms time resolution, was applied to the center frequency of each chorus band, which was 3.8 kHz for LB chorus and linearly increased from 6.4 to 7.7 kHz for UB chorus. The output of the filter, which was interpolated to fill in the gaps where there were no data from the electric antenna, provides a reasonable fit for each band and is shown as a solid blue line in Figures 6.1b and 6.1c.

For both upper and lower band chorus, the envelope of the intensity near the magnetic equator generally has an exponential dependence on magnetic latitude. An example of this exponential dependence is shown by the solid portion of the black lines in Figure 6.1b and 6.1c. The exponential rise near the magnetic equator can be modeled by $I = I_0 e^{\alpha z}$, where I represents intensity, α represents the spatial growth factor, and z represents distance in km from the equator. For this case, the exponential rise near the magnetic equator has $\alpha = 1.08 \times 10^{-3} \text{ km}^{-1}$ for UB chorus and $\alpha = 2.74 \times 10^{-3} \text{ km}^{-1}$ for LB chorus.

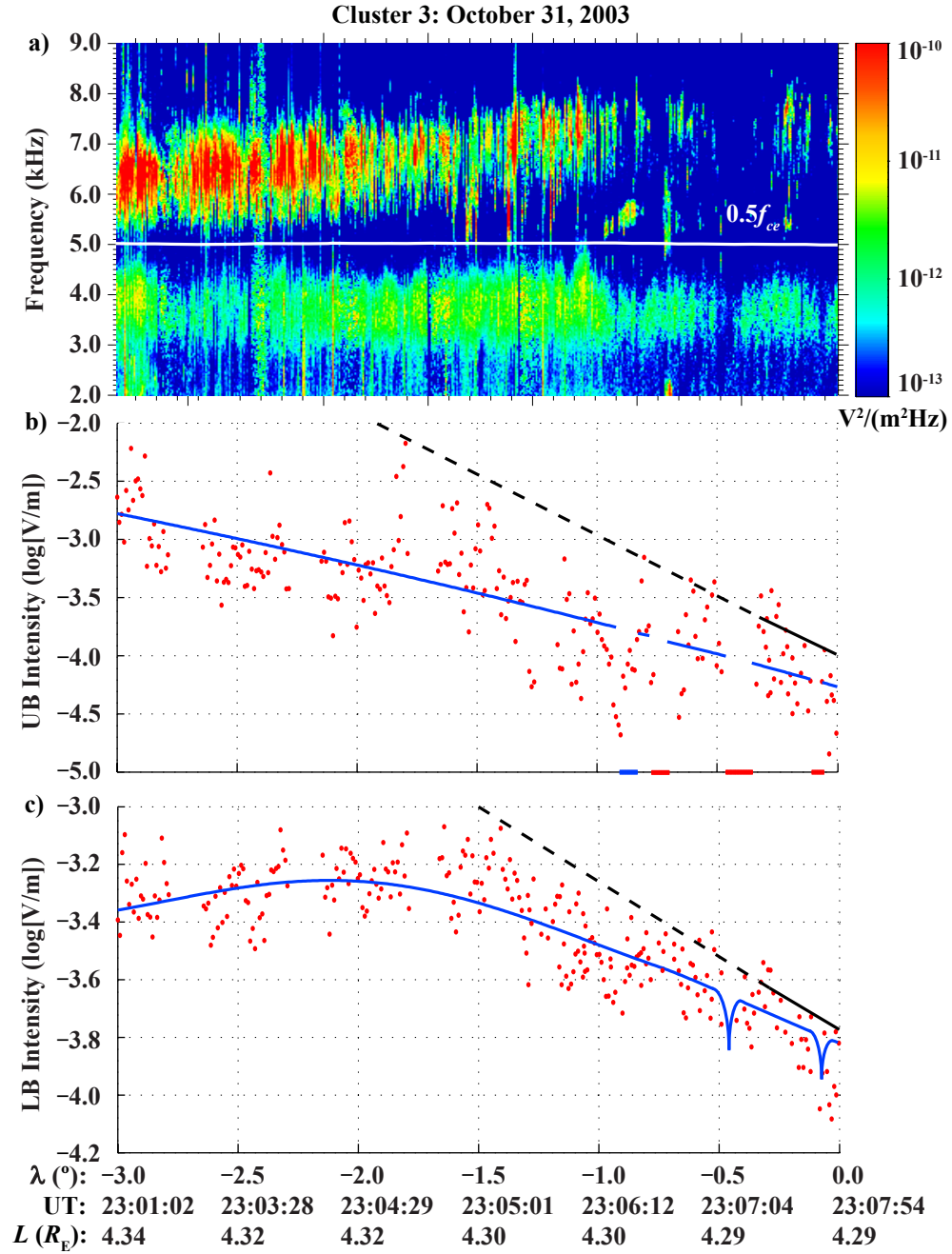


Figure 6.1: Measurements for Cluster 3 on October 31, 2003 during 23:01:02-23:07:54 UT. (a) E field spectrogram showing a pass with banded chorus. (b) The logarithm of UB and (c) LB chorus intensity as a function of λ is shown in red. The output of the narrowband moving average filter is shown in blue, while the envelope of the intensity is shown in black. Ephemeris data for Cluster 3 is given on the bottom.

6.3 Case II: September 19, 2003

Surprisingly, in approximately half of the cases, there was an absence of chorus emissions within 1° (~ 500 km) of the magnetic equator. An example of this behavior is shown in Figure 6.2, which displays Cluster 2 observations of banded chorus on September 19, 2003 during 03:35:45-03:44:19 UT. The data are shown for magnetic latitudes -5° to 0° . The weak emissions observed near $\lambda \sim -1^\circ$ appear to be chorus, but do not appear to conform to the banded configuration. Upper and lower chorus bands are observed until the region near the magnetic equator is approached. Outside this zone of exclusion, the chorus intensity is seen to increase with distance away from the magnetic equator.

A number of impulses can be seen in the spectrogram of Figure 6.2a, some of which are marked by arrows on the time axis. These impulses are artifacts of the fact that the automatic gain control (AGC) system of the WBD instrument does not update rapidly enough. In determining the intensities of each chorus band, each 1-minute spectrogram is also visually inspected. If the emissions appeared to be AGC-produced impulses, they are not included in the integration of the wave spectral density. Therefore, the intensities calculated are only for each band of chorus.

Figures 6.2b and 6.2c show in red the logarithm of the chorus intensities for upper and lower band chorus, respectively, with respect to magnetic latitude. An intensity of 10^{-7} V/m indicates the background noise level for each band. For both upper and lower band chorus, the intensity appears to increase with distance away from the magnetic equator. A moving average narrowband filter is applied to the center frequency of each chorus band, set to be 6.2 kHz for UB chorus and 4.5 kHz for LB chorus. The output of the filter provides a reasonable fit for each band and is shown as a solid blue line in Figures 6.2b and 6.2c. The exponential rise near the magnetic equator, shown by the solid portion of the black lines in Figures 6.2b and 6.2c, has $\alpha = 1.08 \times 10^{-3} \text{ km}^{-1}$ for UB chorus and $\alpha = 2.74 \times 10^{-3} \text{ km}^{-1}$ for LB chorus.

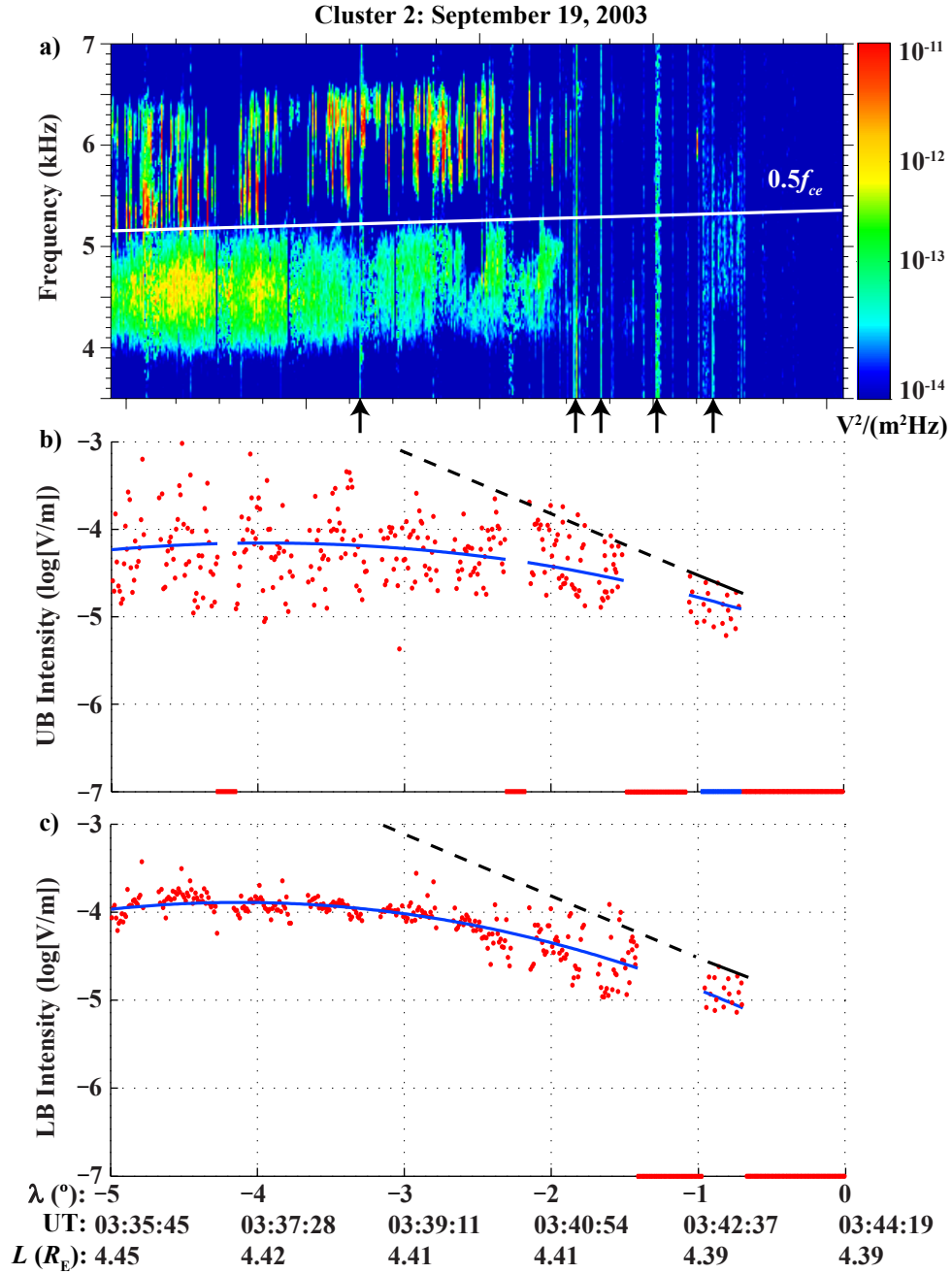


Figure 6.2: Measurements for Cluster 2 on September 19, 2003 during 03:35:45-03:44:19 UT. (a) E field spectrogram showing a pass with banded chorus. (b) The logarithm of UB and (c) LB chorus intensity as a function of λ is shown in red. The output of the narrowband moving average filter is shown in blue, while the envelope of the intensity is shown in black. Ephemeris data for Cluster 2 is given on the bottom.

6.4 Spatial Dependence Statistics

The two cases from September 19, 2003 and October 31, 2003, shown above, are representative of the entire banded chorus set in this study. A band of chorus is assumed to be exponentially dependent on distance away from the magnetic equator if $\alpha > 0.1 \times 10^{-3} \text{ km}^{-1}$. The value of α is determined by the solid portion of the black lines in Figures 6.1b, 6.1c, 6.2b, and 6.2c. The probability of occurrence of exponential dependence of chorus intensity as a function of distance from the magnetic equator over all orbits is $\sim 86\%$ for LB chorus and $\sim 63\%$ for UB chorus. The chorus that do not have this exponential spatial dependence may have been uniformly generated over an extended region, as described in Section 4.2.1.

The probability of occurrence of different ranges of α for both upper and lower band chorus over all orbits is shown in Figure 6.3. For both bands of chorus, α has the highest probability of occurrence in the range $0.9\text{--}1.8 \times 10^{-3} \text{ km}^{-1}$. This peak probability of occurrence is 28.7% for LB chorus and 25.3% for UB chorus. The rise in probability of occurrence from smaller α to the peak is much less steep than the fall in probability of occurrence from the peak to larger α . For both bands of chorus, the second highest peak occurs for α in the range $1.8\text{--}2.7 \times 10^{-3} \text{ km}^{-1}$. The overall distribution of α over all orbits for each band is $f(\alpha) \simeq \alpha^2 e^{-\alpha}$, though it is a slightly better fit for UB chorus than LB chorus. An example of this type of Poisson distribution is shown as a red line in Figure 6.3.

For the majority of the chorus cases analyzed, the average intensity of both bands of chorus is exponentially dependent on distance away from the magnetic equator. In our method, the average intensity of the chorus emissions can increase either due to an increase in the number of chorus elements per unit length or due to an intensity increase in each chorus element if the number of elements per unit length is constant. Though the increase in intensity may be partly due to an increase in number of chorus elements, the majority of the increase in intensity away from the magnetic equator appears to be predominantly due to an increase in intensity of the chorus elements, as seen in Figure 6.4.

Figure 6.4a shows observations of two UB chorus elements from Cluster 3 on October 31, 2003 during 23:07:02–23:07:04 UT for $\lambda = 0.11^\circ$. On this same day during 23:06:00–23:06:02 UT, at a distance further away from the magnetic equator at $\lambda = -1.12^\circ$, two

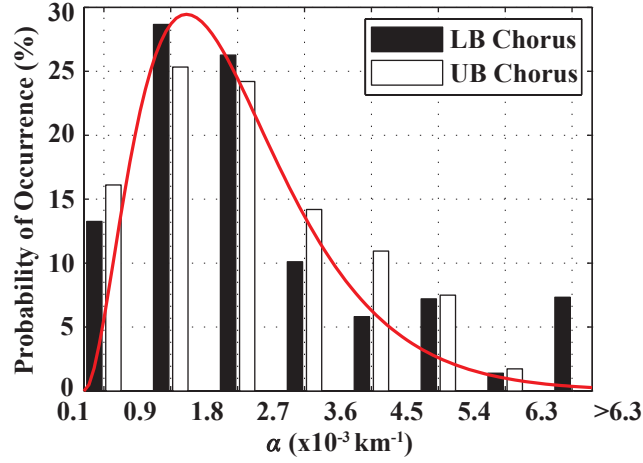


Figure 6.3: Probability of occurrence of different ranges of spatial growth factor, α , for LB and UB chorus over all orbits. The overall distribution of α is $f(\alpha) \propto \alpha^2 e^{-\alpha}$, shown by the red line.

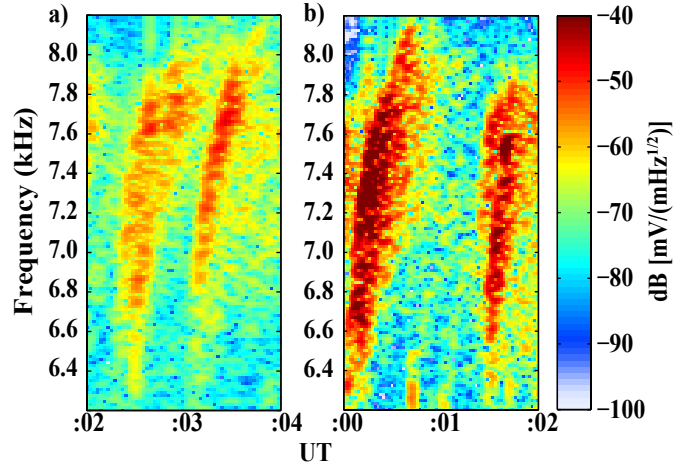


Figure 6.4: E field spectrograms for Cluster 3 observations of UB chorus on October 31, 2003. (a) Two chorus elements observed during 23:07:02-23:07:04 UT at $\lambda = 0.11^\circ$. (b) Two much more intense chorus elements observed during 23:06:00-23:06:02 UT further away from the magnetic equator at $\lambda = -1.12^\circ$.

much more intense UB chorus elements are observed in Figure 6.4b. For this example, the number of chorus elements per unit distance did not increase with distance away from the magnetic equator during the 2 second period of observation, but rather only the intensity of the elements increased.

The similarity in form of the chorus elements suggests that chorus may be generated at low intensity near the magnetic equator, and subsequently amplified to greater intensity as the elements propagate away from the generation point. The amplification mechanism may be linear or nonlinear gyroresonance with energetic electrons. The electron flux, averaged over a pitch angle range of 87.27° to 92.75° , from observations by the PEACE instrument [Johnstone *et al.*, 1997] onboard Cluster 3 on October 31, 2003, seems to provide support for this theory. The particles measured had energies in the 10–25 keV range, with the highest flux occurring at approximately 1.23° to 1.82° off the magnetic equator.

The spatial dependence of chorus intensity near the magnetic equator has not previously been studied or considered in chorus generation models, such as those described in Omura *et al.* [2008] and Trakhtengerts [1999]. In the Omura *et al.* [2008] model, the growth of the wave amplitude of chorus is studied as a function of time. Initially, this wave growth is found to be linear, after which the wave amplitude grows nonlinearly until it saturates.

The backward wave oscillator (BWO) model [Trakhtengerts, 1999] of chorus generation relates this process to an absolute instability of chorus waves, which can occur in the presence of a step-like feature in the electron distribution function. This step-like feature may arise naturally from the cyclotron resonance interaction of Equation 1.4. It is proposed that electrons with this distribution function move along the magnetic field, usually in regions on the order of 2000 km, and independently generate chorus waves propagating in opposite directions. Therefore, the distribution of α in this study provides important insight into the spatial dependence of chorus intensity.

6.5 Summary

Data from 19 different Cluster orbits containing banded chorus emissions show that for moderate magnetic disturbances, there are two main configurations of chorus, one for which there is no chorus present within 1° of the magnetic equator and one for which

there are only weak chorus emissions present in this region. For either configuration, the envelope of the intensity of banded chorus near the magnetic equator generally has an exponential spatial dependence on distance z away from the magnetic equator, expressed as $I = I_o e^{\alpha z}$. LB chorus intensity has an exponential dependence on magnetic latitude with a probability of $\sim 86\%$, while UB chorus intensity has this dependence with a probability of $\sim 63\%$. The $f(\alpha) \simeq \alpha^2 e^{-\alpha}$ distribution of α provides a new boundary condition for consideration in current and future models of the chorus generation mechanism.

Chapter 7

Summary and Future Research

7.1 Summary of Major Results

Banded chorus emissions are natural electromagnetic plasma waves that are observed in two distinct bands with an emission gap at $f_{ce}/2$ in the magnetosphere outside the plasma-pause. Chorus waves can increase the flux of relativistic electrons by accelerating electrons with energies in the keV range to energies in the MeV range. These relativistic electrons pose a serious hazard for spacecraft systems, as they may cause damage to onboard electronics or even cause a system failure. This dissertation provides a better understanding of the source region characteristics of banded chorus emissions.

Though chorus is believed to be generated through a cyclotron resonance interaction near the magnetic equator, there is no accepted explanation for why the banded structure of chorus is observed. A new theory suggesting banded chorus is generated within whistler-mode ducts is described in Chapter 2. This theory states that UB chorus can be guided by depletion ducts for all θ and LB chorus can be guided by depletion ducts for $\theta \gtrsim \theta_G$ and by enhancement ducts for $\theta < \theta_G$.

To test this theory, high resolution electron density observations were carried out as described in Chapter 3 using the EFW and WHISPER instruments onboard the Cluster spacecraft. The plasma frequency determined from EFW, using the spacecraft potential, has a time resolution of 0.2 seconds. While the time resolution of data from EFW is higher

than that of WHISPER, the EFW data must be calibrated using the WHISPER data. WHISPER operates in the passive mode where only natural electric emissions are monitored and in the active mode where the transmitter sends pulses that stimulate resonances in the magnetosphere. These resonances include the plasma frequency, upper hybrid frequency, gyrofrequency and its harmonics, and the Bernstein mode frequencies. The plasma frequency from WHISPER is interpolated with that from EFW, from which the electron density is calculated. The electron density determined from this process has the highest spatial resolution to date of 17 km, a time resolution of 0.2 seconds, and an accuracy within 1%. Irregularities in the electron density profile are classified as ducts if they satisfy two ducting requirements, based on previous studies. The first is the half-width, which must be between ~ 5 and ~ 45 wavelengths, and the second is the enhancement or depletion factor, which must be greater than or equal to 10%.

The electron density profiles that are derived from EFW and WHISPER data are used to analyze the relationship between banded chorus and ducts, as investigated in Chapter 4. Two case studies from October 31, 2003 and January 20, 2004 demonstrate that LB chorus can be guided by and generated within whistler-mode enhancement and depletion ducts, respectively. The case from January 20, 2004 provided further insight into LB chorus excitation, suggesting that uniform chorus generation over an extended region of ~ 500 km may be common. The two case studies are representative of the larger data set, which consists of 19 Cluster orbits with 51 different passes spread across the 4 spacecraft. These passes all contain observations of banded chorus and ducts, and include the source region of chorus, which is near the magnetic equator. For this data set, LB chorus emissions were found to be generated within ducts located at the same L -shell within $\sim 3^\circ$ of the magnetic equator. The wave normal angle distribution for the chorus generated within ducts show that the majority of chorus waves can also be guided by whistler-mode ducts. For depletion ducts, $\theta \gtrsim \theta_G$ occurs with a probability of $\sim 87\%$, while for enhancement ducts, $\theta < \theta_G$ occurs with a probability of $\sim 91\%$.

In Chapter 5, wave normal angles for UB and LB chorus emissions are analyzed in both the equatorial and off-equatorial regions, spanning magnetic latitudes up to 50° , using data from the Polar spacecraft. The wave normal angle is characterized as a function of magnetic latitude. For LB chorus, $\theta < 20^\circ$ with increasing probability as the magnetic

latitude increases. 20% of the wave normal angles for LB chorus have values within 10° of the Gendrin angle. For UB chorus, $\theta < 20^\circ$ for $\lambda < 10^\circ$ and rise toward the resonance cone, while $\theta \sim \theta_R$ for $7^\circ \leq \lambda \leq 18^\circ$. For both cases, the wave normal angles move away from the resonance cone angle for $\lambda > 18^\circ$. LB chorus waves have a time averaged Poynting flux that is 60 times greater than that of UB chorus waves. S decreases with θ for LB chorus, but is distributed evenly about the median value of θ for UB chorus. The wave normal angle distribution is important in evaluating resonance wave-particle interactions.

To further understand the source region characteristics of banded chorus, the spatial dependence of chorus intensity is investigated in Chapter 6. Using the same data set as Chapter 4, two configurations of banded chorus were observed, one with chorus absent within 1° of the magnetic equator and one with only weak chorus emissions in this region. For both configurations, the intensity of banded chorus generally has an exponential spatial dependence on distance away from the magnetic equator. UB chorus intensity has this dependence with a probability of $\sim 63\%$, while LB chorus intensity has it with a probability of $\sim 86\%$. The distribution of the spatial growth factor provides a new boundary condition for chorus generation models.

7.2 Suggestions for Future Research

This dissertation provides many new contributions to our understanding of the source region characteristics of banded chorus emissions, as well as opportunities for future research. Concerning the observations discussed in Chapter 3, an automated process could be developed to determine the plasma frequency from the active spectra of WHISPER. This process could then be used in conjunction with the plasma frequency from the passive spectra of WHISPER and the data from EFW to determine the total plasma frequency and electron density. Once the electron density is calculated, an automated process could also be developed to identify ducts based on the ducting requirements. If these processes are developed, many more cases of banded chorus and ducts may be analyzed for a larger time period and set of L -shells.

In Chapter 4, the LB chorus on January 20, 2004 was one of the first cases observed with oblique wave normal angles, as LB chorus generally tends to have small wave normal

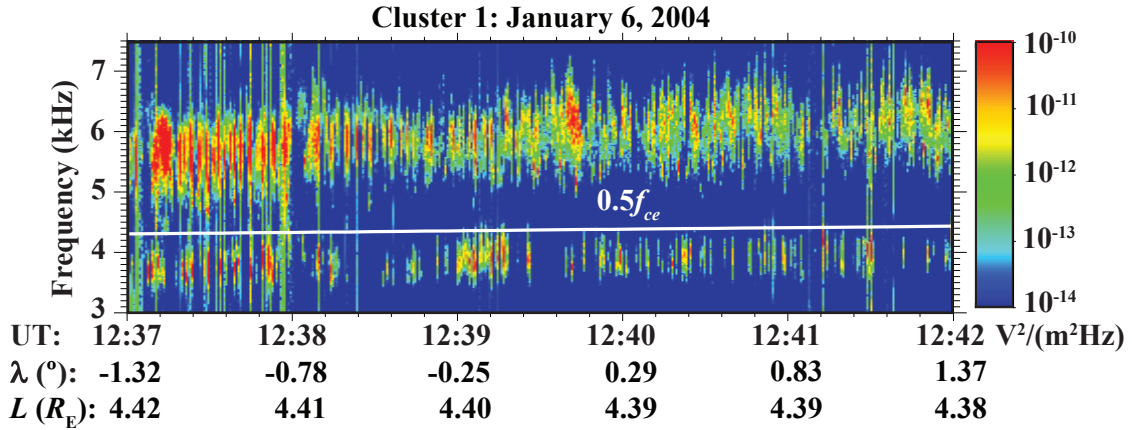


Figure 7.1: E Field spectrogram from Cluster 1 showing a pass with banded chorus on January 6, 2004 during 12:37:00-12:42:00 UT. Ephemeris data for Cluster 1 is given on the bottom.

angles. Finding other cases with oblique wave normal angles would be important to identify whether it is common for LB chorus to be uniformly excited over an extended region of ~ 500 km. A spectrogram for a similar pass with banded chorus emissions observed on January 6, 2004 during 12:37:00-12:42:00 UT is shown in Figure 7.1. Wave normal angle and duct analysis of this pass and other such passes could give more insight on how often uniform excitation of LB chorus occurs.

The wave normal angle analysis was limited to LB chorus for the data set in this study due to the upper frequency limitation of the STAFF instrument to 4 kHz. In order to determine the wave normal angles for UB chorus using STAFF, passes must be found that contain UB chorus with frequencies below 4 kHz. A different satellite system could also be used in the future that provides measurements of all three magnetic field components and at least two electric field components, which is necessary to determine the wave normal angle. To analyze the relationship between UB chorus and ducts, this satellite system would also have to have the ability to determine electron density with high spatial resolution and accuracy.

The electron density profile in Figure 2.2a shows maxima that have values that are 2 to 4 times that of one of the adjacent minima between the peaks. Since the electron density affects the resonance condition of Equation 1.4, this suggests that very different

groups of energetic electrons may be involved in the excitation of the two chorus bands, even though the two bands are generally separated in frequency by less than 500 Hz. The minimum energy of nonrelativistic electrons that undergo cyclotron resonance with parallel propagating chorus waves can be calculated from the expression

$$E_{\min} = \frac{B^2}{8\pi N_e} \frac{f_{ce}}{f} \left(1 - \frac{f}{f_{ce}}\right)^3 \quad (7.1)$$

[[Li et al., 2011b](#)]. For typical frequencies in the magnetosphere, $1 < f_{pe}/f_{ce} < 5$, a particle-in-cell demonstration suggests that UB chorus can be excited by electrons with energies below ~ 1 keV and that LB chorus can be excited by electrons with energies above ~ 10 keV [[Liu et al., 2011](#)]. These results could be verified by analyzing the measurements of energetic electrons from the PEACE instrument onboard Cluster and correlating it with UB and LB chorus emissions observed in the WBD data.

In Chapter 6, the intensity of the upper and lower chorus bands were manually determined. In order to look at a larger data set in less time, an automated process to detect and isolate the two bands of chorus, as well as take out the impulses from the AGC, could be developed. A new chorus generation model could also be developed using the new boundary condition provided by the distribution of α , as well as the wave normal angle distributions provided by this dissertation. The results of this future research will continue to advance our fundamental understanding of the source region characteristics of magnetospheric ELF/VLF banded chorus emissions.

Bibliography

- Allcock, G. M. (1957), A study of the audio-frequency radio phenomenon known as 'dawn chorus', *Aust. J. Phys.*, *10*, 286–298.
- Angerami, J. J. (1970), Whistler Duct Properties Deduced from VLF Observations Made with the Ogo 3 Satellite near the Magnetic Equator, *J. Geophys. Res.*, *75*, 6115–6135, doi:10.1029/JA075i031p06115.
- Appleton, E. V. (1932), Wireless Studies of the Ionosphere, *J. Inst. Elec. Engrs.*, *71*, 642.
- Baker, D. N. (2000), The occurrence of operational anomalies in spacecraft and their relationship to space weather, *IEEE Transactions on Plasma Science*, *28*, 2007–2016, doi: 10.1109/27.902228.
- Balogh, A., M. W. Dunlop, S. W. H. Cowley, D. J. Southwood, J. G. Thomlinson, K. H. Glassmeier, G. Musmann, H. Luhr, S. Buchert, M. H. Acuna, D. H. Fairfield, J. A. Slavin, W. Riedler, K. Schwingenschuh, and M. G. Kivelson (1997), The Cluster Magnetic Field Investigation, *Space Sci. Rev.*, *79*, 65–91, doi:10.1023/A:1004970907748.
- Bartels, J., N. H. Heck, and H. F. Johnston (1939), The Three-Hour Index Measuring Geomagnetic Activity, *Terrestrial Magnetism and Atmospheric Electricity (Journal of Geophysical Research)*, *44*, 411–454, doi:10.1029/TE044i004p00411.
- Bell, T. F., U. S. Inan, and R. A. Helliwell (1981), Nonducted coherent VLF waves and associated triggered emissions observed on the ISEE-1 satellite, *J. Geophys. Res.*, *86*, 4649–4670, doi:10.1029/JA086iA06p04649.

- Bell, T. F., U. S. Inan, N. Haque, and J. S. Pickett (2009), Source regions of banded chorus, *Geophys. Res. Lett.*, *36*, L11101, doi:10.1029/2009GL037629.
- Bernstein, I. B. (1958), Waves in a Plasma in a Magnetic Field, *Physical Review*, *109*, 10–21, doi:10.1103/PhysRev.109.10.
- Bortnik, J., U. S. Inan, and T. F. Bell (2006), Landau damping and resultant unidirectional propagation of chorus waves, *Geophys. Res. Lett.*, *33*, L03,102, doi:10.1029/2005GL024553.
- Bortnik, J., R. M. Thorne, and N. P. Meredith (2008), The unexpected origin of plasmaspheric hiss from discrete chorus emissions, *Nature*, *452*(7183), 62, doi:10.1038/nature06741.
- Bortnik, J., W. Li, R. M. Thorne, V. Angelopoulos, C. Cully, J. Bonnell, O. Le Contel, and A. Roux (2009), An Observation Linking the Origin of Plasmaspheric Hiss to Discrete Chorus Emissions, *Science*, *324*, 775–778, doi:10.1126/science.1171273.
- Burch, J. L., and V. Angelopoulos (2009), *The THEMIS Mission*, Springer-Verlag New York Inc., New York, NY, doi:10.1007/978-0-387-89820-9.
- Burtis, W. J., and R. A. Helliwell (1969), Banded chorus: A new type of VLF radiation observed in the magnetosphere by OGO 1 and OGO 3, *J. Geophys. Res.*, *74*, 3002–3010.
- Burtis, W. J., and R. A. Helliwell (1975), Magnetospheric chorus: Amplitude and growth rate, *J. Geophys. Res.*, *80*, 3265–3270.
- Burtis, W. J., and R. A. Helliwell (1976), Magnetospheric chorus: Occurrence patterns and normalized frequency, *Planet. Space Sci.*, *24*, 1007–1024.
- Burton, R. K., and R. E. Holzer (1974), The origin and propagation of chorus in the outer magnetosphere, *J. Geophys. Res.*, *79*, 1014–1023.
- Canu, P., P. M. E. Décréau, J. G. Trotignon, J. L. Rauch, H. C. Seran, P. Ferreau, M. Lévêque, P. Martin, F. X. Sené, E. Le Guirriec, H. Alleyne, and K. Yearby (2001), Identification of natural plasma emissions observed close to the plasmopause by the Cluster-Whisper relaxation sounder, *Ann. Geophys.*, *19*, 1697–1709.

- Carpenter, D. L., and R. R. Anderson (1992), An ISEE/Whistler model of equatorial electron density in the magnetosphere, *J. Geophys. Res.*, *97*, 1097–1108, doi:10.1029/91JA01548.
- Chum, J., and O. Santolík (2005), Propagation of whistler-mode chorus to low altitudes: divergent ray trajectories and ground accessibility, *Ann. Geophys.*, *23*, 3727–3738.
- Chum, J., O. Santolik, D. A. Gurnett, and J. S. Pickett (2009), Oblique lower band chorus waves: Time shifts between discrete elements observed by the Cluster spacecraft, *J. Geophys. Res.*, *114*, A00F02, doi:10.1029/2009JA014366.
- Cornilleau-Wehrlin, N., G. Chanteur, S. Perraut, L. Rezeau, P. Robert, A. Roux, C. de Villedary, P. Canu, M. Maksimovic, Y. de Conchy, D. H. C. Lacombe, F. Lefeuvre, M. Parrot, J. L. Pinçon, P. M. E. Décréau, C. C. Harvey, P. Louarn, O. Santolik, H. S. C. Alleyne, M. Roth, T. Chust, O. Le Contel, and Staff Team (2003), First results obtained by the Cluster STAFF experiment, *Ann. Geophys.*, *21*, 437–456.
- Décréau, P. M. E., P. Ferreau, V. Krannosels'kikh, M. Leveque, P. Martin, O. Randriamboarison, F. X. Sene, J. G. Trotignon, P. Canu, and P. B. Mogensen (1997), Whisper, a Resonance Sounder and Wave Analyser: Performances and Perspectives for the Cluster Mission, *Space Sci. Rev.*, *79*, 157–193, doi:10.1023/A:1004931326404.
- Décréau, P. M. E., P. Ferreau, V. Krasnoselskikh, E. Le Guirriec, M. Lévêque, P. Martin, O. Randriamboarison, J. L. Rauch, F. X. Sené, H. C. Séran, J. G. Trotignon, P. Canu, N. Cornilleau, H. de Féraudy, H. Alleyne, K. Yearby, P. B. Mögensen, G. Gustafsson, M. André, D. C. Gurnett, F. Darrouzet, J. Lemaire, C. C. Harvey, P. Travnicek, and Whisper Experimenters group (2001), Early results from the Whisper instrument on Cluster: an overview, *Ann. Geophys.*, *19*, 1241–1258.
- Escoubet, C. P., R. Schmidt, and M. L. Goldstein (1997), Cluster - Science and Mission Overview, *Space Sci. Rev.*, *79*, 11–32, doi:10.1023/A:1004923124586.
- Gendrin, R. (1960), Guidage des sifflements radioelectriques par le champ magnetique terrestre, *C. R. Acad. Sci.*, *251*, 1085–1087.

- Gendrin, R. (1961), Le guidage des whistlers par le champ magnetique, *Planet. Space Sci.*, *5*, 274–282.
- Goldstein, B. E., and B. T. Tsurutani (1984), Wave normal directions of chorus near the equatorial source region, *J. Geophys. Res.*, *89*, 2789–2810.
- Gurnett, D. A. (1974), The earth as a radio source - Terrestrial kilometric radiation, *J. Geophys. Res.*, *79*, 4227–4238, doi:10.1029/JA079i028p04227.
- Gurnett, D. A., and R. R. Anderson (1981), The Kilometric Radio Emission Spectrum: Relationship to Auroral Acceleration Processes, in *Physics of Auroral Arc Formation, Geophysical Monograph 25*, edited by S.-I. Akasofu & J. R. Kan, pp. 341–350.
- Gurnett, D. A., and A. Bhattacharjee (2005), *Introduction to Plasma Physics*, Cambridge University Press, Cambridge, UK.
- Gurnett, D. A., and B. J. O'Brien (1964), High-latitude geophysical studies with satellite Injun 3, 5, Very low frequency electromagnetic radiation, *J. Geophys. Res.*, *69*, 65–89.
- Gurnett, D. A., A. M. Persoon, R. F. Randall, D. L. Odem, S. L. Remington, T. F. Averkamp, M. M. DeBower, G. B. Hospodarsky, R. L. Huff, D. L. Kirchner, M. A. Mitchell, B. T. Pham, J. R. Phillips, W. J. Schintler, P. Sheyko, and D. R. Tomash (1995), The Polar plasma wave instrument, *Space Sci. Rev.*, *71*, 597–622.
- Gurnett, D. A., R. L. Huff, and D. L. Kirchner (1997), The Wide-Band Plasma Wave Investigation, *Space Sci. Rev.*, *79*, 195–208, doi:10.1023/A:1004966823678.
- Gurnett, D. A., R. L. Huff, J. S. Pickett, A. M. Persoon, R. L. Mutel, I. W. Christopher, C. A. Kletzing, U. S. Inan, W. L. Martin, J.-L. Bougeret, H. S. C. Alleyne, and K. H. Yearby (2001), First results from the Cluster wideband plasma wave investigation, *Ann. Geophys.*, *19*, 1259–1272, doi:10.5194/angeo-19-1259-2001.
- Gustafsson, G., R. Bostrom, B. Holback, G. Holmgren, A. Lundgren, K. Stasiewicz, L. Ahlen, F. S. Mozer, D. Pankow, P. Harvey, P. Berg, R. Ulrich, A. Pedersen, R. Schmidt, A. Butler, A. W. C. Fransen, D. Klinge, M. Thomsen, C. Falthammar,

- P. Lindqvist, S. Christenson, J. Holtet, B. Lybekk, T. A. Sten, P. Tanskanen, K. Lapalainen, and J. Wygant (1997), The Electric Field and Wave Experiment for the Cluster Mission, *Space Sci. Rev.*, 79, 137–156, doi:10.1023/A:1004975108657.
- Hamelin, M. (1978), Contribution to the study of electrostatic and electromagnetic waves near the lower hybrid frequency in ionospheric plasma, Ph.D. thesis, Centre de Recherches en Physique de l'Environnement Terrestre et Planetaire, Orleans (France).
- Haque, N., M. Spasojevic, O. Santolík, and U. S. Inan (2010), Wave normal angles of magnetospheric chorus emissions observed on the Polar spacecraft, *J. Geophys. Res.*, 115, A00F07, doi:10.1029/2009JA014717.
- Haque, N., U. S. Inan, T. F. Bell, J. S. Pickett, J. G. Trotignon, and G. Facskó (2011), Cluster observations of whistler mode ducts and banded chorus, *Geophys. Res. Lett.*, 38, L18,107, doi:10.1029/2011GL049112.
- Harten, R., and K. Clark (1995), The Design Features of the GGS Wind and Polar Spacecraft, *Space Sci. Rev.*, 71, 23–40, doi:10.1007/BF00751324.
- Haselgrove, J. (1955), Ray Theory and a New Method for Ray Tracing, in *Physics of the Ionosphere*, pp. 355–364, Physical Society, London, UK.
- Hayakawa, M., Y. Yamanaka, M. Parrot, and F. Lefeuvre (1984), The wave normals of magnetospheric chorus emissions observed on board GEOS 2, *J. Geophys. Res.*, 89, 2811–2821.
- Helliwell, R. A. (1965), *Whistlers and Related Ionospheric Phenomena*, Stanford Univ. Press, Stanford, CA.
- Helliwell, R. A. (1967), A Theory of Discrete VLF Emissions from the Magnetosphere, *J. Geophys. Res.*, 72, 4773–4790, doi:10.1029/JZ072i019p04773.
- Helliwell, R. A., and J. P. Katsufakis (1974), VLF Wave Injection into the Magnetosphere from Siple Station, Antarctica, *J. Geophys. Res.*, 79, 2511–2518, doi:10.1029/JA079i016p02511.

- Horne, R. B. (2002), The contribution of wave particle interactions to electron loss and acceleration in the Earth's radiation belts during geomagnetic storms, in *Review of Radio Science 1999-2002*, edited by W. R. Stone, pp. 801–828, chap. 33, John Wiley, Hoboken, NJ.
- Horne, R. B., and R. M. Thorne (1998), Potential waves for relativistic electron scattering and stochastic acceleration during magnetic storms, *Geophys. Res. Lett.*, *25*(15), 3011–3014.
- Horne, R. B., R. M. Thorne, S. A. Glauert, J. M. Albert, N. P. Meredith, and R. R. Anderson (2005a), Timescale for radiation belt electron acceleration by whistler mode chorus waves, *J. Geophys. Res.*, *110*, A03225, doi:10.1029/2004JA010811.
- Horne, R. B., R. M. Thorne, Y. Y. Shprits, N. P. Meredith, S. A. Glauert, A. J. Smith, S. G. Kanekal, D. N. Baker, M. J. Engebretson, J. L. Posch, M. Spasojevic, U. S. Inan, J. S. Pickett, and P. M. E. Decreau (2005b), Wave acceleration of electrons in the Van Allen radiation belts, *Nature*, *437*(7056), 227, doi:10.1038/nature03939.
- Hospodarsky, G. B., T. F. Averkamp, W. S. Kurth, D. A. Gurnett, M. Dougherty, U. Inan, and T. Wood (2001), Wave normal and Poynting vector calculations using the Cassini radio and plasma wave instrument, *J. Geophys. Res.*, *106*(A12), 30,253–30,269.
- Inan, U. S. (1986), Jovian VLF chorus and Io torus aurora, *J. Geophys. Res.*, *91*, 4543–4550, doi:10.1029/JA091iA04p04543.
- Inan, U. S., and T. F. Bell (1977), The plasmopause as a VLF wave guide, *J. Geophys. Res.*, *82*, 2819–2827, doi:10.1029/JA082i019p02819.
- Inan, U. S., R. A. Helliwell, and W. S. Kurth (1983), Terrestrial versus Jovian VLF chorus - A comparative study, *J. Geophys. Res.*, *88*, 6171–6180, doi:10.1029/JA088iA08p06171.
- Inan, U. S., Y. T. Chiu, and G. T. Davidson (1992), Whistler-mode chorus and morningside aurorae, *Geophys. Res. Lett.*, *19*, 653–656.

- Inan, U. S., T. F. Bell, J. Bortnik, and J. M. Albert (2003), Controlled precipitation of radiation belt electrons, *Journal of Geophysical Research (Space Physics)*, *108*, 1186, doi:10.1029/2002JA009580.
- Johnstone, A. D., C. Alsop, S. Burge, P. J. Carter, A. J. Coates, A. J. Coker, A. N. Fazakerley, M. Grande, R. A. Gowen, C. Gurgiolo, B. K. Hancock, B. Narheim, A. Preece, P. H. Sheather, J. D. Winningham, and R. D. Woodliffe (1997), Peace: a Plasma Electron and Current Experiment, *Space Sci. Rev.*, *79*, 351–398, doi:10.1023/A:1004938001388.
- Kennel, C. F., and H. E. Petschek (1966), Limit on stably trapped particle fluxes, *J. Geophys. Res.*, *71*, 1–28.
- Kimura, I. (1966), Effects of ions on whistler-mode ray tracing, *Radio Sci.*, *1*(3), 269.
- Koons, H. C. (1989), Observations of large-amplitude, whistler mode wave ducts in the outer plasmasphere, *J. Geophys. Res.*, *94*, 15,393–15,397, doi:10.1029/JA094iA11p15393.
- Koons, H. C., and J. L. Roeder (1990), A survey of equatorial magnetospheric wave activity between 5 and 8 R(E), *Planet. Space Sci.*, *38*, 1335–1341, doi:10.1016/0032-0633(90)90136-E.
- Lauben, D. S., U. S. Inan, T. F. Bell, and D. A. Gurnett (2002), Source characteristics of ELF/VLF chorus, *J. Geophys. Res.*, *107*(A12), 1429, doi:10.1029/2000JA003019.
- LeDocq, M. J., D. A. Gurnett, and G. B. Hospodarsky (1998), Chorus source locations from VLF Poynting flux measurements with the POLAR spacecraft, *Geophys. Res. Lett.*, *25*, 4063–4066.
- Li, W., R. M. Thorne, J. Bortnik, Y. Nishimura, and V. Angelopoulos (2011a), Modulation of whistler mode chorus waves: 1. Role of compressional Pc4-5 pulsations, *J. Geophys. Res.*, *116*(A15), A06,205, doi:10.1029/2010JA016312.
- Li, W., J. Bortnik, R. M. Thorne, Y. Nishimura, V. Angelopoulos, and L. Chen (2011b), Modulation of whistler mode chorus waves: 2. Role of density variations, *J. Geophys. Res.*, *116*(A15), A06,206, doi:10.1029/2010JA016313.

- Liu, K., S. P. Gary, and D. Winske (2011), Excitation of banded whistler waves in the magnetosphere, *Geophys. Res. Lett.*, *38*, L14108, doi:10.1029/2011GL048375.
- Lorentzen, K. R., J. B. Blake, U. S. Inan, and J. Bortnik (2001), Observations of relativistic electron microbursts in association with VLF chorus, *J. Geophys. Res.*, *106*(A4), 6017–6027.
- Maeda, K. (1976), Cyclotron side-band emissions from ring-current electrons, *Planet. Space Sci.*, *24*, 341–347, doi:10.1016/0032-0633(76)90045-3.
- Meredith, N. P., R. B. Horne, and R. R. Anderson (2001), Substorm dependence of chorus amplitudes: Implications for the acceleration of electrons to relativistic energies, *J. Geophys. Res.*, *106*, 13,165–13,178, doi:10.1029/2000JA900156.
- Meredith, N. P., R. B. Horne, R. M. Thorne, and R. R. Anderson (2003), Favored regions for chorus-driven electron acceleration to relativistic energies in the Earth's outer radiation belt, *Geophys. Res. Lett.*, *30*(16), 1871, doi:10.1029/2003GL017698.
- Mielke, T. A., and R. A. Helliwell (1992), An experiment on the threshold effect in the coherent wave instability, *Geophys. Res. Lett.*, *19*, 2075–2078, doi:10.1029/92GL02179.
- Mosier, S. R., M. L. Kaiser, and L. W. Brown (1973), Observations of noise bands associated with the upper hybrid resonance by the Imp 6 radio astronomy experiment, *J. Geophys. Res.*, *78*(10), 1673–1679.
- Muto, H., M. Hayakawa, M. Parrot, and F. Lefeuvre (1987), Direction finding of half-gyrofrequency VLF emissions in the off-equatorial region of the magnetosphere and their generation and propagation, *J. Geophys. Res.*, *92*, 7538–7550.
- Ni, B., R. M. Thorne, Y. Y. Shprits, and J. Bortnik (2008), Resonant scattering of plasma sheet electrons by whistler-mode chorus: Contribution to diffuse auroral precipitation, *Geophys. Res. Lett.*, *35*, L11106, doi:10.1029/2008GL034032.
- Omura, Y., Y. Katoh, and D. Summers (2008), Theory and simulation of the generation of whistler-mode chorus, *J. Geophys. Res.*, *113*, A04,223, doi:10.1029/2007JA012622.

- Parrot, M., O. Santolík, N. Cornilleau-Wehrlin, M. Maksimovic, and C. C. Harvey (2003), Source location of chorus emissions observed by Cluster, *Ann. Geophys.*, *21*, 473–480.
- Pickett, J. S., O. Santolík, S. W. Kahler, A. Masson, M. L. Adrian, D. A. Gurnett, T. F. Bell, H. Laasko, M. Parrot, P. Decreau, A. Fazakerley, N. Cornilleau-Wehrlin, A. Balogh, and M. Andre (2004), Multi-point Cluster observations of VLF risers, fallers, and hooks at and near the plasmapause, in *Multiscale Processes in the Earth's Magnetosphere: From Interball to Cluster*, pp. 307–328, Kluwer Academic Publishers.
- Poevlerlein, H. (1948), Strahlwege von radiowellen in der ionosphäre, *Sitz. Bayerischen Akad. Wiss.*, *1*, 175–201.
- Rosenberg, T. J., R. A. Helliwell, and J. P. Katsufakis (1971), Electron precipitation associated with discrete very-low-frequency emissions, *J. Geophys. Res.*, *76*(34), 8445–8452.
- Rosenberg, T. J., J. C. Siren, D. L. Matthews, K. Marthinsen, J. A. Holtet, A. Egeland, D. L. Carpenter, and R. A. Helliwell (1981), Conjugacy of electron microbursts and VLF chorus, *J. Geophys. Res.*, *86*(A7), 5819–5832.
- Rosenberg, T. J., R. Wei, D. L. Detrick, and U. S. Inan (1990), Observations and modeling of wave-induced microburst electron precipitation, *J. Geophys. Res.*, *95*, 6467–6475.
- Russell, C. T., R. C. Snare, J. Means, D. Pierce, D. Dearborn, M. Larson, G. Barr, and G. Le (1995), The GGS/Polar magnetic fields investigations, *Space Sci. Rev.*, *71*, 563–582.
- Santolík, O. (2008), New results of investigations of whistler-mode chorus emissions, *Non-linear Processes in Geophysics*, *15*, 621–630.
- Santolík, O., and D. A. Gurnett (2003), Transverse dimensions of chorus in the source region, *Geophys. Res. Lett.*, *30*(2), 1031, doi:10.1029/2002GL016178.
- Santolík, O., M. Parrot, and F. Lefeuvre (2003), Singular value decomposition methods for wave propagation analysis, *Radio Science*, *38*(1), 1010, doi:10.1029/2000RS002523.
- Santolík, O., D. A. Gurnett, and J. S. Pickett (2004), Multipoint investigation of the source region of storm-time chorus, *Ann. Geophys.*, *22*, 2555–2563.

- Santolík, O., D. A. Gurnett, J. S. Pickett, M. Parrot, and N. Cornilleau-Wehrin (2005), Central position of the source region of storm-time chorus, *Planet. Space Sci.*, *53*, 299–305, doi:10.1016/j.pss.2004.09.056.
- Santolík, O., J. Chum, M. Parrot, D. A. Gurnett, J. S. Pickett, and N. Cornilleau-Wehrin (2006), Propagation of whistler mode chorus to low altitudes: Spacecraft observations of structured ELF hiss, *J. Geophys. Res.*, *111*(A10), 10,208, doi:10.1029/2005JA011462.
- Santolík, O., D. A. Gurnett, J. S. Pickett, J. Chum, and N. Cornilleau-Wehrin (2009), Oblique propagation of whistler mode waves in the chorus source region, *J. Geophys. Res.*, *114*(A13), A00F03, doi:10.1029/2009JA014586.
- Sazhin, S. S., and M. Hayakawa (1992), Magnetospheric chorus emissions: A review, *Planet. Space Sci.*, *40*, 681–697.
- Scarf, F. L., and C. R. Chappell (1973), An Association of Magnetospheric Whistler Dispersion Characteristics with Changes in Local Plasma Density, *J. Geophys. Res.*, *78*, 1597–1602, doi:10.1029/JA078i010p01597.
- Shprits, Y. Y., R. M. Thorne, R. B. Horne, S. A. Glauert, M. Cartwright, C. T. Russell, D. N. Baker, and S. G. Kanekal (2006), Acceleration mechanism responsible for the formation of the new radiation belt during the 2003 Halloween solar storm, *Geophys. Res. Lett.*, *33*, L05104, doi:10.1029/2005GL024256.
- Sibeck, D. G., and V. Angelopoulos (2008), THEMIS Science Objectives and Mission Phases, *Space Sci. Rev.*, *141*, 35–59, doi:10.1007/s11214-008-9393-5.
- Smith, R. L., and J. J. Angerami (1968), Magnetospheric Properties Deduced from OGO 1 Observations of Ducted and Nonducted Whistlers, *J. Geophys. Res.*, *73*, 1–20, doi:10.1029/JA073i001p00001.
- Smith, R. L., R. A. Helliwell, and I. W. Yabroff (1960), A Theory of Trapping of Whistlers in Field-Aligned Columns of Enhanced Ionization, *J. Geophys. Res.*, *65*, 815–823, doi:10.1029/JZ065i003p00815.

- Spasojević, M. (2003), Global dynamics of the Earth's plasmasphere, Ph.D. thesis, Stanford Univ., Stanford.
- Stix, T. H. (1992), *Waves in Plasmas*, Springer-Verlag New York Inc., New York, NY.
- Storey, L. R. O. (1953), An investigation of whistling atmospherics, *Phil. Trans. R. Soc. London*, A246, 113–141.
- Strangeways, H. J. (1986), Whistler leakage from narrow ducts, *J. Atmos. Terr. Phys.*, 48, 455–462.
- Streltsov, A. V., M. Lampe, W. Manheimer, G. Ganguli, and G. Joyce (2006), Whistler propagation in inhomogeneous plasma, *J. Geophys. Res.*, 111(A10), A03,216, doi:10.1029/2005JA011357.
- Summers, D., B. Ni, and N. P. Meredith (2007a), Timescales for radiation belt electron acceleration and loss due to resonant wave-particle interactions: 1. Theory, *J. Geophys. Res.*, 112, A04206, doi:10.1029/2006JA011801.
- Summers, D., B. Ni, and N. P. Meredith (2007b), Timescales for radiation belt electron acceleration and loss due to resonant wave-particle interactions: 1. Evaluation for VLF chorus, ELF hiss, and electromagnetic ion cyclotron waves, *J. Geophys. Res.*, 112, A04207, doi:10.1029/2006JA011993.
- Thorne, R. M., E. J. Smith, K. J. Fiske, and S. R. Church (1974), Intensity variation of ELF hiss and chorus during isolated substorms, *Geophys. Res. Lett.*, 1, 193–196, doi:10.1029/GL001i005p00193.
- Thorne, R. M., T. P. O'Brien, Y. Y. Shprits, D. Summers, and R. B. Horne (2005), Timescale for MeV electron microburst loss during geomagnetic storms, *Geophys. Res. Lett.*, 110, A09202, doi:10.1029/2004JA010882.
- Trakhtengerts, V. Y. (1999), A generation mechanism for chorus emission, *Ann. Geophys.*, 17, 95–100, doi:10.1007/s005850050739.

- Trotignon, J. G., P. M. E. Décréau, J. L. Rauch, O. Randriamboarison, V. Krasnoselskikh, P. Canu, H. Alleyne, K. Yearby, E. Le Guirriec, H. C. Séran, F. X. Sené, P. Martin, M. Lévêque, and P. Ferreau (2001), How to determine the thermal electron density and the magnetic field strength from the Cluster/Whisper observations around the Earth, *Ann. Geophys.*, *19*, 1711–1720.
- Trotignon, J. G., J. L. Rauch, P. M. E. Décréau, P. Canu, and J. Lemaire (2003), Active and passive plasma wave investigations in the earth's environment: The Cluster/Whisper experiment, *Advances in Space Research*, *31*, 1449–1454, doi:10.1016/S0273-1177(02)00959-6.
- Trotignon, J. G., P. M. E. Décréau, J. L. Rauch, X. Vallières, A. Rochel, S. Kouglblénou, G. Lointier, G. Facskó, P. Canu, F. Darrouzet, and A. Masson (2010), *The WHISPER Relaxation Sounder and the CLUSTER Active Archive*, pp. 185–208, Springer Netherlands, doi:10.1007/978-90-481-3499-1_{12}.
- Tsurutani, B. E., and E. J. Smith (1974), Postmidnight chorus: A substorm phenomenon, *J. Geophys. Res.*, *79*, 118–127.
- Tsurutani, B. T., and E. J. Smith (1977), Two types of magnetospheric ELF chorus and their substorm dependences, *J. Geophys. Res.*, *82*, 5112–5128, doi:10.1029/JA082i032p05112.
- Villalon, E., and W. J. Burke (1995), Pitch angle scattering of diffuse auroral electrons by whistler mode waves, *J. Geophys. Res.*, *100*(A10), 19,361–19,370.
- Walt, M. (1994), *Introduction to Geomagnetically Trapped Radiation*, Cambridge University Press, Cambridge, UK.